Savannah River National Laboratory®

FY23 Laboratory Directed Research & Development Annual Report

SRNL-STI-2023-00648

Front cover: Closeup of the directed energy deposition (DED) system depositing refractory metal.

Read more about this research on p. 12.

Disclaimer

Message from the Laboratory Director and the Deputy Laboratory Director for Science & Technology

At Savannah River National Laboratory (SRNL), we put science to work to protect the environment and address nuclear security challenges. Through our transformative science and technology efforts, SRNL provides solutions to the Department of Energy (DOE) Office of Environmental Management (EM) for the safe cleanup of environmental legacy resulting from nuclear weapons development and government-sponsored nuclear energy research. SRNL also supports DOE's National Nuclear Security Administration (NNSA) as it maintains the nation's nuclear stockpile and reduces the threat of nuclear proliferation around the world.

Investments through SRNL's Laboratory Directed Research and Development (LDRD) program drive exploratory research foundational to advancements in mission critical technologies for EM, NNSA and other offices of DOE. Our LDRD program also provides meaningful development opportunities for the people central to innovation.

Seven Laboratory Director's Postdoctoral Research Fellows were supported by LDRD during fiscal year 2023. These named postdoctoral fellows are driving SRNL's scientific and technical core competencies forward through their dedication to research and advancement of technologies.

The LDRD program supports established researchers to explore new concepts, while fueling opportunities for the next generation of scientists to join the SRNL workforce, contributing to the global scientific community through scientific publications.

Enjoy reading this Annual Report which summarizes the innovative science and engineering contributions of SRNL staff supported by the LDRD Program.

Dr. Vahid Majidi

Laboratory Director

Dr. Sue Clark

Deputy Laboratory Director,
Science and Technology

Contents

Overview

The Laboratory Directed Research and Development (LDRD) program yields foundational scientific research and development (R&D) essential to growing SRNL's core competencies, in alignment with SRNL's Strategic Plan to provide long-term benefits to the Department of Energy (DOE), the National Nuclear Security Administration (NNSA), and other customers and stakeholders. Five strategic goals are outlined in SRNL's strategic plan:

1) Provide applied science and engineering for EM's active clean-up sites and LM's post closure management sites
2) Provide science-based solutions for gaps identified in nonproliferation strategic vision and support the government in activities impacting national security
3) Lead Science, Technologie & Engineering as the central technical authority for processing tritium loaded reservoirs and support production of plutonium pits
4) Align science and energy security programs by focusing modern modeling, simulation, and data analytics tools on materials engineering and performance applications
5) Build a workforce for the future

To fully achieve these strategic goals, SRNL must build upon its technical core competencies. SRNL's six core competencies underpinning the laboratory's strategic goals include:

- Accelerating remediation, minimizing waste, and reducing risk
- Enabling next-generation nuclear material processing and disposition
- Creating manufacturing solutions for EM, NNSA, and energy security
- Assuring production and supply of strategic materials and weapons components
- Sensing, characterizing, assessing, and deterring nuclear proliferation
- Securing connected control systems and associated data

SRNL has focused LDRD Program investments to expand and strengthen the SRNL core competencies. Each project aligns with one or more of the technical core competencies. In addition to supporting SRNL's core competencies, each LDRD investment aligns with one or more of three overall program objectives:

The Three Main Objectives of the LDRD Program

LDRD FY23 by the Numbers

40
Total Projects

$7.85M
Total Program Cost
Fully Burdened

30
Peer-Reviewed Publications
Manuscripts are evaluated in an independent review where experts assess the research for quality and accuracy prior to publication acceptance.

1
Patent Issued

16
Patent Applications

8
Invention Disclosures

28
Postdocs Funded
over 10% of total hours

8
Postdocs Converted to Staff Hires

29
Projects Involving Postdocs

19
Projects Led by Early Career Staff
Early career: within 5 years of terminal degree

9
Projects Involving Interns

Universities Engaged

- University of South Carolina
- Clemson University
- University of Georgia
- Virginia Polytechnic Institute & State University
- Alfred University
- Georgia Institute of Technology
- California State University, Northridge
- New Mexico Institute of Mining and Technology
- University of South Alabama

LDRD Named Postdoctoral Researchers Thrive at SRNL

Strengthening SRNL's future workforce is a primary goal of the LDRD Program. One of the main avenues to accomplish this is hosting postdoctoral researchers ("postdocs"). Through their research supported by the LDRD program, postdocs develop their professional skills while solving complex technical and scientific problems. In the process, they grow their professional network and further their scientific reputation through publication of their research findings in peer-reviewed journals.

SRNL's Laboratory Director's Postdoctoral Research Fellow, a named postdoctoral fellowship, was established in FY22 and grew to seven positions in FY23. The Laboratory Director's Postdoctoral Research Fellows are experts in their field, with strong publication records. With a focus on one specific project under the guidance of an SRNL research advisor, the fellows are provided the opportunity to apply their expertise on a focused scientific question and make a long-term research impact. Fellows are afforded a high level of creative freedom and the time necessary to hone their critical thinking and problem-solving skills. The fellows are provided the tools and resources necessary to grow as researchers and succeed in the national laboratory R&D environment.

SRNL's named postdoctoral fellows supported by LDRD during FY23 are highlighted below.

"The Laboratory Director's Postdoc has allowed me the freedom to take on one of the most challenging and comprehensive atomistic modeling techniques that I desperately wanted to develop during graduate school. The Laboratory Director's Postdoc has allowed me to make it a reality here at SRNL – and it is awesome that I can use my project to help the mission of the lab! This postdoc opportunity allows me to put a big bow on top of all my scientific education."

Nick Szaro

Joined SRNL in August 2023 from University of South Carolina

"A named postdoctoral fellow at a national laboratory is an amazing achievement in anyone's career, however, the Laboratory Director's Postdoctoral Fellow at SRNL is unique, in that it provides a blend of mentorship and research opportunities that sets up postdoctoral fellows with the skills needed to be the next generation of world class researchers.

Alex Bretaña

Joined SRNL in July 2022 from University of Missouri

The Laboratory Director's Postdoc position will set me up for success in my career as it is allowing me to focus on one project and learn everything necessary to reach the goals of the project. Specifically, I have the ability to learn and develop computational skills while simultaneously honing my experimental skills that I developed in graduate school. In tackling this one project, I will become a much more well-rounded scientist with skills that are readily transferrable to a multitude of future projects. Likewise, the network of researchers and mentors that I have grown and cultivated thus far has allowed me to see the breadth of possibilities to extend our work to other domains in the future.

Brandon Yost

Joined SRNL in May 2023 from University of North Carolina at Chapel Hill

I have liked the independence associated with being an LDRD Laboratory Director's post-doc. It has allowed me to not only do my research, but also to navigate everything associated with working for SRNL on my own. Between handling what materials/equipment needs to be ordered, designing, and executing experiments, and navigating the aspects of working at SRNL in general, the position has allowed me to develop my abilities as a scientist and an independent researcher.

Jesse Smith

Joined SRNL in August 2023 from Texas A&M University

The Laboratory Director's Postdoctoral Researcher position has challenged me to take a project from idea to practice using my skills. This will set me up for success in my career by demonstrating that I can begin a new project, learn the required skills, and quickly produce results; skills that will be required for all future positions. The structure of the Laboratory Director's Postdoctoral Researcher position allows me to concentrate on one major project and make large progress rather than making smaller advances on many projects.

Matt Gordon

Joined SRNL in September 2023 from Indiana University

"The Laboratory Director's Postdoc position is an incredible opportunity to turn ideas into results on a national lab scale. This position allows me to focus on my proposed work and gives me the resources and time to perform research at the highest level achievable. The progression through this postdoc opportunity will undoubtably hone my skills as a scientist and further prepare me for my career ahead.

Logan Breton

Joined SRNL in August 2023 from University of South Carolina

"I think that the Laboratory Director's postdoc position will allow me to make a significant contribution to SRNL while also giving me the opportunity to learn and grow as a scientist and researcher.

Greg Chipman

Joined SRNL in September 2023 from Brigham Young University

WORKFORCE DEVELOPMENT

Exploring a New Frontier of Radiation-Resistant Materials

Dr. Guin tests a radiation-stable elastomer by gentle stretching the as-cast piece while looking for voids or defects.

Providing science and technology solutions is central to the purpose of the Savannah River National Laboratory (SRNL) Laboratory Directed Research and Development (LDRD) program. With a focus on mission agility, the SRNL LDRD program supports the exploration of new approaches to address current and future DOE and NNSA mission needs.

In FY23, the LDRD program funded researcher Tyler Guin to investigate a novel solution to radiation-stable polymers to address challenges the NNSA currently faces with the general incompatibility of radioactive gasses, such as tritium, and polymers. Motivated by market need and the current gaps in existing scientific knowledge, Guin is using this work to drive SRNL's core competency of next-generation nuclear materials processing by working towards a material solution that will improve safety, lower the costs, and enable new methods of handling, containing, and processing nuclear materials.

He has leveraged the methodology to produce phenyl silicone elastomers. When asked about the motivation behind his LDRD project, "Tritium and radiation-resistant silicone membranes through tailored phenyl content," Guin remarked: "We knew that tritium-resistant polymers were useful throughout the NNSA system. We tested our first samples at an exposure matching the highest seen in literature to highlight the potential of these polymers." Through NNSA support, Guin will perform tritium exposures, building off the LDRD research which focused on gamma irradiation of similar polymeric materials.

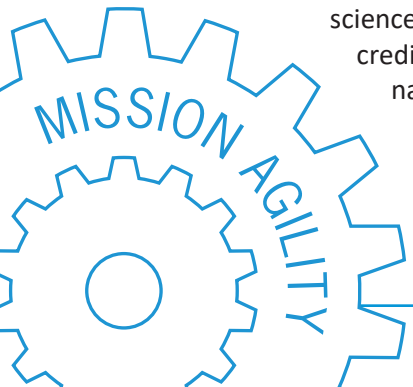

A record of providing mission critical solutions such as Guin's maintains SRNL's reputation as a premier applied science laboratory, allowing further research exploration to address complex national problems. He credits his LDRD project for the opportunity to transform his research into a product that meets national sponsor needs, saying, "Without LDRD, we would not have had any samples, polymers, or proof of concept required to justify furthering the research."

The LDRD program will continue to support mission-focused research such as Guin's to sustain and enhance SRNL's reputation as a leading research and development institution.

At SRNL, we put science to work.

Advanced Manufacturing of Novel Alloys for Harsh Environments

Inspired by the high demand for novel materials that perform well in harsh service conditions, SRNL researcher Guru Dinda is exploring new alloy development supported through the Laboratory Directed Research and Development Program (LDRD).

The LDRD Program supports high-risk and innovative projects that address emerging scientific needs. In addition, LDRD provides national laboratories with the opportunity to acquire and build the foundational tools that ensure long-term scientific vitality for the nation. The LDRD program at Savannah River National Laboratory (SRNL) is no exception, and a successful example is Dinda's cutting-edge LDRD project, "Accelerated Discovery of W–Re–Ta–Mo Refractory Medium Entropy Alloy for Extreme Conditions". Dinda and his team have established a novel, laser-based, directed energy deposition (DED) system to demonstrate a newly proposed high-throughput alloy development concept.

To counter traditional resource-intensive and time-consuming approaches for alloy development, Dinda and his team are working to implement a high-throughput combinatorial alloy development framework based on additive manufacturing principles coupled with CALPHAD-based solidification modeling. To accomplish this objective, he developed a novel, open architecture DED machine. The laser-based DED system uses a 3-kW diode laser, six-axis robotic arm, coaxial nozzle, and four powder feeders. Seldom found in commercial DED systems, this machine allows for quick process parameter optimization (e.g., laser power, scanning speed, and powder feed rates) by changing the parameters synchronously. This allows samples to be produced in a higher yield than previous methods, decreasing the costs associated with each sample and allowing for a wider range of material testing. Therefore, it is anticipated, "That the DED-based combinatorial alloy development process will be the future of rapid development of new materials for structural and functional applications," said Dinda.

This use of Additive Manufacturing (AM) to target alloy development for harsh environments has reinforced and broadened SRNL's position in advanced manufacturing, and consequently has garnered interest from many researchers in the AM realm. In particular, this advancement has helped promote workforce development

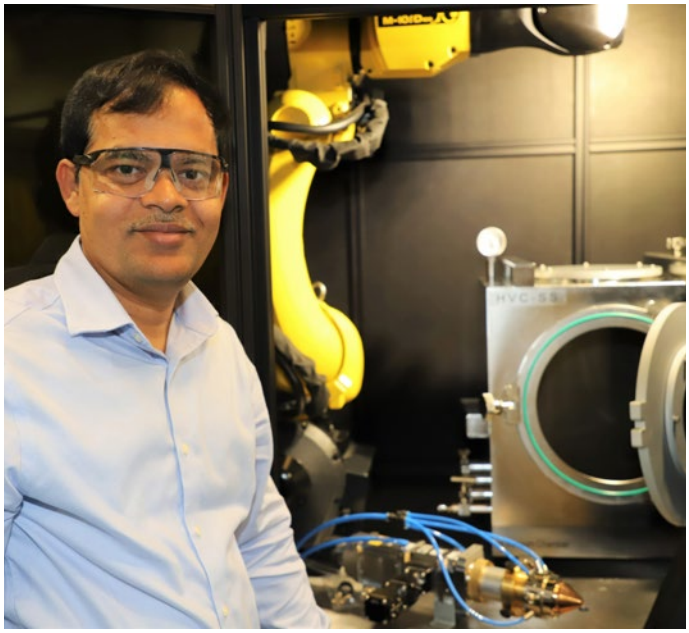

Dr. Dinda stands beside the DED System components: coaxial nozzle, inert gas chamber and 6-axis robot. (photo by Kelsie Taylor)

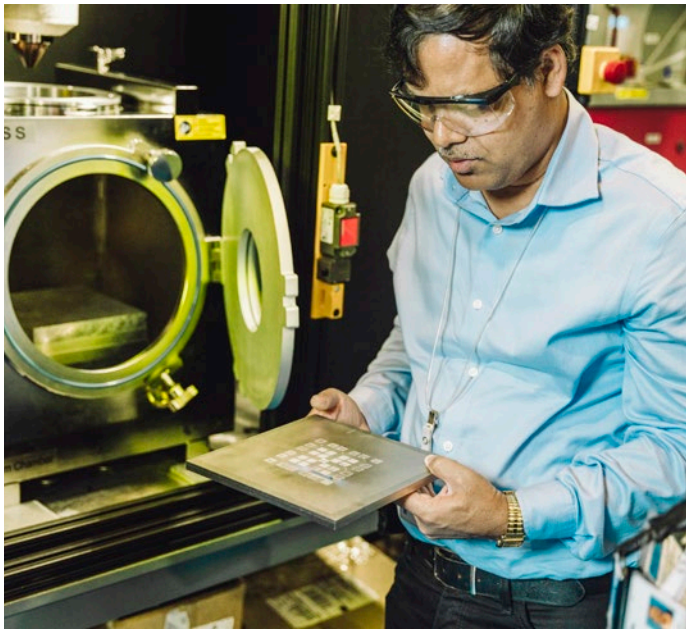

Visually inspecting the quality of the deposited coupons.

TECHNICAL VITALITY

at the laboratory. An example is the influence that Dinda's research had on Colleen Hilla, one of SRNL's named Eisenhower Postdoctoral fellows, when selecting the path for her success as an early career scientist. When asked about the impact of Guru's work on her research trajectory, Colleen shared the following: "When applying for the Eisenhower fellowship, my proposed project required the use of a multi-hopper DED system. Upon visiting SRNL I spoke with Guru about the system he was then in the process of developing. This system will allow us to complete high-throughput materials processing. Having this capability in-house will provide expanded opportunities for this and future work." Since arriving at SRNL, Colleen and Guru have worked closely to develop synergy between their projects and will continue to explore the capabilities of the DED system.

Guru and his team are an excellent illustration of SRNL's mission to provide high-value, cost-effective solutions to complex technical problems. Their DED-based system is a prime example of how the LDRD program at SRNL is championing a strong technical presence and building a lasting reputation in the scientific and technical communities.

The powder feeders are filled with different metal powders to create an alloy.

FY23 PROJECTS

CORE COMPETENCY:

Accelerating remediation, minimizing waste, and reducing risk

Modified Carbon Engineered Cellular Magmatics

William Jolin

Engineered Cellular Magmatics upcycled from post-consumer waste glass can provide a porous scaffold to support activated carbon. The activated carbon was modified by attaching a chelator to remove metals from solution with increased efficacy, creating a tunable solution for contaminant removal from previous waste products.

Introduction

Engineered Cellular Magmatics (ECMs) are synthetic, engineered pumice used as insulation or as geotechnical fill. The source glass material (typically commercial soda-lime-silica container glass) is mixed with a foaming agent. The mixture is subject to thermal treatment, at temperature much lower than traditional glass recycling, where the foaming agent decomposes, creating pores in the ECM structure. The foaming agent, often calcium carbonate, can be modified to other sources of carbon leading to variation in the product structure.[1] Activated carbon, in conjunction with other agents (e.g. calcium carbonate), can be used to foam ECMs, leaving behind a portion of oxidized carbon on the surface of the ECM pores. This oxidized carbon can then be modified to target and sequester specific contaminants. Proof of concept through the modification of the surface-bound activated carbon with the chelator Ethylenediaminetetraacetic acid (EDTA) can demonstrate that these novel materials can be tuned for various contaminants of concern.

Approach

The objective of the proposed work is to modify activated carbon based ECMs by attaching functional groups that target specific contaminants of concern. ECMs with 1-5 wt% partially oxidized carbon were fabricated at SRNL at the lab scale. These ECMs were further oxidized by chemical means to create carboxyl groups on the surface of the activated carbon incorporated into the structure of the ECMs. The ECMs with oxidized carbon will be further modified (**Figure 1**) by 1) zinc (or nickel) impregnation:

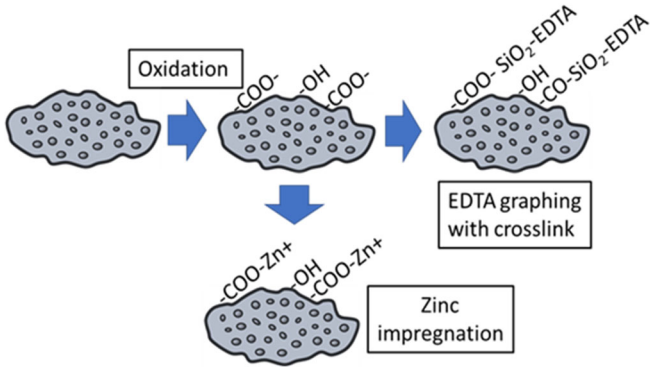

Figure 1. ECM modification process

where positively charged zinc sorbs to the negatively charged carboxyl group and 2) the attachment of ethylenediaminetetraacetic acid (EDTA) through a silica cross link. Zinc, a weak Lewis acid, can act as a complexation site to bind nitrates, iodates, and other oxyanions while EDTA is a robust chelator of cationic metals and radionuclides.

Accomplishments

- ECMs with 1-5 wt% partially oxidized carbon were fabricated at SRNL at the lab scale with 2% carbon providing balance between porosity/surface area and carbon content.
- Method for EDTA attachment to ECMs was developed. EDTA was attached to the surface of the activated carbon containing ECMs through a silica cross link where Tetraethyl orthosilicate (TEOS) and N-(Trimethoxysilpropyl)ethylenediamine, tetraacetic acid (TMS-EDTA) was added stepwise to a hydrochloric acid solution containing the carbon-

[1] König, et al. "Fabrication of highly insulating foam glass made from CRT panel glass." *Ceramics international* **2015**,41(8), 9793-9800.

ECMs. This seemingly permanent attachment overcame the interferences of the glass matrix for attachment and modification. The modified material was characterized by thermogravimetric analysis (TGA). TGA results revealed approximate 1% coverage of EDTA by mass on the surface of the ECMs.

- Sorption of Fe, Ni, and Pb was then tested to the modified and unmodified ECMS through batch isotherm experiments.
- An 80% uptake of Fe was evident onto EDTA modified carbon ECMs in acidic conditions. No uptake was seen for unmodified ECMs, carbon containing or otherwise, under similar conditions. The modification of carbon containing ECMs was therefore determined to be successful.
- Sorption of Pb was high to all forms of ECMs (modified and unmodified), suggesting the use of the material as a multi mechanism sorbent.
- Under alkaline conditions sorption of all metals was high to unmodified ECMs, again showing the usefulness of ECMs a means to sequester contaminants overall.
- Nitrate and chromate uptake onto zinc and nickel impregnated ECMs was minimal, likely due to the interference of counterions released from the glass structure or the formation of unreactive Zn or Ni oxides on the surface.

Peer-reviewed Publications

In preparation:

- "Contaminant Sequestration Using Engineered Cellular Magmatics" William Jolin, Anna Stanfield, Austin Stanfield, and Cory Trivelpiece
- "Carbon Functionalized Foamed Glass Ceramics for Remediation of Heavy Metal Contaminated Water" Alex Kugler, Austin Stanfield, Anna Stanfield, Logan Howell, Kylie Manning, Cory Trivelpiece, and William Jolin

Intellectual Property

- Provisional Patent Application; SRS-23-025, Functionalized Carbon-Modified Foamed Glass Ceramics

Team Members

Austin Stanfield, Anna Stanfield**,** Eric McCaslin, Cory Trivelpiece, William Jolin, Alex Kugler, Courtney Burckhalter, Austin Stanfield[*], Erin McCaslin[*], Logan Howell[+], Kylie Manning[+]

[*]Postdoctoral Researcher
[+]*SRNL* Intern

photo by Chris O'Neil

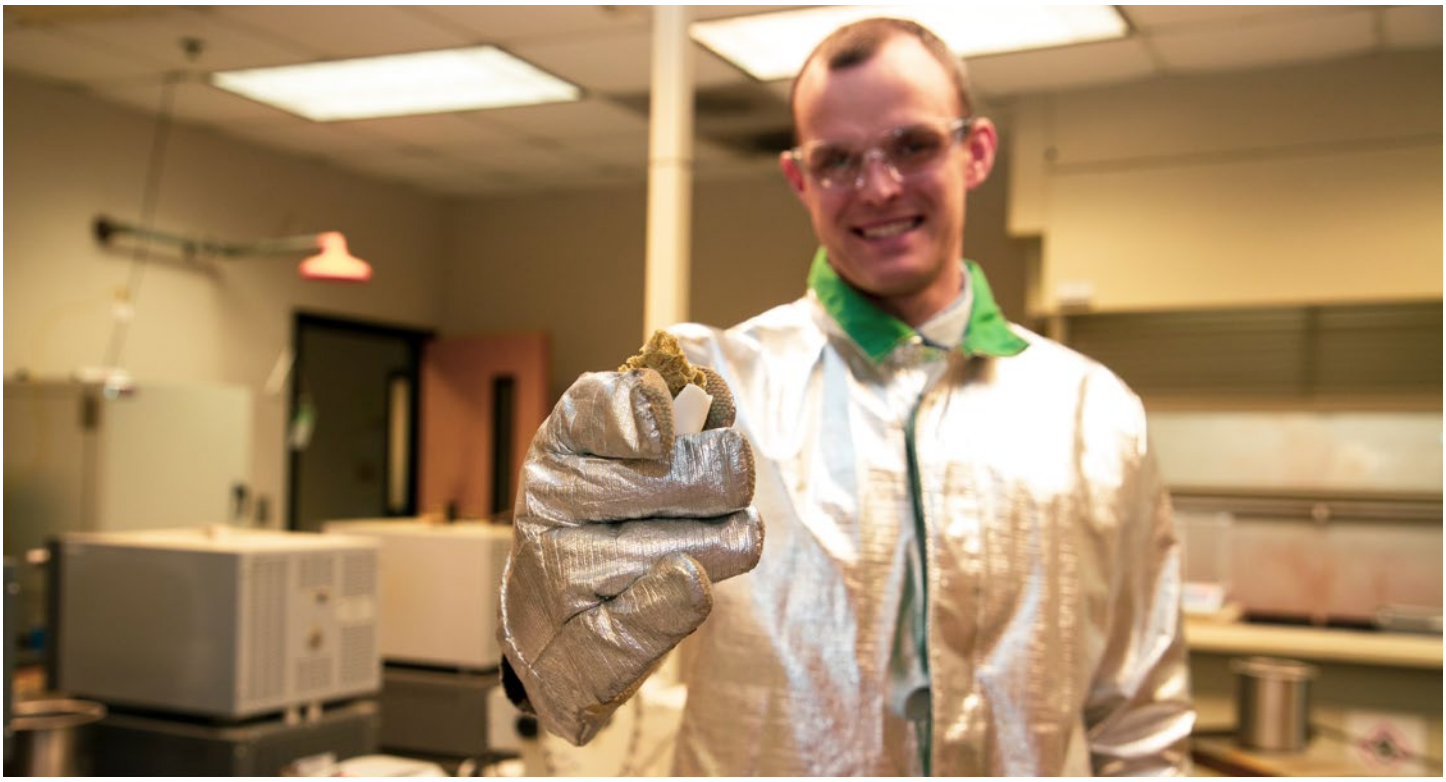

Gamma Radiation Protected Self-Healing Polymer Composite

Brady Lee

This research will help understand microbiological response mechanisms with respect to radiation resistance and associated genetic loci for response to radiation in individual prokaryotes and microbial communities. Environmental isolates involved in radionuclide biotransformation will also be tested for radiation resistance to understand how metabolism in these environments can be improved through higher survival rates in the presence of ionizing radiation. Identification of important genetic determinants and microbes with a range of radiation resistance will allow future development of biosensors for nonproliferation, environmental, and medical purposes. This year's report will provide a final summary of all three years of research.

Introduction

Radiation resistance is a common biotic trait, yet molecular resistance mechanisms are not well understood. The objective of the proposed work is to understand how expression of single-stranded deoxyribonucleic acid binding proteins are central to radiation resistance. Expression of single-stranded deoxyribonucleic acid binding proteins in a highly – radiation-resistant microorganism is hypothesized to be a model of radiation resistance across the three domains of life. Expression of genes encoding these proteins and associated regulators was analyzed in the radiation resistant prokaryote, *Halobacterium salinarum* NRC-1. In addition, radiation resistance in environmental isolates used for radionuclide transformation will also be determined. Communities from radioactive environments will also be characterized in the final year of the project. Signatures that are part of this mechanism are important to the Department of Energy because the information can be used as a signature for radiation biology, non-proliferation, and improved remediation processes, as well as preventing corrosion in nuclear storage environments.

Approach

Research goals were accomplished using a combined molecular biology and microbial growth approach. In order to determine the effect of this large insertion on the expression of three RPA homologs in *Halobacterium*, these regulators and the region containing the mutation were deleted (**Figures 1 & 2**) and analyzed for changes in the expression of *rfa1*, *rfa2*, and *rfa3* through quantitative PCR. In addition, experiments were performed to monitor changes in growth characteristics associated with gene deletion. Strain designation keys are shown in **Table 1**. Plasmids constructed are shown in **Table 2**. Known strains of metal and radionuclide reducing bacteria were exposed to varying levels of ionizing radiation and then grown to determine levels of radiation resistance in these species.

The Savannah River Site L-Basin Facility is used to store fuel from various locations across the DOE Complex. Visual examination of racks used to store fuel rods indicated the presence of material resembling spider webs. During maintenance to remove debris from the bottom of the storage basins, filters were used to collect samples. Organic and inorganic material from the samples were used for microbial enrichments, as well as DNA extraction for future sequencing analyses.

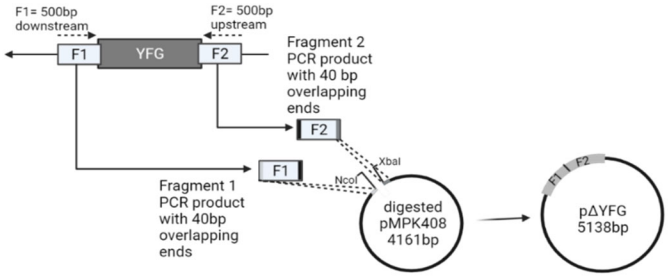

Figure 1. Schematic outlining the creation of deletion plasmids. The suicide vector pMPK408 was used in a Gibson Assembly. "YFG" is a placeholder for the gene/region of interest.

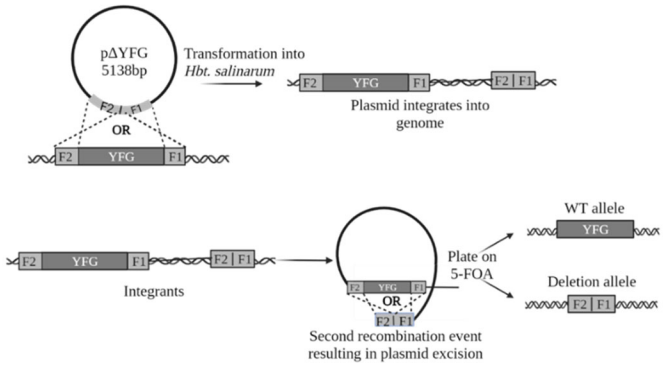

Figure 2. Schematic of the homologous recombination events in the established pop-in-pop-out method of gene replacement (Peck et al, 2000). This method can result in either the retention of the wild-type allele or the replacement by the deletion allele.

Accomplishments

- Tools were developed using Gibson Assembly (**Figure 1**) and established methods (**Figure 2**) to generate knockout alleles of loci potentially involved in radiation resistance in *Halobacterium.*
- Demonstrated the co-transcription of two potential regulatory genes in *Halobacterium* and the extent of leader transcript (**Figure 3**).
- Microbes known to metabolize and concentrate radionuclides demonstrated varying levels of radiation resistance (**Table 3**).
- Determined that radiation resistance may be attributed to multiple factors working in unison and that regulators for single-stranded DNA binding proteins are likely located in other areas of the genome (**Figure 4, Tables 4 & 5**).
- A deletion in the gene encoding an ATP-dependent RNA helicase homolog caused changes in growth along with changes in expression of RPA genes (**Figures 5, 6 and 7**).
- Isolated new halophilic species for additional testing and genome sequencing.
- Isolated microbial DNA from hypersaline environments for community analysis.
- Sediment samples from L-Basin showed high numbers of low nutrient, iron related, anaerobic, and acid producing bacteria (**Table 6**). No sulfate reducing bacteria were found in the samples.

***Hbt. salinarum* strain**	**Genotype**	**Source**
NRC-1	Wild type	Gift from S. DasSarma
LH101	As NRC-1, but Δ*ura3*	Laboratory stock
LH102	Δ*ura3* derivative of radiation resistant mutant LH5	Laboratory stock
LH103	Δ*ura3* derivative of radiation resistant mutant LH6	Laboratory stock
LH 184	As LH103, but Δ*vng155*	This study
LH185	Isogenic to LH184, but *vng155*$^{+}$	This study
LH186	As LH101 but Δ*ecp*	This study
LH187	Isogenic to LH186, but *ecp*$^{+}$	This study
LH188	As LH102 but Δ*ecp*	This study
LH189	Isogenic to LH188, but *ecp*$^{+}$	This study
LH190	As LH103 Δ*ecp*	This study
LH191	Isogenic to LH190, but *ecp*$^{+}$	This study
LH192	As LH101 but Δ*erc*	This study
LH193	Isogenic to LH192, but *erc+*	This study
LH196	As LH101, but Δ*vng155-160*	This study
LH197	Isogenic to LH192, but *vng155-160*$^{+}$	This study
LH198	As LH103, but Δ*vng155-160*	This study
LH199	Isogenic to LH194, but *vng155-160*$^{+}$	This study

Table 1. Strains used in studies for Tables 4 & 5, and Figures 3-6.

Plasmid	**Description**	**Source**
pMPK408	Litmus 28 (NEB)-based plasmid containing *ura3;* suicide vector for *Halobacterium*	Peck et al., 2000
pKQP1	pMPK408 containing *Δerc* allele	This study
pKQP2	pMPK408 containing *Δecp* allele	This study
pHTL150	pMPK408 containing *Δprtr1* allele	This study
pHTL155	pMPK408 containing *Δvng41* allele	This study
pHTL156	pMPK408 containing *Δvng41* - *tnp1*	This study

Table 2. Plasmids used to knockout selected genes in *Halobacterium*. Construction is shown in Figure 1. Resulting strains are listed in Table 1.

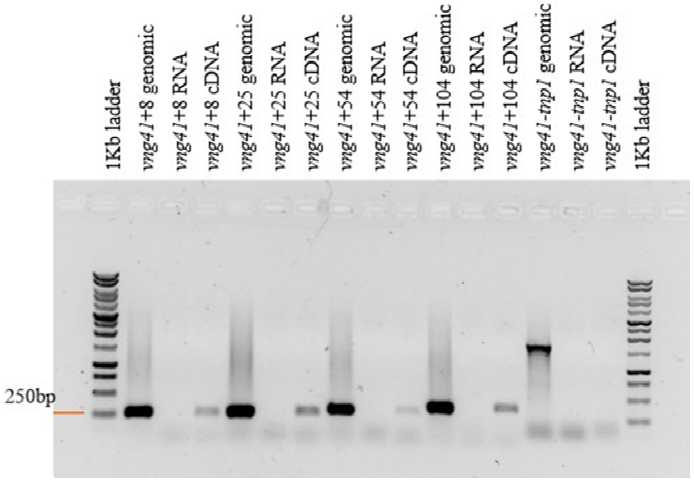

Figure 3. Determination of co-transcription and analysis of start of transcription of genes in the *prtr1-vng41* region. All isolated strains transcribe the region between the start of *prtr1* and 104 bp upstream of the start of *vng41* amplified from cDNA. LH101 genomic DNA was used as a control.

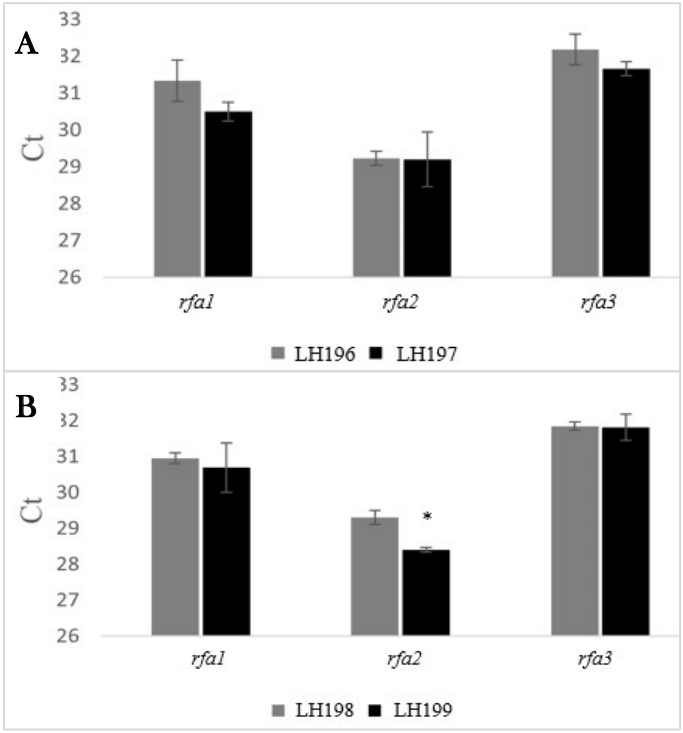

Figure 4. Effect of deletion of *vng41-tnp1* on *rfa* gene expression. Deletion of the *vng41-tnp1* intergenic region confers a significant change in Ct (cycle threshold) values in background strain LH103 (LH198/LH199) (B), but not in background strain LH101 (LH196/LH197)(A). Ct values are shown for each target gene. Gene deletions were confirmed using qPCR.

Microbial Species	D10 (Gy)
Cellulomonas ES-6	80 - 320
Cupriavidus basilensis SRS	20 - 80
Shewanella algae BRY	20 - 80
Shewanella oneidensis MR-1	20 - 80

Table 3. Ionizing radiation resistance in metal and radionuclide reducing bacteria. D10 is the radiation dose required to inactivate 90% of a viable microbial population or reduce the population by a factor of 10.

Strain	Copy# *rfa1*	Copy# *rfa2*	Copy# *rfa3*
LH184	1.49e6	1.62e6	5.9e6
LH185	1.27e6	1.9e6	6.87e6
LH196	6.55e5	7.95e5	4.69e6
LH197	1.13e6	8.10e5	6.87e6
LH198	8.42e5	7.54e5	6.0e6
LH199	9.99e5	1.36e6	6.17e6

Table 4. Absolute expression of *rfa* genes in strains deleted for potential regulatory regions for *rfa3* compared to their isogenic counterparts.

Strain	*rfa1*	*rfa2*	*rfa3*
LH101	4.79×10^5	7.56×10^4	3.1×10^6
LH102	5.80×10^5	7.59×10^4	7.28×10^6
LH103	4.4×10^5	7.51×10^4	9.82×10^6

Table 5. Copy number of *rfa* gene transcripts in *H. salinarum* strains in the absence of irradiation.

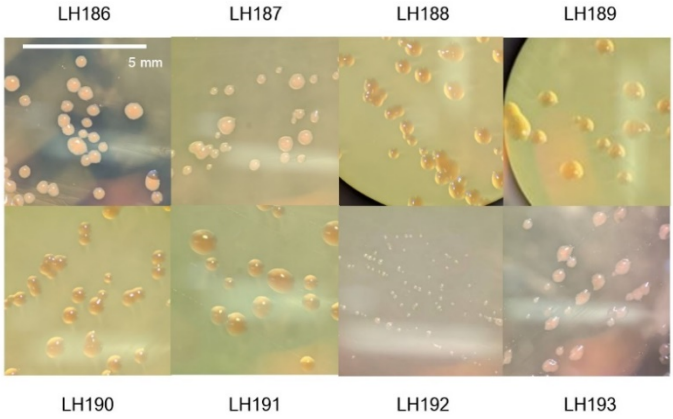

Figure 5. *Halobacterium salinarum* deletion and isogenic strains LH186-LH193. Strains were grown on solid CM+ media for 7 days and viewed under a light microscope. See Table 1 for genotypes of strains. Gene deletion was confirmed using qPCR.

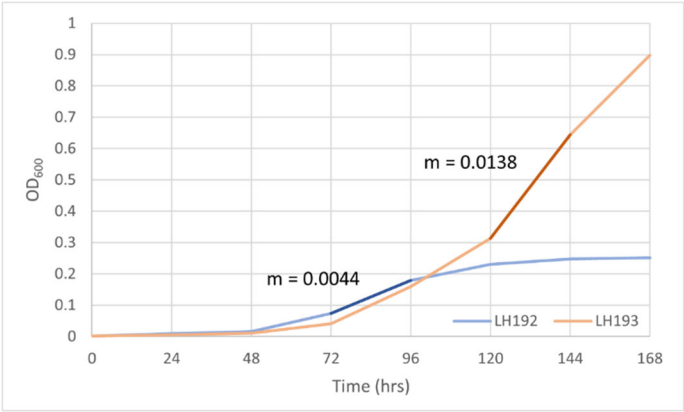

Figure 6. Effect of erc deletion on growth kinetics of H. salinarum. erc deletion LH192 (blue line) and isogenic strain LH193 (orange line). Exponential phase for each is highlighted in the corresponding darker color.

Biofilm Sample ID	Low Nutrient Bacteria (LNB) cells/mL	Iron Related Bacteria (IRB) cells/mL	Anaerobic Bacteria (ANA) cells/mL	Acid-Producing Bacteria (APB) cells/mL	Sulfate-Reducing Bacteria (SRB) cells/mL
10 HI	>100,000	>100,000	10-100	1,000-10,000	ND
25 LO	>100,000	>100,000	10-100	10-100	ND

Table 6. Microbial cell numbers for different physiological types in L-Basin sediment samples.

A

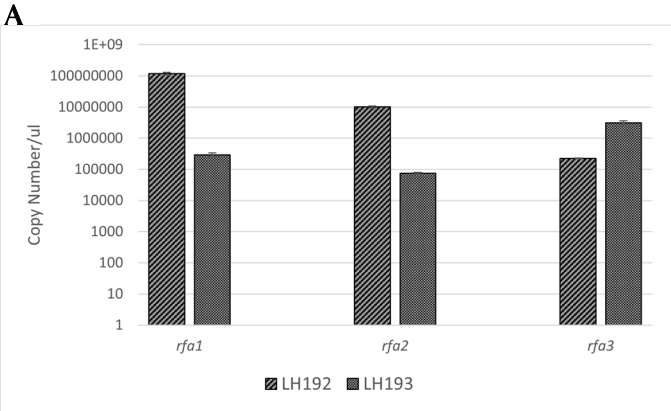

B

Gene	Relative Change	p-value
rfa1		
	400.018	3.82E-06
rfa2		
	133.670	3.15E-07
rfa3		
	0.07233	0.0084

Figure 7. Copy number of *rfa1*, *rfa2*, and *rfa3* in *erc* deletion (LH192) and *erc*+ (LH193) strains. (A) Expression of RPA homologs. (B) Relative change of RPA homolog expression in LH192 as compared to LH193.

Peer-reviewed Publications

- Meeks, H.N., R.P. Oates, H. Cui, G. M. Hwang, R.P. Volpe, R. B. Hayes, T.Y. Steen, R.T. Agans, C.E. Turick, R. Brigmon, B. Liebeskind, K. Ganduly, M.R. Sussman, B.D. Lee, A. Lewis, D. Schabacker, and W.L. McKendred. Harnessing the Environment to Identify Nuclear Processes: Biologically-Mediated Approaches. *Countering WMD J.,* **2022**, *24,* 60-85
- Perea, K., L. DeVeaux, R. Brigmon, B.D. Lee. Complete genome sequence of *Cellulomonas sp*., strain ES6, a chromate-reducing bacterium isolated from chromium-contaminated subsurface sediment. Microbiology Resource Announcement. DOI: https://doi.org/10.1128/MRA.00495-23

Team Members

Nate Losey[*], Linda DeVeaux[a], Hannah Lambertson[a], Katheryn Perea[a], Katherine Persinger[a]

[a] New Mexico Institute of Mining and Technology
[*] *Postdoctoral Researcher*

A Lightning Forecast System to Mitigate DOE EM Risk

Stephen Noble

Lightning represents a safety hazard to outdoor workers and equipment at the Savannah River Site and at other Department of Energy sites. Our objective is to provide innovative site lightning forecasts using modeled cloud physics, typical of real-world lightning formation, that are derived from high resolution numerical weather prediction models.

Introduction

The Savannah River Site (SRS) experiences more than 3,000 lightning strikes per year, which poses a safety risk to workers. However, the Atmospheric Technologies Group (ATG) does not currently perform explicit lighting forecasts for SRS. The current notification system is based on the detection of 3 occurring cloud-to-ground lightning strikes within the SRS boundaries or a small buffer area (~10 km) and does not provide advanced warning of lightning threat. This legacy procedure has led to a handful of near misses in the last few years when thunderstorms have developed directly over SRS, allowing limited or no warning to workers in the field.

Lightning potential is created by vertical atmospheric motions separating charges within mixed phase clouds. The coexistence of different ice types and liquid water droplets are essential for the transfer of ions within these mixed phase clouds. Mesoscale numerical weather prediction (NWP) models provide high resolution cloud properties such as solid and liquid water content as well as vertical velocities. Lightning indices, such as the Lightning Potential Index[1], make use of this information from these models to provide lightning potential forecasts in a realistic physical sense. ATG operationally runs mesoscale models for use in site forecasts and emergency response, which can be also used to provide information for lightning forecasts. Our objective is to provide a robust lightning forecast system to reduce risk to DOE workers and property, especially in a changing climate where extreme weather events are likely to occur more often.

Approach

Mesoscale NWP models provide moderate to high resolution of atmospheric phenomena but use parameterizations to depict cloud microphysics determining cloud liquid and ice water amounts. As the models are used to predict future meteorological outcomes, they can provide the information necessary for predicting lightning conditions. Using two mesoscale NWP models, Regional Atmospheric Modeling System (RAMS) and the Weather Research and Forecast model (WRF), we modeled case studies of lightning occurrences to compare lightning potential with actual strikes within the model domain. By testing various configurations of model settings or parameterizations with the case studies, the models are then tuned to the best possible outcome. With WRF this was done using machine learning to test lightning indices' ability to predict lightning during a two-week summertime period. For RAMS, this was done with seven individual cases across months to identify the best overall case for different convective regimes. Tuned model settings were implemented operationally to create statistics over the course of multiple months. These statistics will provide a representation of the overall efficiency of these forecasts based on Type I and Type II errors (false positives and false negative for lightning strikes) for work planners and outdoor workers at SRS. Spatial and temporal errors can be best identified and smoothed by averaging; domain

[1] Yair, Y.; Lynn, B.; Price, C.; Kotroni, V.; Lagouvardos, K.; Morin, E.; Mugnai, A.; Llasat, M. d. C. Predicting the potential for lightning activity in Mediterranean storms based on the Weather Research and Forecasting (WRF) model dynamic and microphysical fields. *J. Geophys. Res.* **2010**, *115*, D04205. DOI: 10.1029/2008JD010868

averages for the temporal errors and 24-hour averages for the spatial errors.

Accomplishments

- Ran greater than 100 RAMS 30-hr simulations, 6 case studies with 20+ variations to model setting, to compare model lightning potential with lightning strikes (**Figure 1**).
- Selected the optimized RAMS settings, determined by minimizing the timing difference between peak model lightning potential and peak number of strikes, to implement a daily operational forecast.
- Implementation of RAMS produced over 200 days of forecasts and 150 days of WRF forecasts.
- Used lightning indices from a physics-based ensemble of two-week simulations of convective environments and observations of cloud-to-ground lightning to calculate the probability of lightning occurrence (**Figure 2**).
- Submitted publication based on WRF lightning forecast potential forecasts using machine learning, currently under revision.
- Collected over 150 days of operational WRF simulations and over 200 days of operational RAMS simulations (ongoing) to develop statistics for testing error and uncertainty and establish a baseline for the limitation of lightning potential forecasts usefulness.

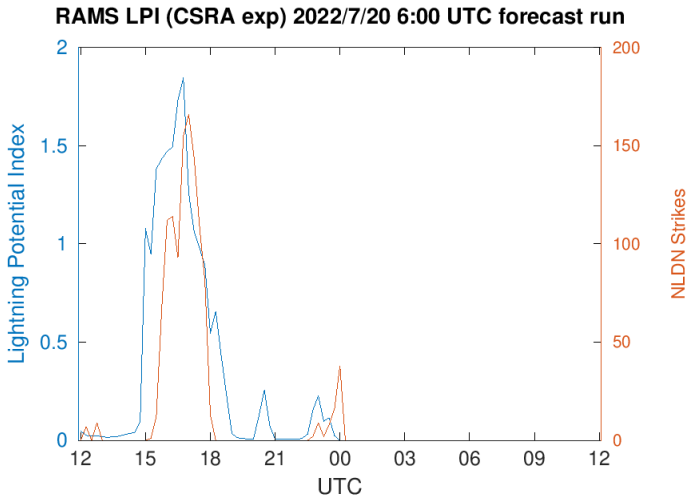

Figure 1. Case study from 20 July 2022 used for determining best RAMS parameterizations.

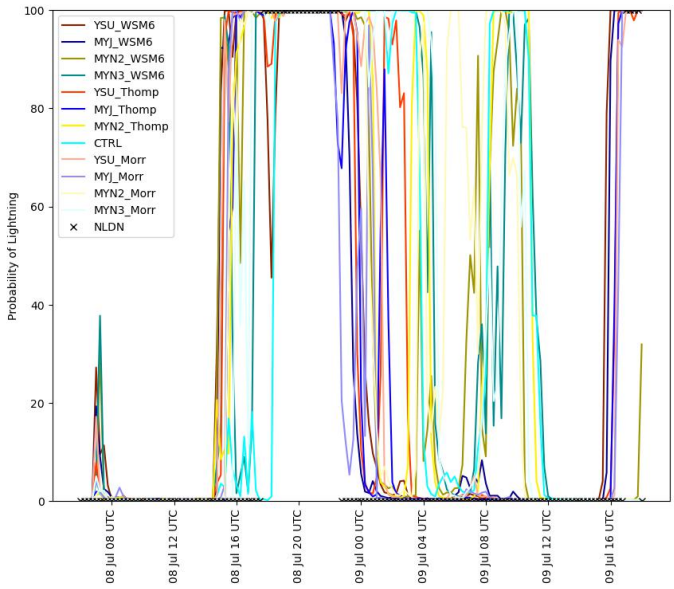

Figure 2. Predicted probabilities of lightning of multiple WRF settings over one week in July 2022.

Peer-reviewed Publications

- Thomas, A.; Noble, S. A Physics-Based Ensemble Machine-Learning Approach to Identifying a Relationship Between Lightning Indices and Binary Lightning Hazard. *Artificial Intelligence for the Earth Systems* **2023** (reviewed, in revision to be resubmitted).

Team Member

Andrew Thomas*

**Postdoctoral Researcher*

Growth and Development of Quantum Materials

Utpal N. Roy

Topological insulators (TIs) are novel states of matter classified as quantum materials. The goal of this project is to find suitable TI materials having robust topological surface states for different dopants/impurities with the capability of tuning the Fermi level. The exotic properties of topological insulators can be used for developing dissipation-less, ultra-fast electronics and quantum computation devices.

Introduction

Topological insulators have a unique characteristic of being an insulator as the bulk property and having conducting surface states. The surface states are symmetry-protected Dirac fermions that are well isolated from the bulk valence and conduction bands. Ideally, these topological surface states and bulk electronic states would act independently. The degree to which they interact depends on the crystalline quality, material composition, and defects present in the material. The goal of this project is to find a suitable TI material with robust topological surface states against doping/impurities, plus the capability of tuning the Fermi level.

Recently Sb_2Te_2Se was reported[1] to have a capability to tune the Fermi level and shows robustness of the topological surface states against impurity doping. Undoped Sb_2Te_2Se was reported as *p*-type, while tin-doped material is an *n*-type material.

We recently grew an undoped Sb_2Te_2Se ingot by the vertical Bridgman technique, which is a melt growth technique. Tin-doped Sb_2Te_2Se has also been grown by the same method. The availability of *p*- and *n*-type material will allow us to fabricate and characterize quantum devices on *p*-*n* junctions. A polished wafer of the as-grown material has been characterized using different tools, including single crystal x-ray diffraction, powder x-ray diffraction and energy dispersive spectroscopy (EDS), to measure the alloy composition and crystallinity. The lattice constant and the Se composition variation along the growth direction were determined to further estimate the composition along the length.

Approach

The approach is to grow topological insulator materials having robust topological surface states against doping/impurities plus the capability of tuning the Fermi level. Thus, control of the material composition and the ability to grow high-quality crystals are required for developing effective topological insulators as quantum devices.

Very recently, Sb_2Te_2Se has been reported1 to have the ability of tuning the Fermi level and having the robustness of topological surface states against impurity doping. The crystals are also capable of tuning the Fermi level by doping with tin to convert the material from p-type to n-type. Undoped Sb_2Te_2Se acts as p-type and tin-doped (about 1 at. %) Sb_2Te_2Se behaves as n-type material. The goal is to grow p-and n-type high-quality Sb_2Te_2Se crystals that would allow us to fabricate quantum devices based on p-n junctions.

We have grown an un-doped Sb_2Te_2Se ingot using the vertical Bridgman growth technique. Crystals have been characterized by single crystal X-ray diffraction and powder X-ray diffraction to analyze the crystal structure and the variation of the lattice constant along the length of the ingot. The data were used to study the extent of the compositional variation along the growth direction. The selenium content is reported to segregate along the

[1] D. Mallick et al. Applied Phys. Lett. 118 (2021) 154001.

growth direction in the Sb_2Te_2Se ingot and concentrate in the last-to-freeze section, which is commonly observed. Energy dispersive spectroscopy (EDS) was also carried out along the length of the grown ingot to further understand the compositional variation and segregation of selenium. **Figure 1a** shows a photograph of the Sb_2Te_2Se ingot of diameter 22mm and about 4.8 cm long. The variation of selenium along the axial direction of the ingot is shown in **Figure 1b**. The surface defects in the image are inconsequential - the EDS measurements were carried out on the wafer cut along the length of the ingot.

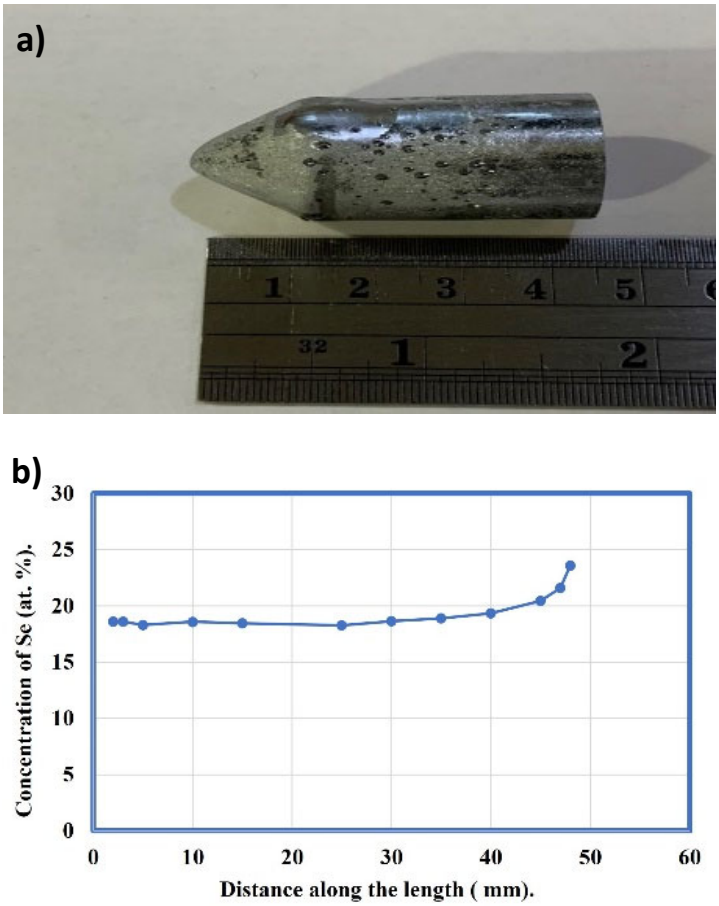

Figure 1: a) Photograph of an undoped Sb_2Te_2Se ingot grown by the vertical Bridgman growth technique, b) selenium concentration along the length of the as-grown ingot.

Accomplishments

- Successfully grew an undoped $Sb_2Te_{3-x}Se_x$ (nominal value is x=1) ingot with a diameter of 22 mm by the vertical Bridgman growth technique.
- Within the accuracy of the measurement method, the EDS results showed a uniform composition along the length of the undoped ingot up to ~4 cm from the tip. After 4 cm, the selenium segregates heavily towards the end of the ingot.
- The powder X-ray diffraction results performed at various lengths of the undoped ingot show similar findings. For example, the calculated lattice constant ("a") at 1.6 cm from the tip and 2.5 cm from the tip were found to be 4.1816 Å and 4.1825 Å, respectively, indicating good uniformity. The corresponding value for the Se composition "x" varied between ~1.00 to 0.99, again indicating good uniformity. Near the end of the ingot (last to freeze), the lattice constant ("a") was 4.1688, and the corresponding value of x was 1.132. Thus, the segregation of selenium near the end of the ingot is more prominent as compared to the rest of the ingot.
- The growth of tin doped Sb_2Te_2Se ingot has been completed by using the vertical Bridgman growth technique. The variation of the composition was similar to the undoped Sb_2Te_2Se ingot. The crystal structure has been determined by the electron diffraction technique. The lattice constant found was a=b= 4.19 Å, c= 29.94 Å with $\alpha = \beta = 90°$ and $\gamma = 120°$ and matches well with the values obtained with un-doped Sb_2Te_2Se ingot as measured by single crystal X-ray diffraction (a=b= 4.2 Å, c= 29.94 Å with $\alpha = \beta = 90°$ and $\gamma = 120°$). The crystal structure was found to be trigonal with the space group R-3m.
- Completed the growth of undoped Sb_2Te_2Se ingot from Te-rich melt. Compositional evaluation is underway.
- Other dopants will also be explored to achieve *n*-type materials.

Team Members

Binod Rai, Henry Ajo, Catherine Housley, Patrick O'Rourke, Robert Lascola, Jonathon Baker, Alex Bretaña*

**Postdoctoral Researcher*

Functionalized Cellular Magmatics

Cory Trivelpiece

Our research focused on creating valuable and economical materials from recycled glass that is typically landfilled. We upcycle this glass by turning it into a synthetic pumice, which is then functionalized via chemical processes to act as filtration media for wastewater and gas streams and/or biological substrates.

Introduction

Approximately 6Mt of glass are disposed of in landfills in the United States annually, which is unfortunate given the nearly infinite recyclability of glass. Much of our efforts are focused on developing novel modified materials, known as engineered cellular magmatics (ECMs), that not only work in laboratory settings but also scale to existing industrial production methods to enable rapid technology transition and commercialization. In the past year, we have incorporated a larger swath of functionalized materials into the ECM portfolio and validated results of the efficacy of these materials at remediating harmful contaminants from environmental ecosystems.

To produce ECMs, we start with washed and crushed glass that was once "curbside" recycled but ultimately ended its lifecycle as waste in a landfill. We have made an evolutionary leap over traditional foamed glass materials made from similar products in the batching process and post-synthesis treatment techniques we apply to the finished materials. In pre-synthesis batching, we utilize small amounts of additives, such as activated carbon or bauxite tailings, to control ECM properties such as chemical composition and mineralogy. By doing so, we introduce surface modifications that enable the remediation of many contaminants of concern from a multitude of potential sources. In post-synthesis functionalization, we either treat the finished product via aqueous or gaseous processing to guide the growth of secondary mineral phases that also are useful at sequestering contaminants, or we utilize the ECMs as substrates for substances like biofilms and biomolecules, which have efficacy at remediating waste streams through biological processes.

Approach

In the final year of this work, we focused on expanding the functionality of ECMs by incorporating novel biomolecules to the surfaces of the materials. In addition to this expanded range of secondary treatment options, we focused on developing a model framework for predicting the processability of materials into ECMs.

Much of this year's studies focused on determining the various types and amounts of biomolecules that could be "grown" on the ECM surface. These included investigating the growth of lipids, carbohydrates, and proteins that have uses in various applications such as antibiotics and catalysis. Similar to the success we had with biofilms consisting of living bacterial consortiums in previous years, we utilized industrially available growth media and cryopreservation techniques to establish the usefulness of these materials from an industrial perspective.

Our computational/predictive efforts focused on utilizing first-principle materials science concepts to develop a model that could accurately predict glass and glass-ceramic foam density based on glass composition. We combined glass science computational methods available through GlassPy[1] with models describing bubble growth and release to develop a model that accurately predicts a glass or glass ceramic foam density. From this predicted property, we can determine quantities such as porosity, processing temperature, and pore size distribution, which impact the processing of these novel materials from bench to industrial scale.

[1] Cassar, D., GlassNet: a multitask deep neural network for predicting many glass properties. arxiv 2023.

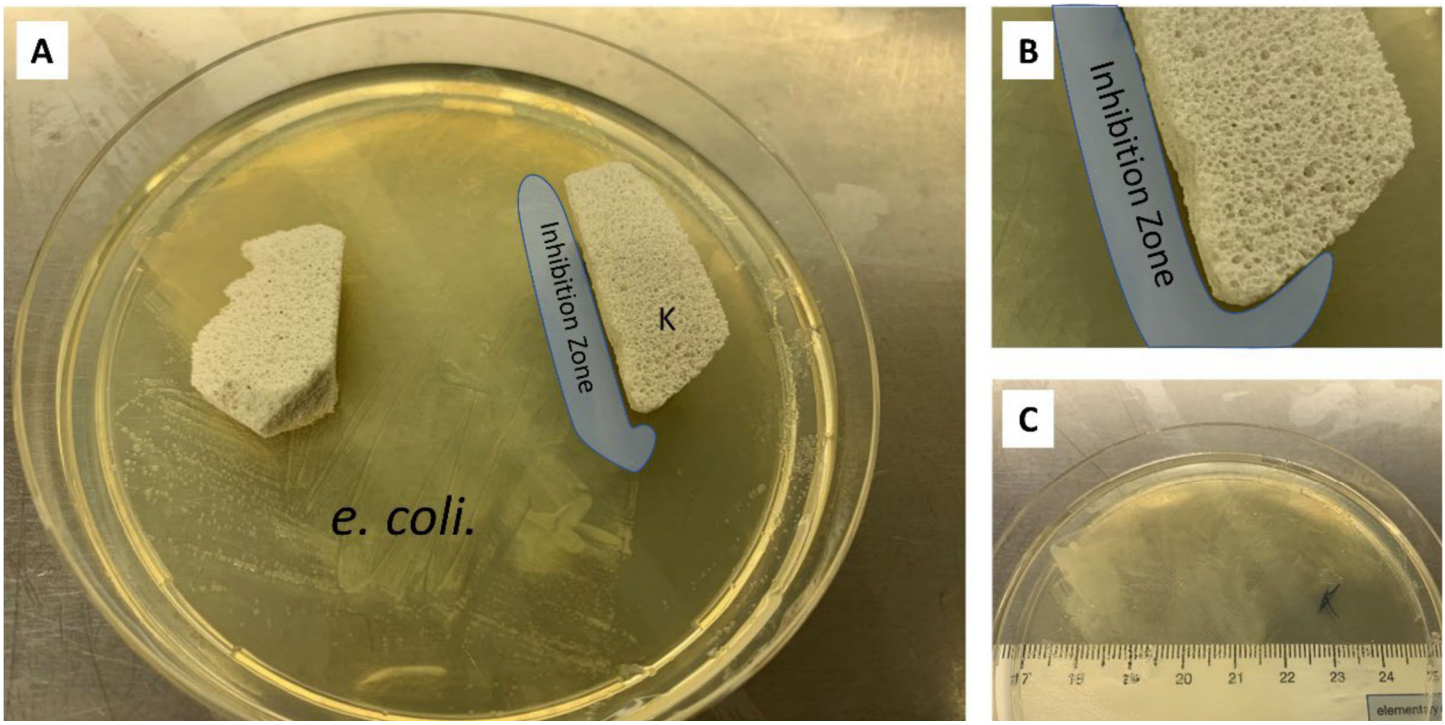

Figure 1. A and B. Kanamycin (K, antibiotic) treated samples showing a typical zone of inhibition where the preserved ECM was placed in the presence of e. coli. C. The growth media with the ECM removed showing the zone of inhibition.

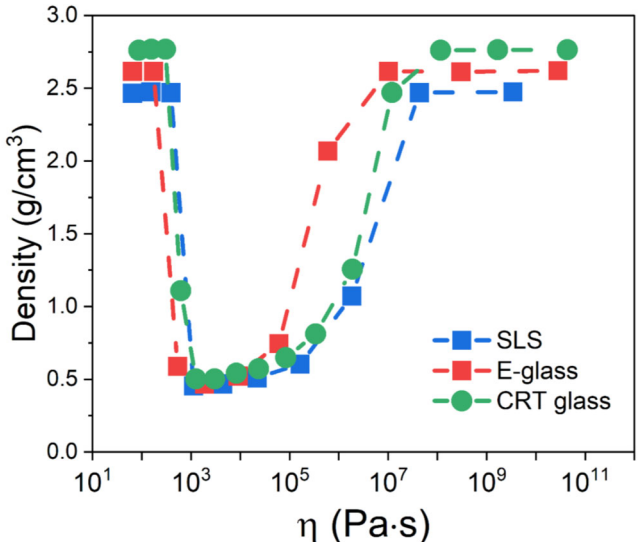

Figure 2. Prediction of foam density versus the composition-dependent viscosity of various types of glass currently identified for ECM feedstocks.

Accomplishments

The major accomplishments of the past year's work are summarized in two points:

- The successful incorporation, cryopreservation, and reactivation of biomolecules on a commercially viable ECM composition.
  - **Figures 1A-C** demonstrate the effect of a carbohydrate biomolecule present on an ECM on stopping the advance of E. coli in a standard gel growth media versus the growth of these bacteria in a control sample.
- The development of a model that successfully predicts the density of a glass foam based on glass composition.
  - **Figure 2** shows the prediction of glass density when incorporated with a foaming agent versus the viscosity of the glass, which is directly proportional to the processing temperature at which the material is synthesized. Based on these predictions, we can control pore size, total porosity, and glass density during the synthesis process, demonstrating another stark difference between traditional foam glass and ECMs.

Peer-reviewed Publications

- Kugler, A., Trivelpiece, C. & Brigmon, R.L. Foamed glass ceramics—an upcycled scaffold for microbial biofilm development. *Biotechnol Lett,* **2023**, *45*, 225–233.
- Trivelpiece, C. et. al. A Novel Approach to Zeolite Synthesis and Support Using Upcycled Waste Glass. *Materials Today Sustainability* (under review).

Intellectual Property

- Brigmon, R. Kugler, A. Trivelpiece, C. "Engineered Micromagmatics for Deploying Microorganisms." USPTO Application No. 18/317,314.
- Kugler, A. Trivelpiece, C. "Biomolecular Material and Related Methods." USPTO Application No. 18/478,133.

Team Members

Will Jolin, Alex Kugler, Madison Hsieh, Catherine Housley, Anna Stanfield, Collin Wilkinson[a], W. Taylor Adams, Bryce Brechin, Christopher Verst, Austin Stanfield[a], Nate Lousy[a], Eric McCaslin[a], Jackson DeVault[+], Logan Howell[+], Vasilii Maxsimov[a+]

[a]Alfred University
[+]Undergraduate Student

Gamma Radiation Protected Self-Healing Polymer Composite

Thanh-Tam Truong

This research developed self-healing coatings suitable for radiation environments through incorporation of microcapsules containing liquid healing agent and high-attenuation coefficient nanoparticles. The self-healing polymer system exhibits autonomous crack repair, prolonging coating service life and reducing replacement costs.

Introduction

Polymeric materials, ubiquitous in industrial applications such as healthcare, nuclear, and aerospace, are susceptible to damage from radiation-induced degradation. Microcapsule (MC)-based self-healing polymers are one approach to increase the service life of these materials. When polymer coatings with MCs are damaged, the ruptured MCss release healing agent that flows into the crack to repair the damage, as shown in **Figure 1**. This restores the properties of the polymer coating and mitigates loss of corrosion protection, thereby lengthening the service life and consequently reducing costs associated with maintenance or replacement. As gamma photons can cause premature curing of the healing agent contained within MCss, the MC shell was fortified with nanoparticles with high attenuation coefficients. A key part of this project was developing a synthesis procedure for incorporating nanoparticles, with high atomic number, into the microcapsule wall while maintaining sufficient levels of healing agent within the MC core. Epoxy films containing dispersed MCs were developed to evaluate their ability to self-repair. Developing an MC-based self-healing polymer system that retains self-healing functionality under gamma radiation will be a first in the field of self-healing polymers.

Approach

For MCs to be useful in a self-healing coating, the healing agent must be flowable and encased in a robust shell. For this project, an epoxy similar to the polymer film matrix was chosen as the healing agent and the MC shell was composed of poly(urea formaldehyde) (PUF). PUF MCs are sufficiently resilient to withstand processing steps during film preparation while being brittle enough to rupture and release healing agent when the film is scratched. Unmodified tungsten (VI) oxide (WO_3) nanomaterial and WO_3 nanomaterial modified with poly(ethylene oxide) were incorporated into PUF MCs and the synthesis procedure was optimized to increase the loading of nanoparticles while maintaining high healing agent encapsulation efficiency. Modified WO_3 nanoparticles were necessary to achieve even incorporation into PUF MCs. **Table 1** lists the properties of the synthesized MCs, and the modified WO_3/PUF MCs have both the highest encapsulation efficiency at 48% and WO_3 nanoparticle loading at 3.5 wt.%. Epoxy films were cured with 20 wt.% modified WO_3/PUF microcapsules on carbon steel plates, a material susceptible to corrosion. After scribing the film with a scalpel, self-healing performance was assessed visually after 24 hr salt exposure, as shown in **Figure 2**. The epoxy film without MCs was corroded along the cracks while the film with WO_3/PUF MCs self-healed and remained mostly

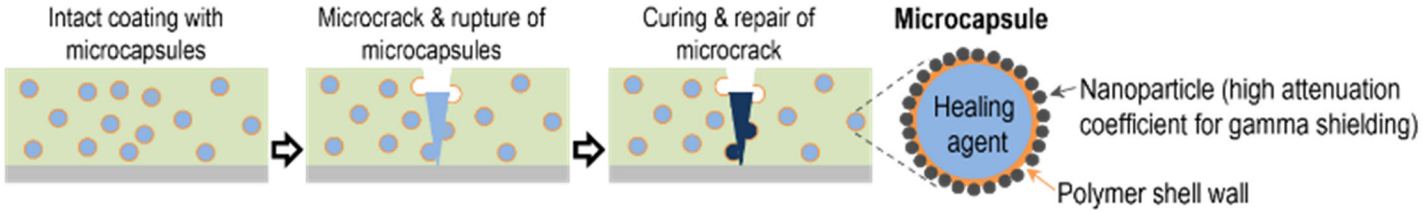

Figure 1. Schematic of self-healing in a microcapsule-based coating system. Inset: components of synthesized microcapsule.

corrosion-free and, thus, retained its corrosion protection property.

Both MCs fortified with modified WO_3 (WO_3/PUF) and MCs containing no nanoparticles (control) were exposed to gamma radiation from a Co-60 source at a dose rate of ~50 kRad/hr in 10,000 min increments. After irradiation, the encapsulation efficiency for the MCs was measured and compared to initial values to determine the loss in encapsulation efficiency. As shown in **Figure 3**, WO_3/PUF MCs were more resistant to gamma-induced degradation of the epoxy healing agent core compared to the control MCs. Thus, WO_3 nanoparticles in the MC shell mitigated the curing of epoxy healing agent within the MC core.

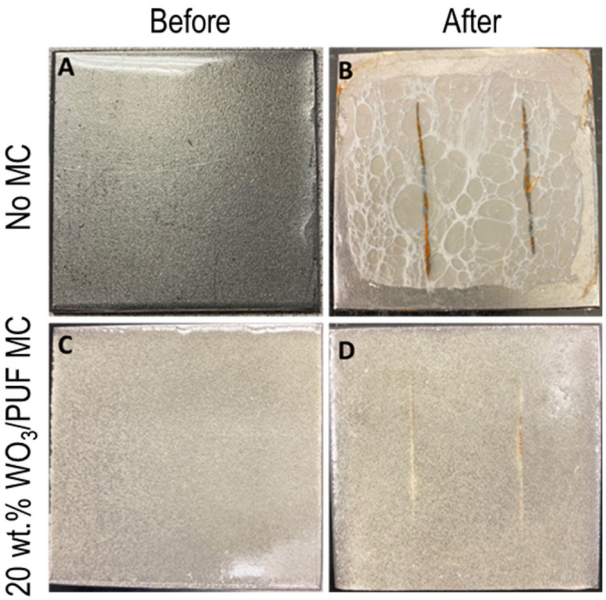

Figure 2. Corrosion test results for carbon steel plates with no-microcapsules and 20 wt.% microcapsules-embedded epoxy coatings. Pictures of samples before (A) and after (B) scribing and salt exposure for epoxy coating without microcapsules, and before (C) and after (D) scribing and salt exposure for microcapsule embedded coating.

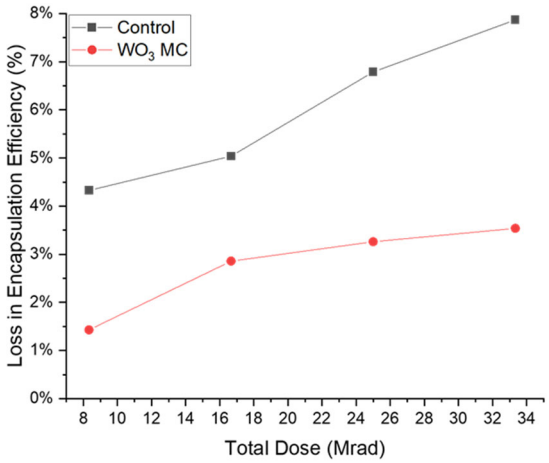

Figure 3: Loss in epoxy healing agent encapsulation efficiency vs. total radiation dose for control PUF MC and WO_3/PUF MC.

Samples	WO_3 in MC (wt.%)	Average Diameter (μm)	Encapsulation Efficiency
PUF MC	0%	102 ± 31.3	44% ± 1%
WO_3/PUF MC	2.0% ± 0.1%	125 ± 28.8	46% ± 1%
Modified WO_3/PUF MC	3.5% ± 0.1%	117 ± 31.4	48% ± 1%

Table 1. Properties of synthesized microcapsules

Accomplishments

- Optimized homogenous inclusion of tungsten (VI) oxide nanoparticles into PUF. MCs; increased nanoparticle content to approximately 3.4% of MC total weight.
- Prepared MC-containing epoxy films on carbon steel and verified ability of films to self-heal and retain corrosion protection properties after physical damage.
- Demonstrated a ~50% reduction in gamma induced degradation of the epoxy healing agent core in MCs fortified with tungsten oxide nanoparticles.

Peer-reviewed Publications

- Preparation and characterization of tungsten oxide fortified poly(urea-formaldehyde) microcapsules for self-healing coatings – Submitted to Progress in Organic Coatings

Team Members

W. Taylor Adams, Bryce Brechin, Christopher Verst, Meryl Wiratmo[+]

[+]*Undergraduate Intern*

FY23 PROJECTS

CORE COMPETENCY:

Assuring production and supply of strategic materials and components

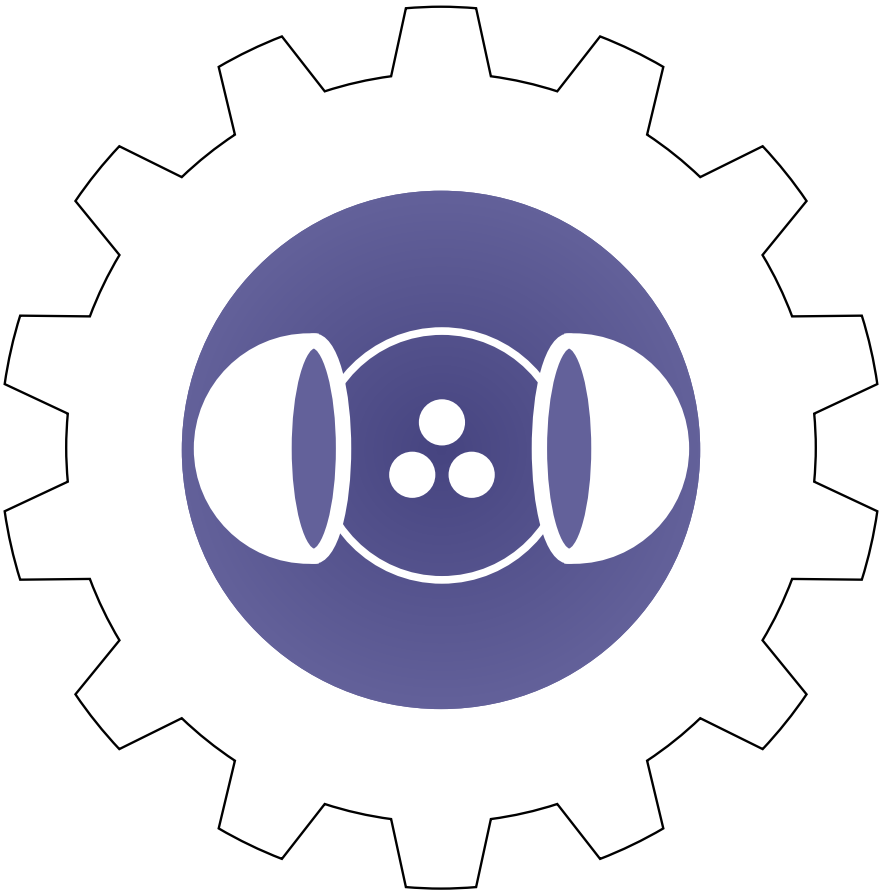

Advanced Modeling of Tritium Embrittlement in Stainless Steels

Eric Hoar

This research project focuses on the use of artificial intelligence and machine learning algorithms to predict the mechanical properties of stainless steel. The model attempts to identify failure trends by predicting the reduction in mechanical properties due to embrittlement. This understanding is essential for predicting the limits of tritium infrastructure.

Introduction

Austenitic stainless steels are structural materials utilized in vessels for the storage of tritium gas due to the steel's high resistance to hydrogen isotope embrittlement [1-3]. However, as tritium decays helium is created in the material, which leads to increased embrittlement effects. **Figure 1** illustrates how both the microstructure and charging environment can affect the mechanical properties of stainless steel [4]. Due to the increase in embrittlement effects caused by tritium decay it is important for tritium facilities to understand the limitations of stainless steels in this environment. SRNL has over twenty years of experience identifying these embrittlement effects. However, there has been limited effort in the development of a model capable of predicting the mechanical properties of austenitic stainless steel after tritium charging. Therefore, due to the availability of a large tritium embrittlement dataset, machine learning algorithms provide an opportunity to develop a data-driven model of embrittlement in stainless steels.

Approach

The approach used in this project was to train a machine learning model, using the available SRNL and literature embrittlement data, to predict the fracture toughness of stainless steel as a function of tritium content. The database created will be a conglomerate of multiple datasets and, as such, will need to be curated so the data can be compared to each other. Through discussions with experts, it was identified that the stainless-steel composition, hydrogen-isotope content, helium content, and testing environment (i.e., pressure and temperature) would be key parameters for the model. The machine learning algorithms were built using the python language and the open source scikit, scipy, and numpy libraries. These libraries provide pre-built functionality that greatly reduce the number of custom-built functions required for model development. The embrittlement database will be divided into training and testing datasets with an 80-20 split, respectively. Multiple models will be developed and trained to identify the most optimal machine learning algorithm for the data. These models include decision tree (DT), random forest (RF), and Gaussian process regression (GPR) models. These algorithms require a different amount of training data to be viable and, as such, it is expected that some will show good predictive ability while others will not. Model performance will be described using the coefficient of determination (R^2) to identify the model's ability to characterize the variability of the training data and the mean average percent error to identify the model's ability to accurately predict the desired outputs.

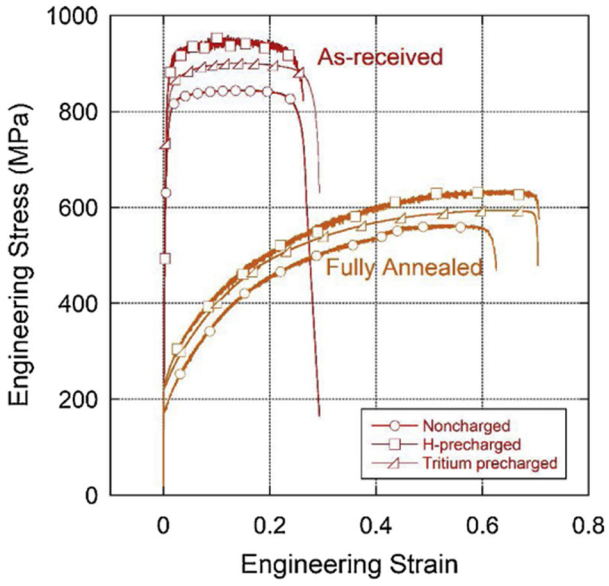

Figure 1. Comparison of stress-strain curves for stainless steel samples of the same composition charged in various environments and with different microstructures.

P	S	N	Co	O	Al	Composition units	Charge Type	Exposure Temp	Exposure Temp units	Over-pressure	Over-pressure units	Age Time	Age Time units	Age Temp	Age Temp units	Testing Environment	Testing Pressure	Testing Pressure units	Testing Temp	Testing Temp units	sotope Cont	He Content	Content units
0.014	0.011	0	0	0	0	wt%	None - He	-	-	-	-	-	-	-	-	None	-	-	293	K	0	0	wppm
0.014	0.011	0	0	0	0	wt%	None - H	-	-	-	-	-	-	-	-	Hydrogen	69	MPa	293	K	0	0	wppm
0.0225	0.015	0	0	0	0	wt%	None	-	-	-	-	-	-	-	-	None	-	-	293	K	0	0	wppm
0.0225	0.015	0	0	0	0	wt%	Hydrogen - H	293	K	34	MPa	24	h	-	-	Hydrogen	34	MPa	293	K	-	0	wppm
0.0225	0.015	0	0	0	0	wt%	Hydrogen - H	293	K	69	MPa	24	h	-	-	Hydrogen	69	MPa	293	K	-	0	wppm
0	0	0	0	0	0	wt%	None	-	-	-	-	-	-	-	-	None	-	-	293	K	0	0	wppm
0	0	0	0	0	0	wt%	Hydrogen - H	473	K	24.1	MPa	240	h	-	-	Hydrogen	69	MPa	293	K	55	0	wppm
0.0225	0.015	0	0	0	0	wt%	None	-	-	-	-	-	-	-	-	None	-	-	293	K	0	0	wppm
0.0225	0.015	0	0	0	0	wt%	Hydrogen	293	K	69	MPa	-	-	-	-	None	-	-	293	K	-	0	wppm
0.0225	0.015	0	0	0	0	wt%	None	-	-	-	-	-	-	-	-	None	-	-	293	K	0	0	wppm
0.0225	0.015	0	0	0	0	wt%	None - He	-	-	-	-	-	-	-	-	None	-	-	293	K	0	0	wppm
0.0225	0.015	0	0	0	0	wt%	None - H	-	-	-	-	-	-	-	-	Hydrogen	69	MPa	293	K	0	0	wppm
0	0	0.25	0	0	0	wt%	None	-	-	-	-	-	-	-	-	None	-	-	293	K	0	0	wppm
0	0	0.25	0	0	0	wt%	Hydrogen - H	473	K	24.1	MPa	240	h	-	-	Hydrogen	69	MPa	293	K	-	0	wppm
0.0225	0.015	0.13	0	0	0	wt%	None - He	-	-	-	-	-	-	-	-	None	-	-	293	K	0	0	wppm
0.0225	0.015	0.13	0	0	0	wt%	None - H	-	-	-	-	-	-	-	-	Hydrogen	69	MPa	293	K	0	0	wppm
0.3	0.025	0.25	0	0	0	wt%	None	-	-	-	-	-	-	-	-	None	-	-	293	K	0	0	wppm
0.3	0.025	0.25	0	0	0	wt%	None - He	-	-	-	-	-	-	-	-	None	-	-	293	K	0	0	wppm
0.3	0.025	0.25	0	0	0	wt%	None - H	-	-	-	-	-	-	-	-	Hydrogen	69	MPa	293	K	0	0	wppm
0.3	0.025	0.25	0	0	0	wt%	Hydrogen	430	K	69	MPa	1000	h	-	-	None	-	-	293	K	-	0	wppm
0.3	0.025	0.25	0	0	0	wt%	Hydrogen - H	430	K	69	MPa	1000	h	-	-	Hydrogen	69	MPa	293	K	-	0	wppm
0.015	0.008	0	0	0	0	wt%	None	-	-	-	-	-	-	-	-	None	-	-	380	K	0	0	wppm
0.015	0.008	0	0	0	0	wt%	Hydrogen	470	K	69	MPa	35000	h	-	-	None	-	-	380	K	-	0	wppm
0.015	0.008	0	0	0	0	wt%	None	-	-	-	-	-	-	-	-	None	-	-	273	K	0	0	wppm
0.015	0.008	0	0	0	0	wt%	Hydrogen	470	K	69	MPa	35000	h	-	-	None	-	-	273	K	-	0	wppm
0.015	0.008	0	0	0	0	wt%	None	-	-	-	-	-	-	-	-	None	-	-	200	K	0	0	wppm
0.015	0.008	0	0	0	0	wt%	Hydrogen	470	K	69	MPa	35000	h	-	-	None	-	-	200	K	-	0	wppm
0.015	0.008	0	0	0	0	wt%	None - N	-	-	-	-	-	-	-	-	None	-	-	77	K	0	0	wppm
0.015	0.008	0	0	0	0	wt%	Hydrogen - N	470	K	69	MPa	35000	h	-	-	None	-	-	77	K	-	0	wppm
0.0225	0.015	0	0	0	0	wt%	None	-	-	-	-	-	-	-	-	None	-	-	380	K	0	0	wppm
0.0225	0.015	0	0	0	0	wt%	Hydrogen	620	K	69	MPa	500	h	-	-	None	-	-	380	K	-	0	wppm
0.0225	0.015	0	0	0	0	wt%	None	-	-	-	-	-	-	-	-	None	-	-	298	K	0	0	wppm
0.0225	0.015	0	0	0	0	wt%	Hydrogen	620	K	69	MPa	500	h	-	-	None	-	-	298	K	-	0	wppm
0.0225	0.015	0	0	0	0	wt%	None	-	-	-	-	-	-	-	-	None	-	-	250	K	0	0	wppm
0.0225	0.015	0	0	0	0	wt%	Hydrogen	620	K	69	MPa	500	h	-	-	None	-	-	250	K	-	0	wppm
0.0225	0.015	0	0	0	0	wt%	None	-	-	-	-	-	-	-	-	None	-	-	200	K	0	0	wppm
0.0225	0.015	0	0	0	0	wt%	Hydrogen	620	K	69	MPa	500	h	-	-	None	-	-	200	K	-	0	wppm
0.3	0.025	0.25	0	0	0	wt%	None	-	-	-	-	-	-	-	-	None	-	-	375	K	0	0	wppm
0.3	0.025	0.25	0	0	0	wt%	Deuterium	620	K	69	MPa	500	h	-	-	None	-	-	375	K	-	0	wppm
0.3	0.025	0.25	0	0	0	wt%	None	-	-	-	-	-	-	-	-	None	-	-	298	K	0	0	wppm
0.3	0.025	0.25	0	0	0	wt%	Deuterium	620	K	69	MPa	500	h	-	-	None	-	-	298	K	-	0	wppm
0.3	0.025	0.25	0	0	0	wt%	None	-	-	-	-	-	-	-	-	None	-	-	245	K	0	0	wppm
0.3	0.025	0.25	0	0	0	wt%	Deuterium	620	K	69	MPa	500	h	-	-	None	-	-	245	K	-	0	wppm
0.3	0.025	0.25	0	0	0	wt%	None	-	-	-	-	-	-	-	-	None	-	-	220	K	0	0	wppm
0.3	0.025	0.25	0	0	0	wt%	Deuterium	620	K	69	MPa	500	h	-	-	None	-	-	220	K	-	0	wppm
0.3	0.025	0.25	0	0	0	wt%	None	-	-	-	-	-	-	-	-	None	-	-	200	K	0	0	wppm
0.3	0.025	0.25	0	0	0	wt%	Deuterium	620	K	69	MPa	500	h	-	-	None	-	-	200	K	-	0	wppm
0.017	0.012	0.04	0	0	0	wt%	None	-	-	-	-	-	-	-	-	None	-	-	293	K	0	0	wppm
0.017	0.012	0.04	0	0	0	wt%	None - H	-	-	-	-	-	-	-	-	Hydrogen	69	MPa	293	K	0	0	wppm

Figure 2. Subset of the new embrittlement database illustrating the inclusion of testing temperature and pressure.

Accomplishments

Model results were presented at the 2023 ANS Annual Meeting on June 12, 2023, in the Advanced/Additive Manufacturing: 1 section.

- The manuscript "Machine Learning Prediction of Fracture Toughness in Hydrogen-charged Stainless Steels" was published in the peer-reviewed *Transactions* conference proceedings.

Model development and results were presented at the 1st BSRA Computing Exchange on March 30, 2023.

- Presentation was given to both current SRNL employees as well as BSRA university partners to foster collaborations between SRNL and the universities.

An expansive literature review was performed which identified "embrittlement index" as a measurement of interest.

- Many publications had measured embrittlement by calculating the embrittlement index of the material. This was done by comparing the reduced property value to the property value of the as received material.
- This illustrated the need to convert the SRNL data to "embrittlement index" values in order to greatly expand the database size.

Converted and expanded the embrittlement database to include embrittlement index data obtained from literature.

- The expanded embrittlement index database is twice the size of the original embrittlement data repository.
- **Figure 2** shows a subset of the new database, which considers both hydrogen and tritium content as a combined "H-isotope" variable.

Developed a new machine learning methodology utilizing the embrittlement index database to predict the embrittlement index as a function of material composition, testing environment, H-isotope content, and He content.

- This included the inclusion of code to calculate the H-isotope content as a function of environment.
- The new models were also developed to predict either embrittlement index calculated using elongation data (EI_el) or the embrittlement index calculated using reduction of area data (EI_ra). These data types are common in hydrogen embrittlement literature.
- The SRNL experimental data was combined with both the EI_el & EI_ra data by calculating the embrittlement index using fracture toughness (**Table 1**).

Algorithm	EI_el		EI_ra	
	R^2	$\%_{error}$ (%)	R^2	$\%_{error}$ (%)
DT	0.9907	11.0621	1.0	10.9890
RF	0.9857	11.2143	0.9755	24.7595
GPR	0.9908	51.3915	0.7172	47.0689

Table 1. Comparison of R^2 and average percent error for the prediction of the elongation embrittlement index and the reduced area embrittlement index for each of the developed models including the decision tree, random forest, and gaussian process regression models.

Error analyses were performed on each of the developed models to identify the trained model's fit to the training data and predictive ability for new data points.

- Comparison plots for each of the different models are illustrated in **Figures 3-8**.
- The DT model (**Figures 3 & 4**) provides a good predictive ability with high R^2 values of 0.9907 and 1.0 as well as low mean average percent errors of 11.061% and 10.9890% for EI_el and EI_ra, respectively. However, from Figures 3 & 4 it can be identified that the DT model can be overfitting the training dataset.
- The RF model (**Figures 5 & 6**) also provides good predictive ability with high R^2 values of 0.9857 and 0.9755 as well as low mean average percent errors of 11.2143% and 24.7595% for EI_el and EI_ra, respectively. **Figures 5 & 6** also show some possible overfitting though to a lesser degree than the DT model.
- The GPR model (**Figures 7 & 8**) provides the worst predictive ability of the three model algorithms with R^2 values of 0.9908 and 0.7172 and high mean average percent errors of 51.3915% and 47.0689% for EI_el and EI_ra, respectively. The high percent error could be due to the relatively low amounts of data available for training the model.

Peer-reviewed Publications

- Hoar, E.; Hitchcock, D.; Krentz, T.; Roy, L. Machine Learning Prediction of Fracture Toughness in Hydrogen-charged Stainless Steels. *ANS 2023 Annual Meeting Transactions*. **2023**, 338-341. DOI: 10.13182/T128-41910
- Hoar, E.; Hitchcock, D.; Krentz, T.; Roy, L. Machine Learning Prediction of Fracture Toughness in Hydrogen-charged Stainless Steels. *ANS 2023 Annual Meeting*, June 2023. (oral presentation).

Team Members

Dale Hitchcock, Timothy Krentz, Lindsay Roy

References

1. Caskey Jr, G. Tritium-helium Effects in Metals. *Fusion Technology* **1985**, vol 8, 2293-2298.
2. Morgan, M. J.; Tosten, M. H. Tritium Effects on Weldment Fracture Toughness. *Savannah River National Laboratory,* **2006**. WSRC-STI-2006-00056.
3. Morgan, M. J.; Hitchcock, D. A.; Krentz, T. M; West, S. L. Tritium Aging Effects on Fracture Toughness of Stainless Steel Weldments. *Fusion Science and Technology*, **2020**, 76:3, 209-214. DOI:10.1080/15361055.2019.1704138
4. Krentz, T. M.; Ronevich, J. A.; Balch, D. K.; San Marchi, C. Tritium Embrittlement of Austenitic Stainless-Steel Tubing at Low Helium Contents. *Fusion Engineering and Design* **2021**, 168: 112413.
5. Morgan, M. J.; West, S. L.; Chapman, G. K. Tritium Aging Effects on Fracture Toughness of Type 21-6-9 Stainless Steel. *Savannah River National Laboratory*, **2007**. WSRC-TR-2007-00244.

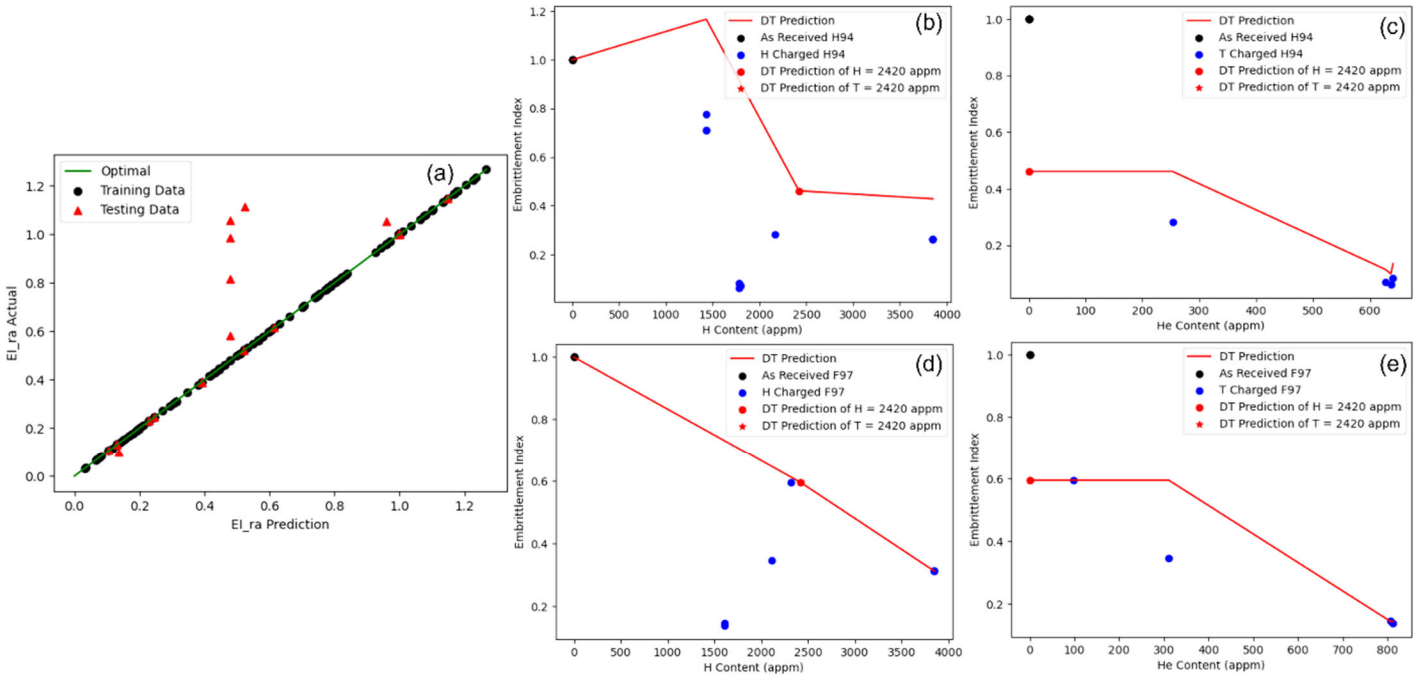

Figure 3. Comparison plots showing the results of the DT model for the prediction of EI_el. Plot (a) compares the predicted and actual embrittlement index. Plots (b) and (c) show the H content vs embrittlement index and He content vs embrittlement index respectively for the H94 samples [5]. Plots (d) and (e) show the H content vs embrittlement index and He content vs embrittlement index respectively for the F97 samples [5].

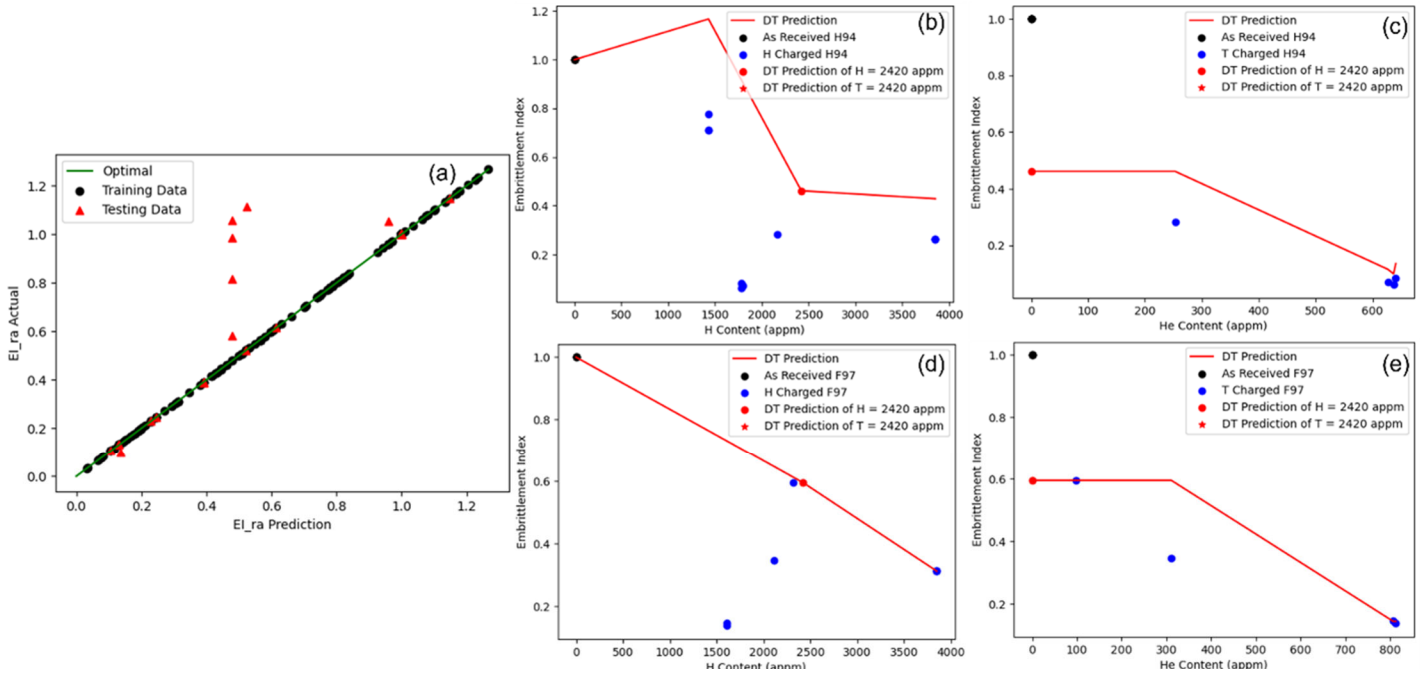

Figure 4. Comparison plots showing the results of the DT model for the prediction of EI_ra. Plot (a) compares the predicted and actual embrittlement index. Plots (b) and (c) show the H content vs embrittlement index and He content vs embrittlement index respectively for the H94 samples [5]. Plots (d) and (e) show the H content vs embrittlement index and He content vs embrittlement index respectively for the F97 samples [5].

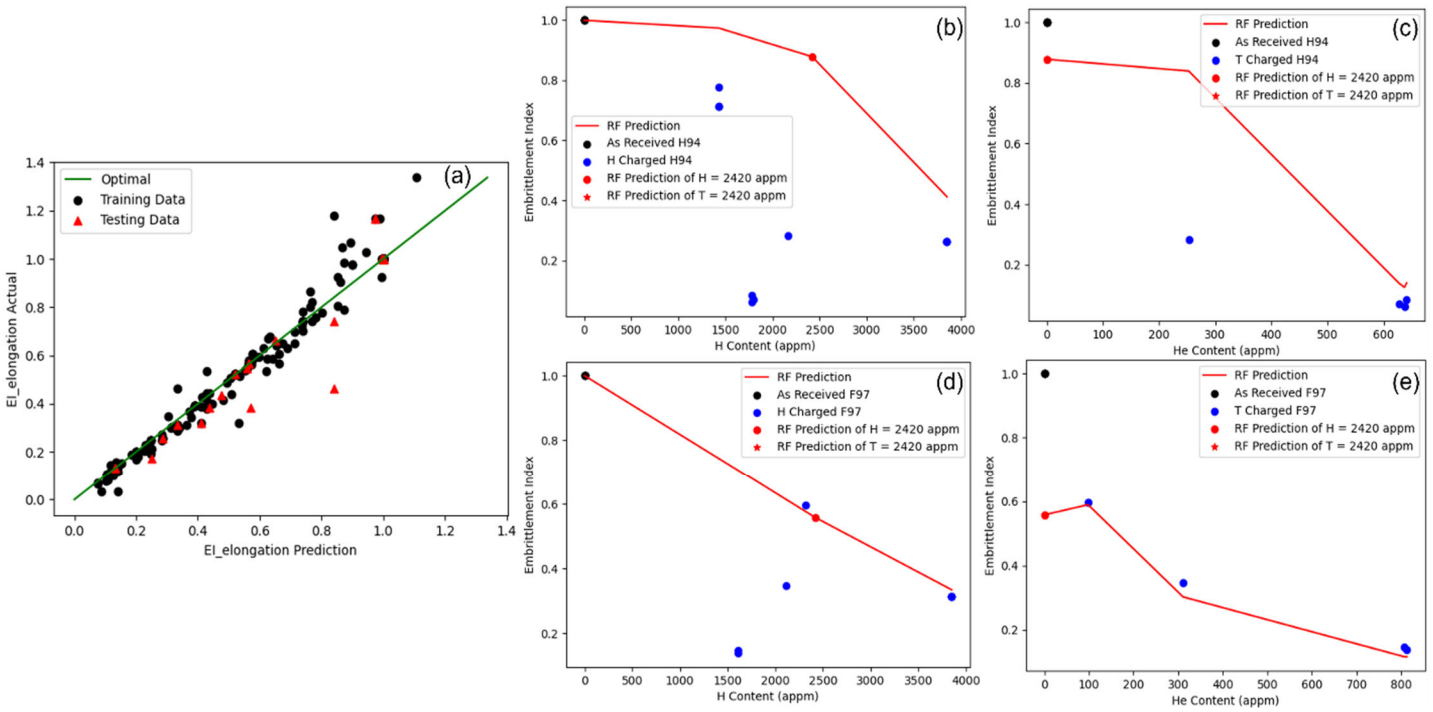

Figure 5. Comparison plots showing the results of the RF model for the prediction of EI_el. Plot (a) compares the predicted and actual embrittlement index. Plots (b) and (c) show the H content vs embrittlement index and He content vs embrittlement index respectively for the H94 samples [5]. Plots (d) and (e) show the H content vs embrittlement index and He content vs embrittlement index respectively for the F97 samples [5].

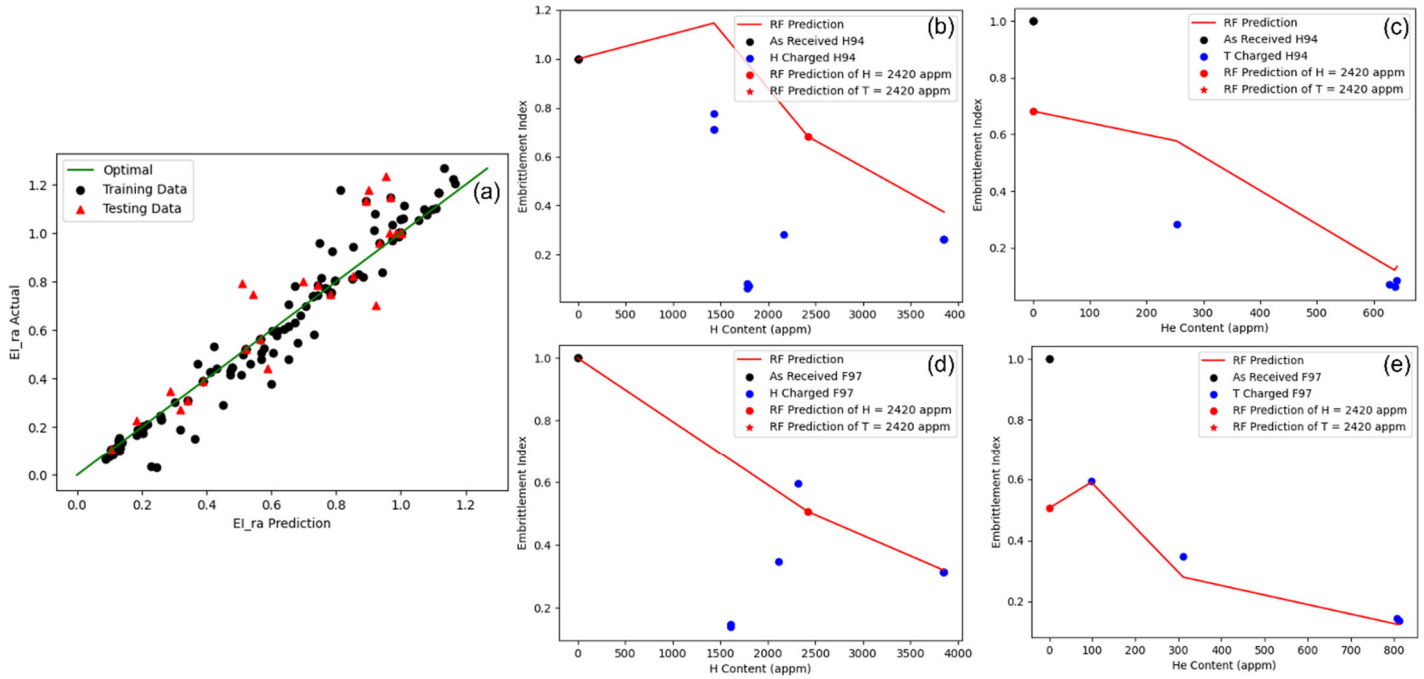

Figure 6. Comparison plots showing the results of the RF model for the prediction of EI_ra. Plot (a) compares the predicted and actual embrittlement index. Plots (b) and (c) show the H content vs embrittlement index and He content vs embrittlement index respectively for the H94 samples [5]. Plots (d) and (e) show the H content vs embrittlement index and He content vs embrittlement index respectively for the F97 samples [5].

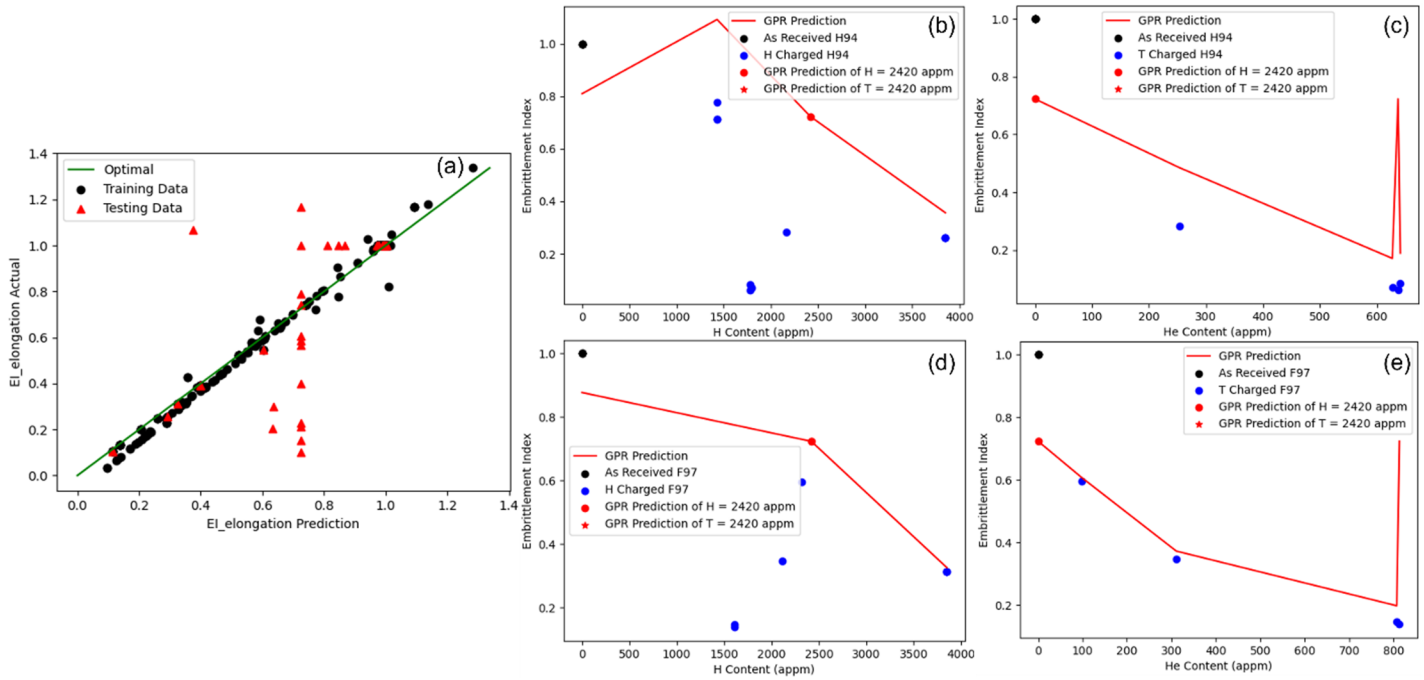

Figure 7. Comparison plots showing the results of the GPR model for the prediction of EI_el. Plot (a) compares the predicted and actual embrittlement index. Plots (b) and (c) show the H content vs embrittlement index and He content vs embrittlement index respectively for the H94 samples [5]. Plots (d) and (e) show the H content vs embrittlement index and He content vs embrittlement index respectively for the F97 samples [5].

FY23 PROJECTS

CORE COMPETENCY:

Enabling next-generation nuclear materials processing and disposition

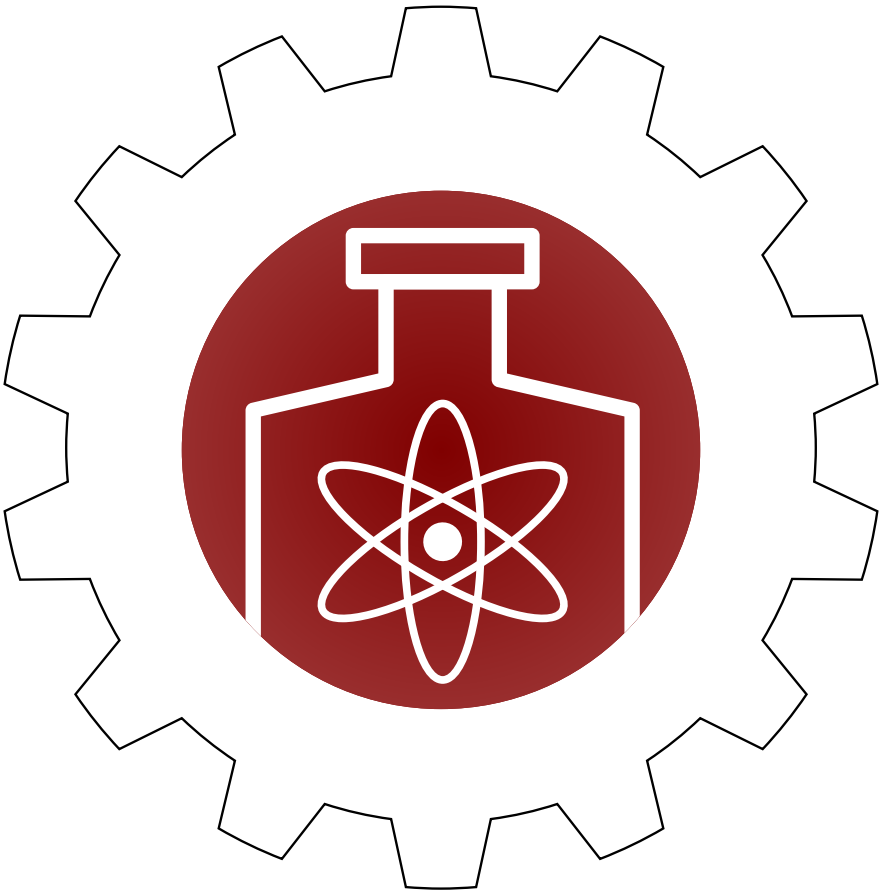

Tritium and Radiation-resistant Silicone Membranes Through Tailored Phenyl Content

Tyler Guin

The lack of tritium-compatible elastomers complicates tritium processing and is a technology barrier for fusion power. This project explores phenyl silicone elastomers as potentially tritium-resistant elastomers. Initial results suggest that they may be tritium resistant, and surprisingly may be among the most gamma radiation-stable elastomers.

Introduction

Prior work from SRNL has demonstrated that polymers perform extremely poorly in contact with tritium, either turning into "goo" from chain scission or brittle char from crosslinking. Conventional inert polymers, such as PTFE, are not resistant to tritium, as the activation energy induced by the beta decay is orders of magnitude higher than conventional chemical bond energy. While most polymers are not resistant to tritium, prior work from SRNL has demonstrated that highly aromatic polymers such as polyimides have relatively good tritium resistance. However, polyimides are not useful for many barrier applications as they are inflexible and difficult to process.

Synergistically, recent work from SRNL has explored the use of phenyl-silicone oils for use in high-rad environments, and these oils demonstrated exceptional resistance to gamma irradiation and deuterium isotope exchange. In contrast to traditional methyl silicones, phenyl silicone oil contains 89 wt% phenyl content, which provides exceptional radical stability. Importantly, it is possible to synthesize longer chain polymers with equivalent chemical structures through organo-silane chemistry.

Prior work has explored the gamma radiation resistance of phenyl silicones, focusing on changes in thermomechanical properties. As expected, phenyl content positively correlates with radiation stability. However, the viability of phenyl silicones in this application is unknown as there are significant gaps in the open literature:

1) All prior work has utilized carbon-carbon crosslinking chemistry.
2) The gas permeation has not been explored as a function of radiation exposure or deuterium exchange.
3) The radiation-induced isotope exchange of phenyl silicones has never been reported.

Approach

Silicone elastomers are traditionally synthesized as an oligomeric oil, terminated with cross-linkable vinyl moieties. These vinyl moieties convert to C-C bonds, which represent radiological weaknesses in the molecular structure. However, without these groups, the crosslinking occurs through removal of water (see **Figure 1**), which must permeate through the elastomer during curing. This can induce voids and defects. Therefore, the first step of the project was to develop a tunable synthesis methodology which enables crosslinking without vinyl groups.

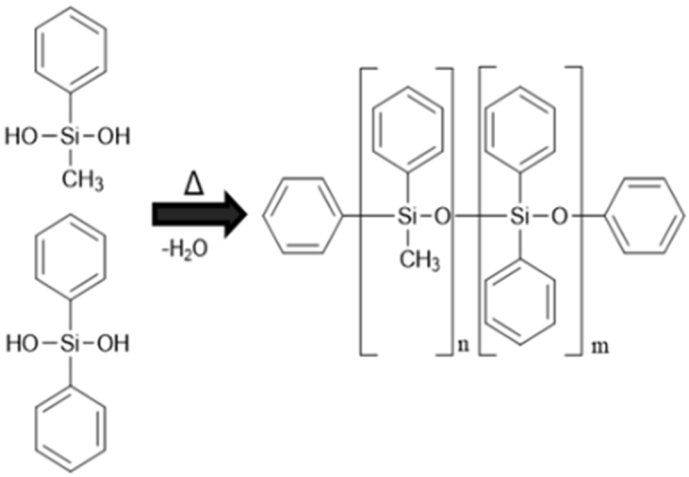

Figure 1. Synthesis methodology for phenyl silicone elastomers.

Initial efforts focused on both monomer and catalyst exploration. In FY23, it was determined that a volatile tin catalyst (removed during curing) and silanol-based monomers were ideal precursors. Further efforts focused on the heating and vacuum removal of byproducts. A stepped curing process under as high a vacuum as possible was required to achieve low-defect membranes. Future work will explore the incorporation of a variety of radiation-stable carbonaceous fillers.

Since direct tritium contact is far too expensive, tritium degradation is simulated by exposure to high levels of gamma radiation in a deuterium environment (to monitor isotope exchange). Exposure in deuterium gas is accomplished in small, stainless-steel cylinders.

The hydrogen permeability of the silicone elastomer is crucial to its intended function. The permeability of hydrogen, nitrogen, and argon in these materials is measured in a custom-built permeation manifold. The permeability and thermomechanical properties of the elastomers are tested before and after radiation exposure.

Accomplishments

- Determined novel methodology to produce phenyl silicone elastomers with no C-C sp^3 crosslinks. Applied this methodology to a variety of permutations, demonstrating tunability of the process.
- These phenyl silicone elastomers experienced no change in thermomechanical or chemical properties after 1 MGy exposure, equivalent or better than the most gamma radiation-stable unfilled elastomers ever reported.
- Confirmed the high gas barrier of the phenyl silicone elastomers in comparison to traditional silicone elastomers.

Intellectual Property

- US Patent Application 63/500,743

Team Members

Lauren Hanna, Chris Verst, George Larsen, Dale Hitchcock, Anastasia Mullins, Gavin Mattingly

Enhancing Charge Injection in Polyoxometalate-based Dye-Sensitized Solar Cells

Lauren Hanna

A selected 3d-transition metal-containing polyoxometalate and corresponding parent polyoxometalate were synthesized. These materials were successfully characterized using a variety of spectroscopic and electrochemical techniques. The polyoxometalates were sensitized with a porphyrin-based dye to permit for photoinduced charge transfer for solar energy applications.

Introduction

Solar energy technology, such as dye-sensitized solar cells, relies on light harvesting materials that optimize use of the solar spectrum for green energy applications. The overall efficiency of a photovoltaic cell is heavily dependent on the electron injection efficiency from the photosensitizer to the semiconductor[1]. Charge injection to the semiconductor is often limited by the intrinsic lifetime of the photoinduced, charge separated state of the sensitizer, which results in electron-hole recombination[1]. To address this issue, a class of materials known as polyoxometalates have been investigated as potential photoanode materials. Polyoxometalates (POMs) are a class of molecular metal oxide analogues that are composed of high valent transition metals (such as Mo, W, or V). Due to their chemical makeup, they are excellent electron acceptors and exhibit reversible redox activity[2, 3]. To efficiently tune the electronic structure of the POM, low valent 3d-transition metals can be integrated into the framework.

Recent studies have concluded that covalent linkages between the photosensitizer and polyoxometalate may generate hybrid products with unique charge transfer properties[4-6]. Despite these efforts, no fundamental, systematic study has been conducted that investigates how the nature of the polyoxometalate affects the efficacy of charge transfer when covalently bound to a photosensitizer.

To understand the charge transfer dynamics of the hybrid material, our investigation designed a 3d-transition metal containing polyoxometalate covalently bound to a porphyrin photosensitizer (4Fe-POM-Zn-CTPP). The results of this study were compared to the analogous homogenous parent Wells-Dawson polyoxometalate,

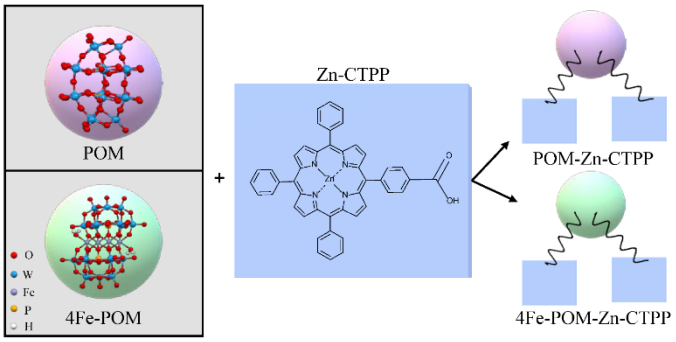

Figure 1. Depiction of the polyoxometalates (POM and 4Fe-POM), porphyrin (Zn-CTPP), and hybrid species (POM-Zn-CTPP and 4Fe-POM-Zn-CTPP) in this study

POM, and the corresponding hybrid material, POM-Zn-CTPP (**Figure 1**).

Approach

The purpose of this project is to understand how incorporation of a heterometal into a polyoxometalate can affect photo-induced charge transfer from a photosensitizer to the POM. The approach of the project is to, first, synthesize an iron-containing polyoxometalate, as well as the parent polyoxometalate containing no heterometal (iron). These POMs are then characterized using a series of spectroscopic and electrochemical techniques to confirm the identity and stoichiometry. Second, the POMs were covalently bound to a porphyrin photosensitizer, zinc (II) monocarboxyphenyl triphenyl porphyrin. These hybrid materials were deposited as thin films on conducting substrates to generate photoanodes. The efficiency of charge transfer from porphyrin photosensitizer to polyoxometalate was evaluated for both materials through spectroscopic and electrochemical means to understand the effect of the heterometal. Fluorescence spectroscopy evaluated each POM-porphyrin hybrid material to determine whether

fluorescence quenching occurred. Quenching of the porphyrin fluorescence was a clear indication of successful charge transfer. Transient photocurrent measurements evaluated the current produced by materials when illuminated by white light; a key quality for successful dye-sensitized photoanode materials. Other electrochemical measurements, such as open circuit voltage and I-V curves, revealed the efficiency of the polyoxometalate-porphyrin material under visible light irradiation.

From these measurements, it was determined that the incorporation of the iron heterometal resulted in efficient charge transfer from the porphyrin moiety to polyoxometalate.

Accomplishments

- Synthesized a series of transition metal substituted polyoxometalates (where TM=Mn, Fe, Cu, Co)
- Synthesized Zn-containing porphyrin photosensitizer
- Successfully covalently bound porphyrin-based photosensitizer to various transition metal substituted polyoxometalates to generate hybrid materials
- Characterized all species, including hybrid materials, using a variety of electrochemical and spectroscopic techniques, including electron dispersive X-ray spectroscopy, Fourier transform infrared spectroscopy (**Figure 2**), UV/Vis spectroscopy (**Figure 3**), and cyclic voltammetry (**Figure 4**)
- Conducted fluorescence measurements on hybrid materials and individual species to efficient photoinduced charge transfer from porphyrin to iron-based polyoxometalate (**Figure 5**)
- Deposited films of hybrid polyoxometalate-porphyrin materials on conductive substrates to generate photoelectrodes
- Carried out photoelectrochemical measurements under dark and illuminated conditions to reveal the production of photocurrent (**Figure 6-7**)
- Submitted manuscript to Dalton Transactions, currently undergoing review
- Abstract was submitted and accepted for a talk at SERMACS conference

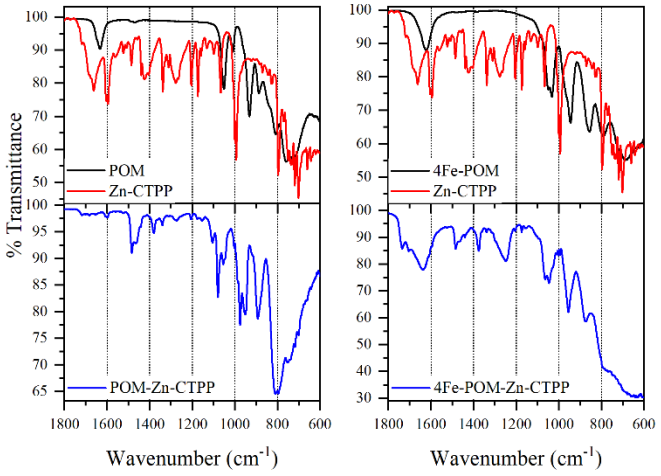

Figure 2. FT-IR spectra of left: POM (black), Zn-CTPP (red), and POM-Zn-CTPP (blue) and right: 4Fe-POM (black), Zn-CTPP (red), and 4Fe-POM-Zn-CTPP (blue)

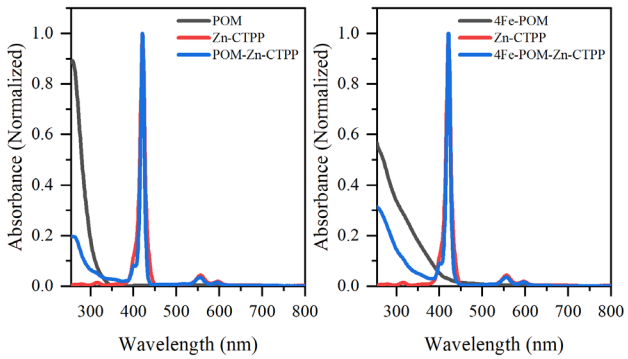

Figure 3. UV/Vis spectra of left: POM (black), Zn-CTPP (red), and POM-Zn-CTPP (blue) and right: 4Fe-POM (black), Zn-CTPP (red), and 4Fe-POM-Zn-CTPP (blue) measured in acetonitrile

Peer-reviewed Publications

- Hanna, L. K. M. Investigation of Heterometal Substitution in Polyoxometalate-Porphyrin Hybrid Materials for Efficient Charge Transfer *Dalton Transactions* **2023**. ***(undergoing peer review)***

Team Member

Kori McDonald

References

(1) Katoh, R.; Furube, A. Electron injection efficiency in dye-sensitized solar cells. *Journal of Photochemistry and Photobiology C: Photochemistry Reviews* **2014**, *20*, 1-16. DOI: https://doi.org/10.1016/j.jphotochemrev.2014.02.001.

(2) Wang, Y.; Fu, X.; Wang, T.; Li, F.; Li, D.; Yang, Y.; Dong, X. Polyoxometalate electron acceptor incorporated improved properties of Cu2ZnSnS4-based room temperature NO2 gas sensor. *Sensors and Actuators B:*

Chemical **2021**, *348*, 130683. DOI: https://doi.org/10.1016/j.snb.2021.130683.
(3) Sun, X.; Lan, Q.; Geng, J.; Yu, M.; Li, Y.; Li, X.; Chen, L. Polyoxometalate as electron acceptor in dye/TiO2 films to accelerate room-temperature NO2 gas sensing. *Sensors and Actuators B: Chemical* **2023**, *374*, 132795. DOI: https://doi.org/10.1016/j.snb.2022.132795.
(4) Winter, A.; Endres, P.; Schröter, E.; Jäger, M.; Görls, H.; Neumann, C.; Turchanin, A.; Schubert, U. S. Towards Covalent Photosensitizer-Polyoxometalate Dyads-Bipyridyl-Functionalized Polyoxometalates and Their Transition Metal Complexes. *Molecules* **2019**, *24* (24), 4446.
(5) Ma, P.; Hu, F.; Wang, J.; Niu, J. Carboxylate covalently modified polyoxometalates: From synthesis, structural diversity to applications. *Coordination Chemistry Reviews* **2019**, *378*, 281-309. DOI: https://doi.org/10.1016/j.ccr.2018.02.010.
(6) Zhu, Y.; Huang, Y.; Li, Q.; Zang, D.; Gu, J.; Tang, Y.; Wei, Y. Polyoxometalate-Based Photoactive Hybrid: Uncover the First Crystal Structure of Covalently Linked Hexavanadate-Porphyrin Molecule. *Inorganic Chemistry* **2020**, *59* (4), 2575-2583. DOI: 10.1021/acs.inorgchem.9b03540.

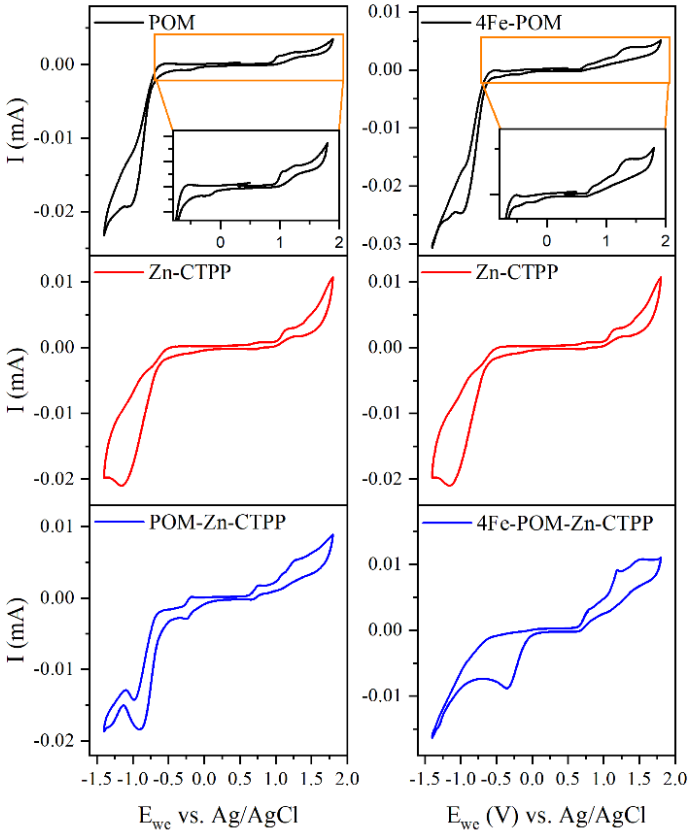

Figure 4. Cyclic Voltammograms of Left: POM (black), Zn-CTPP (red), and POM-Zn-CTPP (blue) and Right: 4Fe-POM (black), Zn-CTPP (red), and 4Fe-POM-Zn-CTPP (blue)

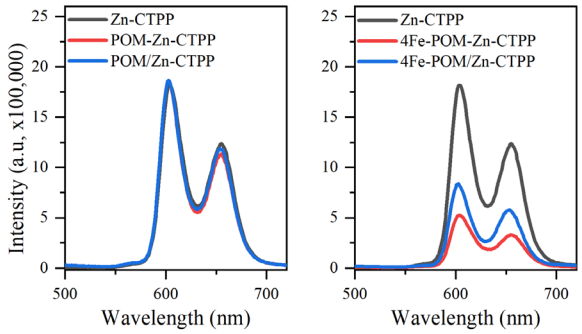

Figure *5.* Fluorescence spectra upon 371 nm excitation of right: Zn-CTPP (black), POM-Zn-CTPP (red), and POM/Zn-CTPP (blue) and left: Zn-CTPP (black), 4Fe-POM-Zn-CTPP (red), and 4Fe-POM/Zn-CTPP (blue)

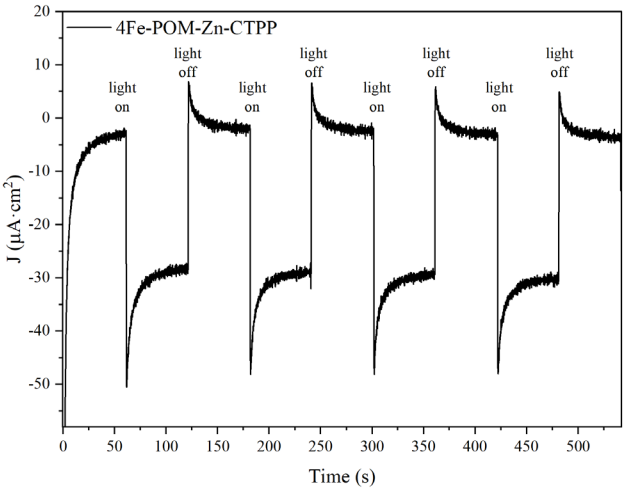

Figure 6. Photoelectrochemical response of 4Fe-POM-Zn-CTPP with a +0.1 V bias upon irradiation (≥ 360 nm)

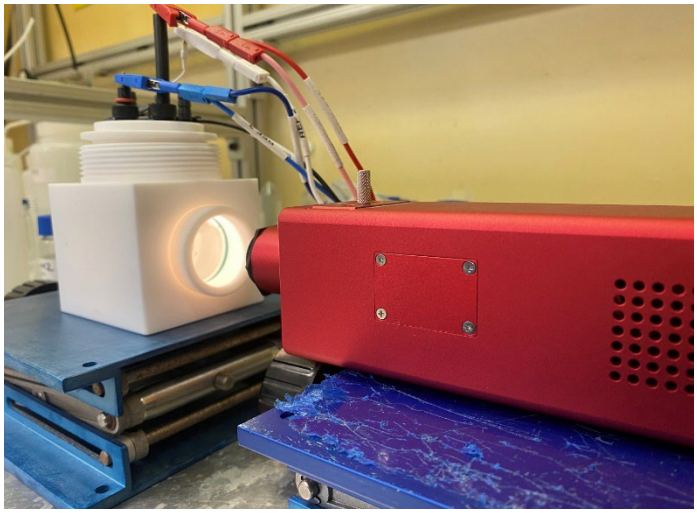

Figure 6. Photocurrent measurement set up with test vessel with optical window and white light source

Topological Magnetic Textures in Lanthanide- and Actinide-based Quantum Materials

Binod Kumar Rai

Materials that are governed by quantum behavior display emergent phenomena, such as exotic magnetism and topological states of matter, and are potentially suitable for future energy storage. Engineering these new quantum materials while understanding their fundamental properties is essential to successfully utilizing these materials in future technologies.

Introduction

The design and development of new materials has often played a key role in discovering new physical phenomena and advancing technology. Quantum materials exhibiting exotic magnetism and topological states of matter are potentially suitable for future energy storage. Alongside the possibility of utilizing these materials in future technologies, the emergent phenomena associated with quantum materials has motivated scientists worldwide. However, the realization of exotic magnetism and topological states of matter as well as the understanding of the fundamental mechanisms of such systems are limited to only a few materials. The f-electron-based compounds are a promising class of materials, where RKKY interactions and spin-orbit coupling favor stabilizing such exotic magnetism and topological states of matter.

This materials-driven research program identified and synthesized several quantum materials that have the potential to exhibit exotic magnetism. The synthesized quantum materials were investigated to study the relationship between structural, magnetic, and electronic properties by establishing collaboration with universities, national labs, and DOE User facilities. Our study focused on the fundamental science of quantum materials and found complex magnetic structures in these materials. The revelation of novel quantum phases in new classes of materials is fundamental yet extremely crucial scientific information needed for advancing our understanding of and establishing a path from the discovery of topological materials to a final product.

Approach

The design and development of new materials for this project requires the liquid flux crystal growth lab for intermetallic- and oxide-based materials. The crystal growth lab was established at SRNL by completing safety work control documents in FY22. We have synthesized several materials such as PuCl3.6H2O, NdCuGa3, EuIr3Si7, and Ir3(Si,Ga)7 at SRNL. The newly established single crystal XRD is crucial for discovery of new crystals such as EuIr3Si7 and Ir3(Si,Ga)7.

The physical properties of magnetic materials are essential to achieving the project's proposed objectives; however, SRNL didn’t have the Dynacool PPMS capability. Thus, materials' magnetic and thermodynamic properties were measured at collaborators’ institutes INL, LANL, and ORNL. To investigate the magnetic structure of materials, neutron beamtime proposals were submitted through a general Users proposal call at ORNL (DOE User Facility). Six neutron beamtime proposals were awarded and neutron scattering experiments were successfully completed in FY22 and FY23. One of the beamtime proposals examined the magnetic properties of NpO2 at cryogenic temperature. One of the neutron beamtime proposals awarded in FY23 is expected to be scheduled for measurements in February/March 2024. One of the proposals is to study complex magnetic structures in actinide-based chloride materials. Our study focusing on the fundamental science of quantum materials has found interesting crystal structure details and complex magnetic structure in these materials.

Accomplishments

We have published three peer-reviewed articles, two manuscripts are under review and two manuscript drafts are in preparation. We presented five contributed talks, and our team was encouraged to apply to three DOE full proposals in FY22 and FY23. The details are provided below:

- Submitted three full DOE SC proposals in FY22 and FY23 and one DOE SC proposal funded in FY 23.
- Invited to write a review article in the Report on Progress in Physics (Impact factor: ~18), the manuscript is under review [see the journal detail in the peer-reviewed publications section].
- The review article overview presents the status of crystal growth, crystal structure and magnetism of actinide oxides candidate materials and provides key insights on continuously developing the fundamental understanding of these magnetic candidate materials.
- We synthesized several clean and rad materials such as NpO2, PuCl3.6H2O, NdCuGa3, EuIr3Si7, and Ir3(Si,Ga)7 at SRNL for the magnetic and physical property measurements of synthesized materials.
- We ran neutron diffraction experiments on NpO2 and hydrated PuCl3. NpO2 results are published in collaboration with ORNL [see the journal detail in the peer-reviewed publications section].
- Invited to write an RTX3 topical review article from the Institute of Physics (IOP) publication and published in the Journal Physics: Condensed Matter in May 2022 [see the journal detail in the peer-reviewed publications section].
- The review article identifies several candidate materials that have potential to exhibit exotic magnetism and topological states of matter.
- The review article was featured as a publication spotlight at SRNL in June 2022.
- Delivered five contributed scientific talks at the American Physical Society and Materials Research Society in FY22 and FY23. NdCuGa3 EuIr3Si7 and Ir3(Si,Ga)7 results were presented at the conferences.
- Presented a poster at the Advanced Manufacturing Center (AMC) collaboration workshop in June 2022.
- Awarded six proposals for neutron beamtime at ORNL in FY22 and FY23. The neutron beamtime was requested using a general user proposal call. Powder and single crystal neutron diffractions were completed at ORNL in $NdCuGa_3$ and NpO_2 materials.
- Established a crystal growth lab for intermetallic- and oxide-based materials for the first time at SRNL.
- Synthesized several candidate materials such as NdCuGa3 Ir9Al28, Ir3(Ga,Si)7 and EuIr3Si7. In addition, single crystal x-ray diffraction data were collected for synthesized materials at SRNL. For example, the crystal structure solution and magnetic measurements under magnetic field results of NdCuGa3 and EuIr3Si7 are presented in **Figures 1, 2 and 3**.
- Arc-melter (a new capability at SRNL to alloy metallic materials) is operational since FY23 by completing a hazard analysis and USQ. The arc-melter was procured in FY22. The new capability will extend SRNL's materials growth and processing strength.

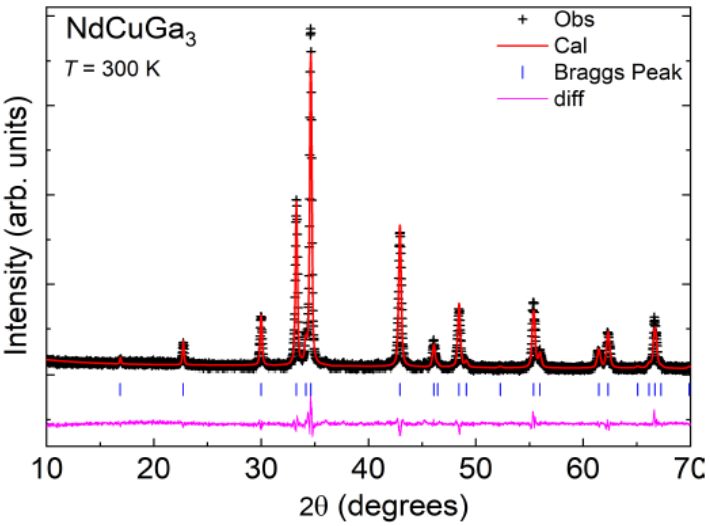

Figure 1. Room-temperature powder diffraction pattern of NdCuGa3 together with the Rietveld refinement (red line) and Bragg positions (vertical lines).

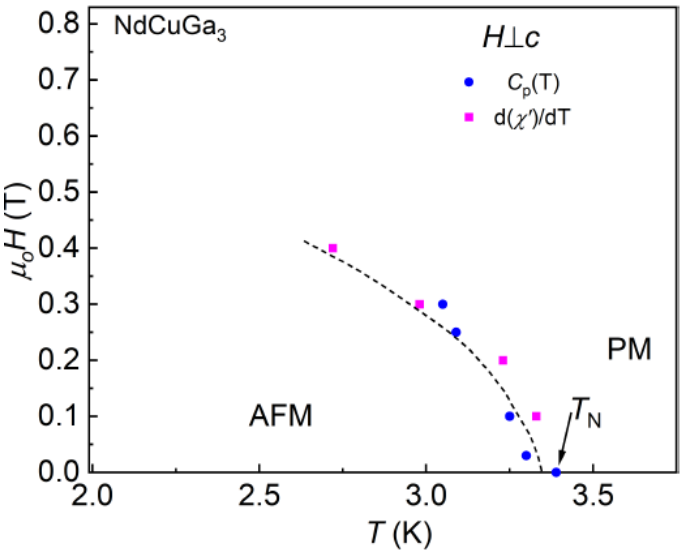

Figure 2. The H vs. T magnetic phase diagram of NdCuGa3 is constructed with transition determined from specific and ac susceptibility data.

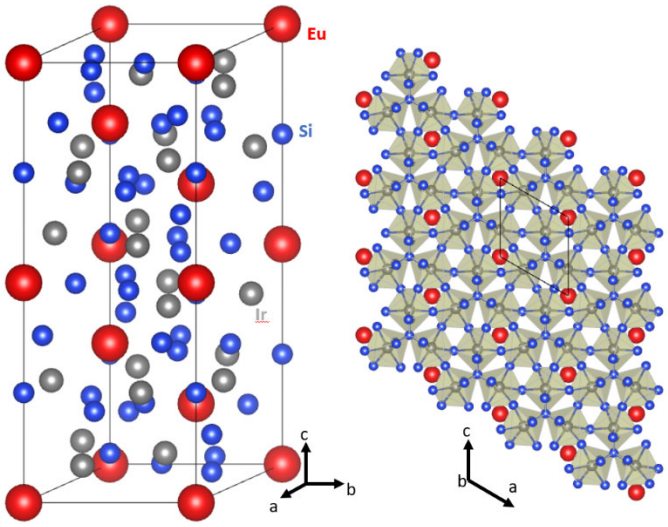

Figure 3. Single crystals of $EuIr_3Si_7$ were discovered at SRNL and single crystal XRD data were characterized and analyzed using a newly installed SCXRD instrument at SRNL. Left: $EuIr_3Si_7$ atoms in a unit cell for the solved crystal structure. Right: atoms viewing along b-axis.

Peer-reviewed Publications

- Binod K. Rai, Alex Bretana, Gregory Morrison, Volodymyr B. Buturlim, Hanno zur Loye, Krzysztof Gofryk "Physical properties of $Ir_3(Ga,Si)_7$ single crystals. (manuscript in preparation *2023)*.
- Binod K. Rai, Alex Bretana, Gregory Morrison, Ryan Greer, Krzysztof Gofryk, Hanno zur Loye, "Magnetism of Binary Actinide Oxides: A Review", Report on Progress on Physics (Invited Review Article, *Under Review 2023)*.
- Binod K. Rai, Patrick O'Rourke, Catherine Housley, Henry Ajo, Arjun Pathak, Narayan Poudel, Krzysztof Gofryk, Boris Maiorov, Qiang Zhang, Travis Williams, and Matthias Frontzek, "Magnetic properties of $NdCuGa_3$ single crystals", *(Under Review 2023)*.
- Matthias D. Frontzek, Luke R. Sadergaski, Samantha K. Cary, Binod K. Rai, "Search for octupolar ordering in NpO_2 by unpolarized neutron powder diffraction", *J. Solid State Chemistry* 321 **2023**, *321,* 123875
- Binod K. Rai, Patrick O'Rourke, Utpal Roy, "Review on crystal structures and magnetic properties of RTX3 materials", J. Physics: Cond. Matter. 2022, 34, 273002 (Invited Topical Review Article, SRNL publication spotlight)
- Binod K. Rai, Shang Gao, Matthias Frontzek, Yaohua Liu, A. D. Christianson, A. F. May, "Magnetic properties of Fe-substituted $NiBr_2$ single crystals", *J. Magn. & Magn. Mater.*, **2022** 557 169452.

Team Members

Alex Bretana[**], Ryan Greer[*] Tucker Koenig[+], Catherine Housley, Henry Ajo, Boris Maiorov[c], Krzysztof Gofryk[b], Gregory Morrison, and Hanno Zur Loye[a]

[a] *University of South Carolina*
[b]*Idaho National Laboratory*
[c]*Los Alamos National Laboratory*
[*]*Postdoctoral Researcher*
[**]*Laboratory Director's Postdoctoral Research Fellow*
[+]*Undergraduate Intern*

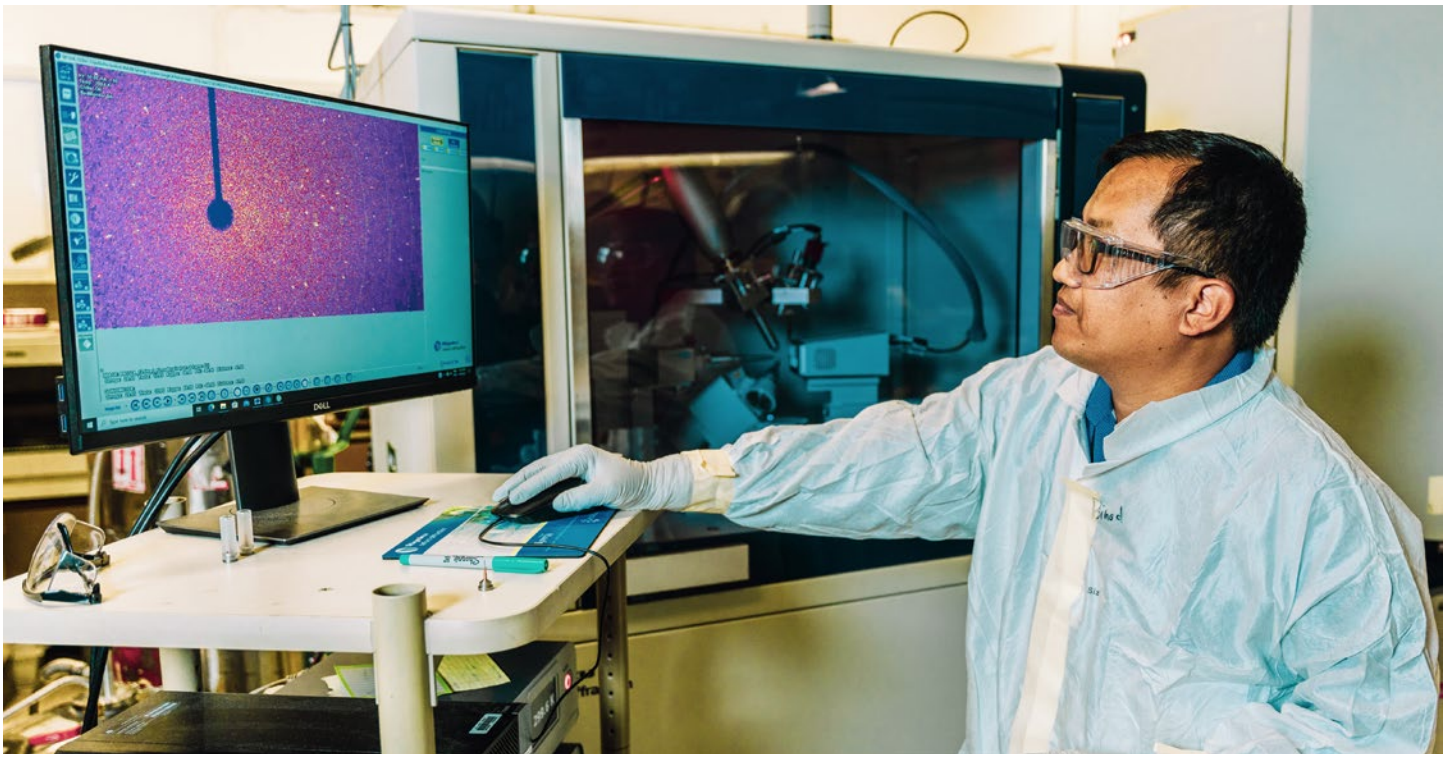

Defining Qubit Properties in Pa^{4+} Complexes

Lindsay Roy

This research seeks to develop a detailed understanding of the chemical and electronic properties of protactinium (Pa) complexes in the hopes of controlling its spin-orbit and crystal electric field effects with potential as an actinide qubit. SRNL has a unique opportunity to not only describe the interplay between the d and f orbital occupations, but also make significant contributions to the community using recently found Pa material.

Introduction

Quantum materials are at the forefront of scientific discovery because their exotic electronic properties will enable new applications not realized before in areas of computing, information, sensing, and other related applications. The f-elements have shown exceptional promise as new quantum materials, particularly as relativistic effects to enable phenomena such as quantum wells and quantum tunneling. The energetics of the actinide series is interesting because the 5f and 6d orbitals change across the periodic table, enabling a rich and complex chemistry wherein control of quantum bit (qubit) could be possible. Protactinium is of particular interest because of near degeneracy of the 6d/5f orbitals, making it behave more like a transition metal. This work delineates the chemically engineering of high-valent $5f^1$ protactinium complexes as qubits by evaluating how its unique atomic properties, including spin-orbit coupling (SOC), crystal electric field (CEF), and nuclear spin, can be exploited through coordination chemistry to observe long-lived coherence times. The research leverages both experimental and theoretical findings to generate a set of features to enhance quantum coherences in actinide molecules.

Approach

Our approach is broken down into two overarching objectives: purification, synthesis, and characterization of Pa^{4+} complexes and development of first-principles derivation of spin-orbit coupling and crystal electric field parameters for Pa^{4+}.

Purification, Synthesis and Characterization:

1. Identify: using radiolysis the legacy sample can be analyzed by its unique radiological signature. This is used to not only understand the bulk element but also its decay daughters/granddaughters.
2. Purify: develop a method to extract the materials from the source.
    1. Dissolution: finding a suitable acid/solvent to isolate the sample from the source
    2. Separation: multiple elements and unwanted products could be removed from the source requiring a separation using solvent, precipitation, or exchange resins.
3. Synthesis and Characterization.
4. Documentation/Storage.

Exploration of the Pa-Ligand chemical space:

1. Exploration: develop ab initio methods to evaluate the metal-ligand chemical space for Pa^{4+} systems. Test Systems: evaluating Walsh Diagrams for MCl_4, MCl_6^{x-} and MCl_3 (M = Th, Pa, U, Np) .
2. Spin-Phonon Coupling: establish a methodology to quantify the intensity as well as mechanisms and processes for relaxation pathways in actinide qubit complexes.

Accomplishments

As mentioned earlier, project work was divided into four tasks to show progress in all areas, which are outlined below along with their milestones in FY23. Results and accomplishments are presented under each milestone.

Task 1: Purification of ~80 mg legacy protactinium (Pa) material

Milestone 1: Identified purification method of ^{231}Pa (August 2022)

The protactinium bearing sealed source (**Figure 1**) was isolated in a 250 mL Nalgene bottle in preparation for

Figure 1. Sample of lead contained Pa-231, legacy material at SRNL.

leaching/dissolution. Initially 10 mL of a 5 M HF solution was added to the vessel and allowed to digest for 10 minutes before isolating a brown solution through filtration. To this solution, a 5x stoichiometric amount of ammonium hydroxide was added to form an off white/tan precipitate expected to be $Pa(OH)_5$. This precipitate was then dissolved in 3 M sulfuric acid (H_2SO_4) due to the known stability of Pa in a sulfate solution. The solution was analyzed by gamma scan to have the most Pa-231 of any product solutions.

Task 2: Synthesis and characterization of Pa^{4+} complexes
Milestone 2: Determination of new Pa^{4+} complexes (ongoing through August 2023)

Proposed scheme for isolation of a protactinium product has been devised. The proposed synthesis will proceed through a hydrothermal based synthesis using a PARR autoclave with a 10 mL Teflon liner. One milliliter of the Pa solution was reacted with 30x molar excess of boric acid following the general reaction reported by Wang et.al. The autoclave was sealed and heated to 200 °C in a box furnace for 7 days after which, the furnace was turned off to cool naturally to room temperature overnight. A white solid was observed and collected on opening the reaction vessel (**Figure 2**). Under a microscope, a fan shaped agglomerate of colorless crystals were observed. A piece of this agglomerate was selected and mounted on a glass fiber for analysis by single crystal X-ray diffraction. Initial unit cell parameters indicate a monoclinic structure containing Pa as shown in **Table 1** below. Proposed crystal structure is in (**Figure 3**).

Task 3: Exploration of the Pa-Ligand chemical space
Milestone 3: Validation of theoretical methods via experiment of Pa^{4+} known complexes (August 2022)

Calculations were performed on MCl_3^+, MCl_4, and MCl_6^{2-} (M = Th-Np) to evaluate the amount of d/f orbital character when breaking from high symmetry complexes. The results show that as you decrease the symmetry of the system, the overall energy remains flat until a higher degree of symmetry breaking occurs in turn leading to higher d orbital character in the highest occupied molecular orbital for the tetrachloride complexes (**Figure 4-6**). There are several commercial-off-the-shelf ligands available to explore the extent of d-character mixing because of symmetry breaking.

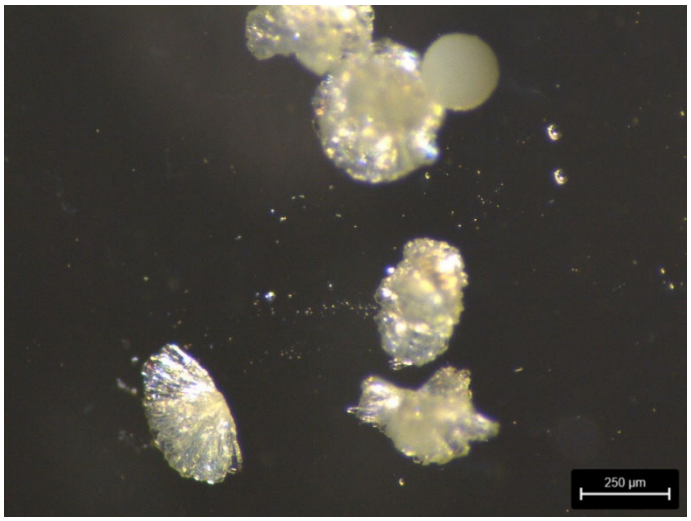

Figure 2. Crystalline material collected after hydrothermal based synthesis targeting a borate compound.

Table 1 Crystal parameters	
a	22.23 Å
b	6.66 Å
c	7.93 Å
α	90°
β	96.89°
γ	90°

Table 1.

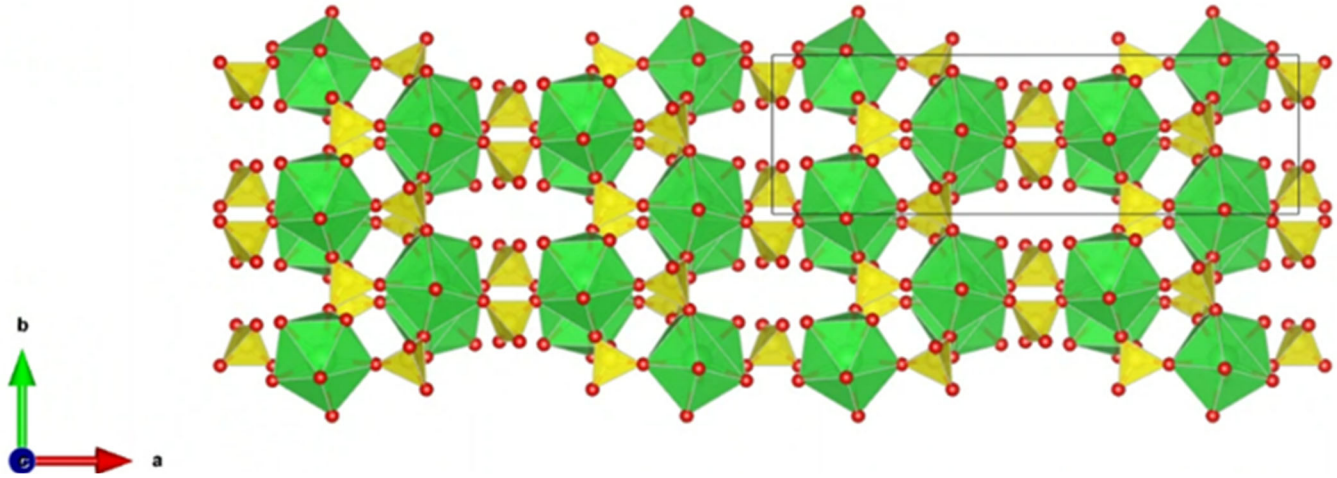

Figure 3. Crystal Structure of (PaO2)2(SO4)3 (Proposed stoichiometry).

Task 4: Spin-phonon coupling calculations

Milestone 4: Derivation of spin-phonon coupling in $5f^1$ single ion magnets (August 2023)

Spin-phonon coupling calculations started using the ORCA software in Q4 FY22. Initial calculations focus on computing the magnetic properties of the early actinide chlorides and metallocene complexes (**Figure 7**).

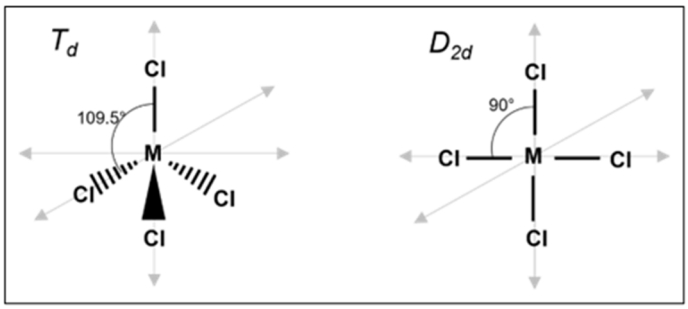

Figure 4. Tetrachloride geometry from T_d tetrahedral to D_{2d} square planar, where the angle change for the 'top' Cl ligand is 70.5 degrees. Intermediate calculations performed at 7.05-degree increments.

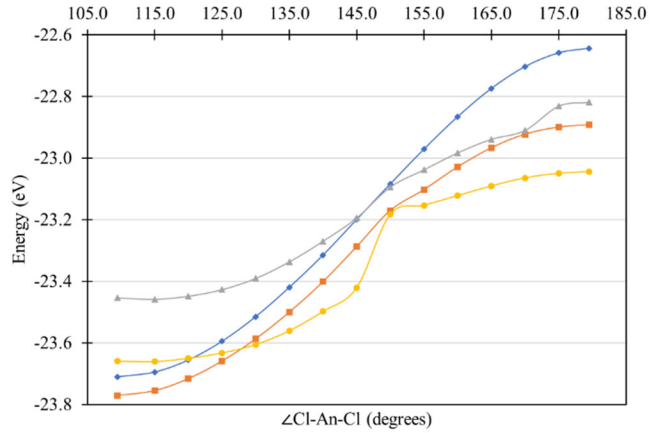

Figure 5. For the tetrachloride complexes, the bond energies for each incremental ∠Cl-An-Cl angle is plotted. The data for each series corresponds to Th: blue, Pa: orange, U: gray, and Np: yellow.

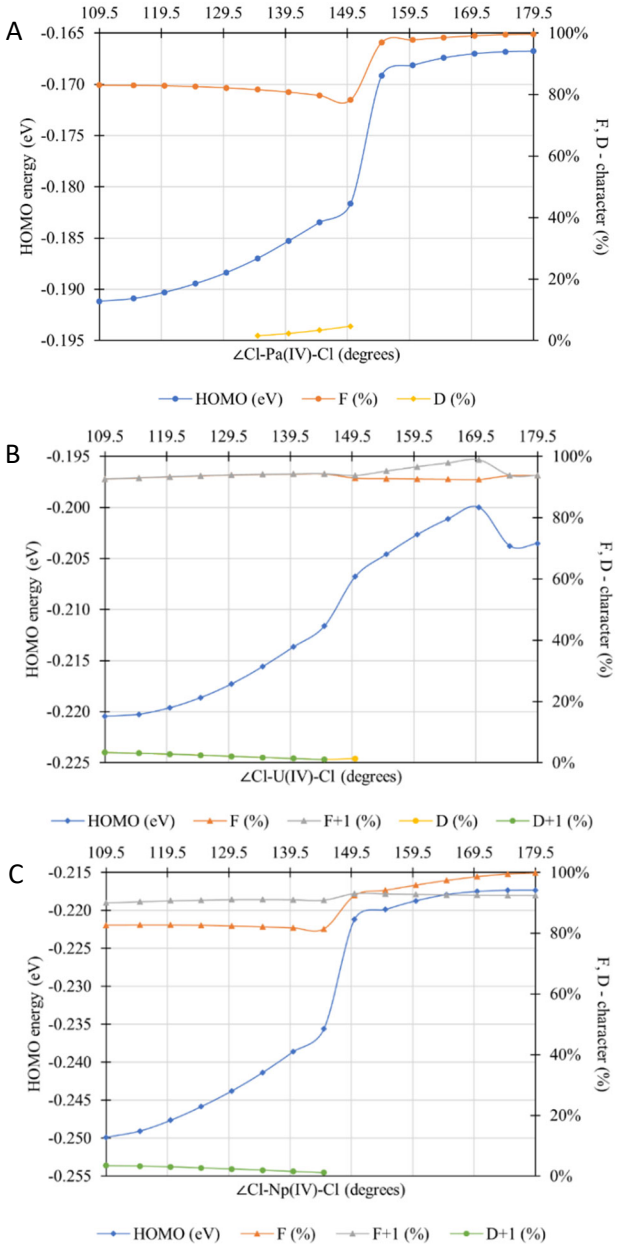

Figure 6. The HOMO energy (eV) for (A) Pa, (B) U, and (C) Np tetrachloride complexes with their respective f and d molecular orbital populations (as percentages) are plotted for each incremental step. Gaps within the d-series imply there is 0.00% d-population. As the Cl-An-Cl angle increases the symmetry changes from tetrahedral to square planar.

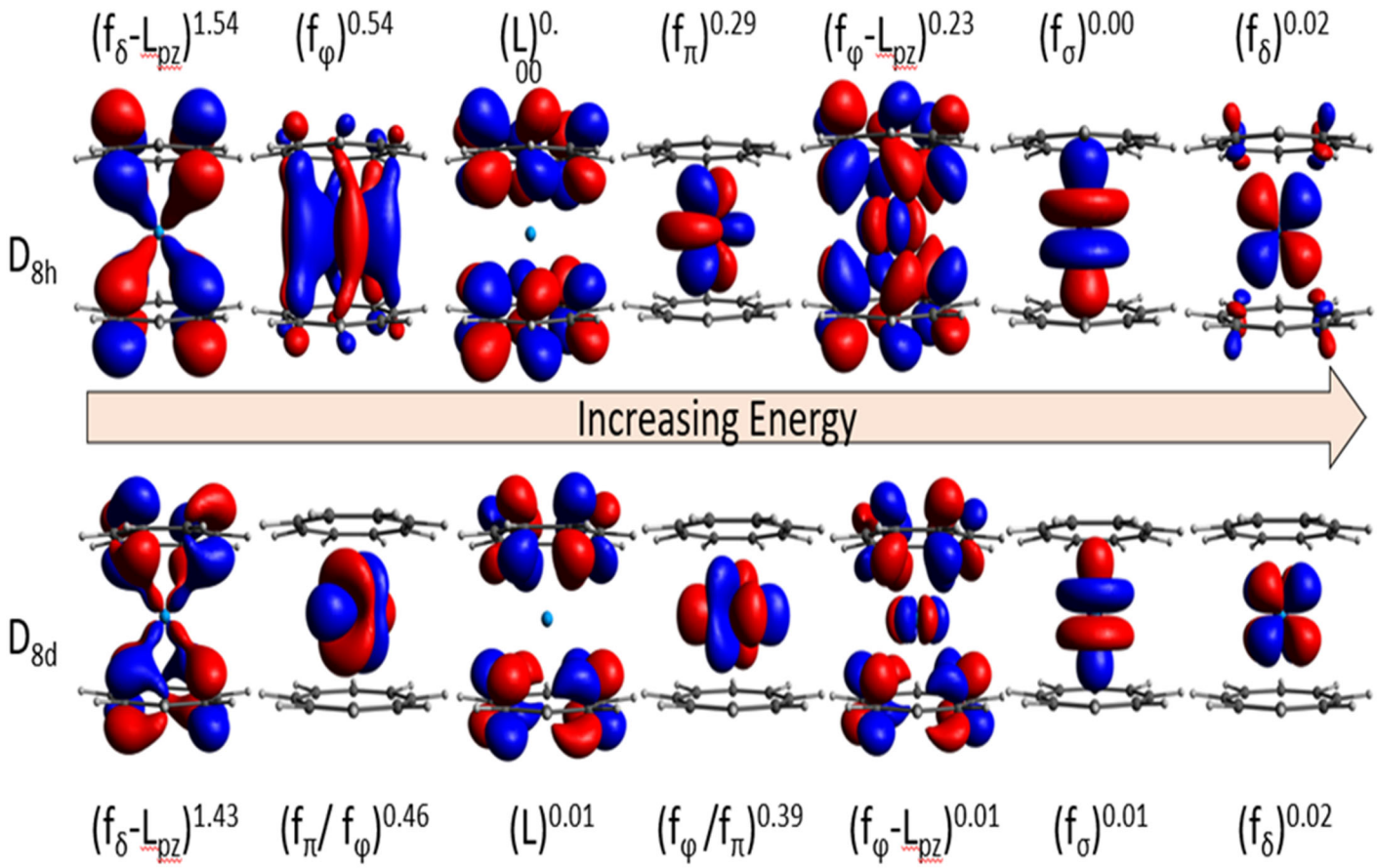

Figure 7. CAS(5,13) computed natural orbitals and their occupation numbers of some of the orbitals in the active space for the $Pa(COT)_2$ molecules is shown.

Team Members

Stephanie Gamble, Garret Gotthelf*, Megan Hoover*, Vinh Nguyen*, Julie Niklas[a]*, Henry La Pierre[a]

[a] *Georgia Institute of Technology*
**Postdoctoral Researcher*

FY23 PROJECTS

CORE COMPETENCY:

Sensing, characterizing, and assessing materials production and environmental impacts

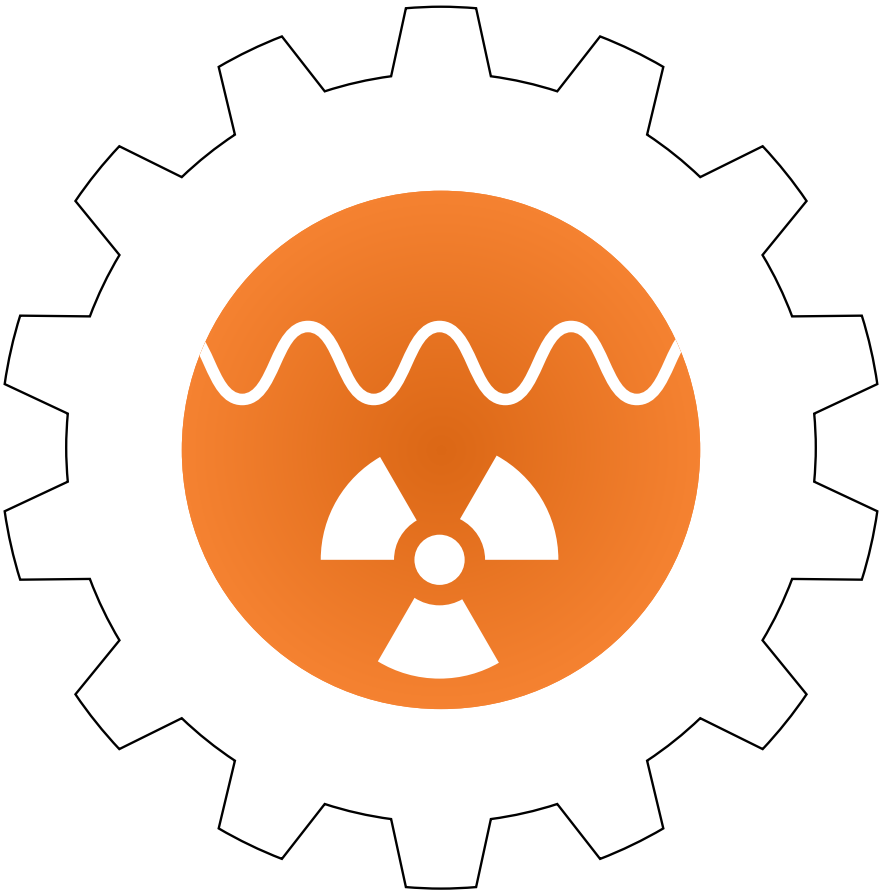

Multivariate Optimization for Sampling Instrumentation

Stephanie Gamble

This work introduces an approach for multivariate, multi-objective optimization with Karush-Kuhn-Tucker conditions to optimize method conditions of an instrument. It also proposes to broaden the options for the quantities to be optimized. An example case has been conducted for optimization of gas chromatography – mass spectrometry sample analysis.

Introduction

In fields involving sampling, optimization of instrument parameters is a common practice as the data output (such as peak shape in gas chromatography – mass spectrometry (GC-MS)) from samples is highly dependent on the instrument's method parameters. There is a need to employ a generalized strategy, suitable for almost any analytical instrumentation/sample preparation/analysis scheme. Trial-and-error is the typical current method optimization technique, which is time consuming and inaccurate when dealing with multiple parameters. The solution to this is multivariate Lagrangian optimization. In addition, a novel concept is proposed to broaden the options for the quantities to be optimized, for example, simultaneously optimizing height and width, rather than only peak area. Multi-objective optimization with Karush-Kuhn-Tucker conditions limits the optimization space to real-world or realistic solutions that are bounded by physical limitations of the instrument or process. These optimization methods are relevant to analytical systems/samplers/sample preparation methods used by government agencies, nuclear nonproliferation offices, and food industries. The resulting procedure will reduce time invested in optimizing analytical methods compared to traditional univariate trial-and-error optimization and potentially improve the sensitivity of current techniques. This methodology could reduce the cost of developing and optimizing future systems and instruments.

Approach

Modern, accurate optimization theory applied to the context of method optimization led to the development of a technique for optimizing the method parameters for a sampler or analytical instrument, such as a GC-MS analysis instrument (e.g., **Figure 1**). The techniques

Figure 1. A gas chromatography – mass spectrometry (GC-MS) instrument for analyzing air or liquid samples.

defined allow for the capability to simultaneously optimize multiple objective quantities [1], use of Lagrangian optimization as opposed to trial-and-error, inclusion of Karush-Kuhn-Tucker (KKT) conditions[2,3] to constrain the parameters based on physical limitations, and consider the Pareto Optimal front[4] to define optimality for a multi-objective problem. See **Figure 2** for the definition of the equation required to solve for the optimal parameter values (X^*).

To demonstrate the new optimization techniques, an example case was conducted for a GC-MS sample containing eleven iodinated alkane compounds with the goal of both maximizing the height of the intensity peaks and minimizing their width. A fractional factorial screening design[5] with analysis of variance[6] determined the parameters of significance to the objectives. Then, surface response experiments, conducted via a Box-Behnken experimental design[7], provided data to fit the objectives to a second order approximation to be

optimized. The equation shown in **Figure 2** was solved to find the optimal parameter values for the GC-MS method for that device to maximize peak heights and minimize widths. Data collected at approximately these optimal values are shown in **Figure 3**. The Pareto optimal front for the two objectives is shown in **Figure 4**.

$$\nabla \mathcal{L}(X^*) = \nabla[\alpha O(X^*) + \sum \mu_i g_i(X^*) + \sum \lambda_j h_j(X^*)] = \vec{\mathbf{0}}$$

where:

$\alpha = -1$ if minimizing, $= 1$ if maximizing
$g_i(X^*) \leq 0$, for all i
$h_j(X^*) = 0$, for all j
$\mu_i \geq 0$, for all i
$\mu_i^t g_i(X^*) = 0$, for all i
$\lambda_j \in \mathbb{R}$, for all j

Figure 2. Lagrangian equation with KKT conditions. $O(X)$ denotes the overall objective function (weighted linear combinator of individual objectives to be simultaneously optimized). g_i functions denote inequality constraints, where the physical range limitations for each parameter are included in the optimization. h_j functions denote any additional equality constraints that may relate the parameters.

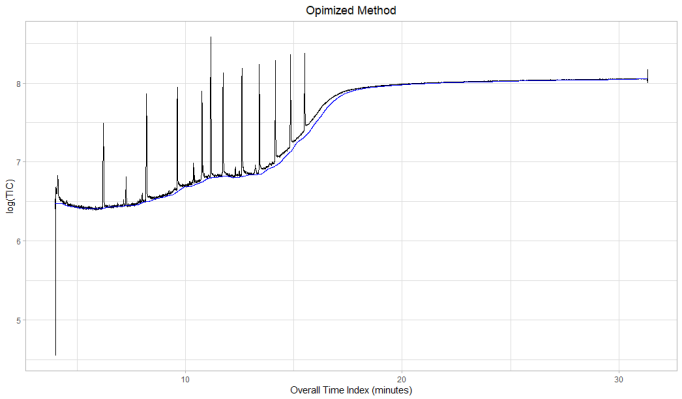

Figure 3. Data collected of the 11 iodinated alkanes at approximately the solved optimal parameters, given by the black line. The calculated baseline for the data is given by the blue line. With the optimal parameters, the measured average height was 1.52 x 10^8, and average width was 7.80 x 10^{-3}.

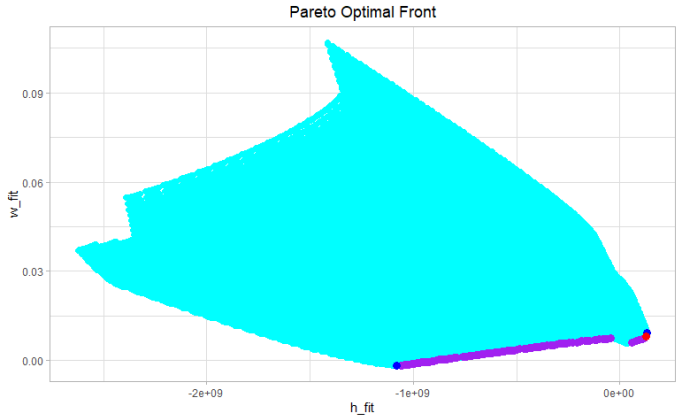

Figure 4: The Pareto optimal front of the fitted average peak height vs fitted average peak width in purple. The red point is the solved optimal point, based on weights chosen to normalize the two objectives, $O(X) = -\frac{1}{max(h)} O_h(X) + \frac{1}{max(w)} O_w(X)$. The space of admissible parameters is given in cyan.

Accomplishments

- A new technique for method optimization for sampling and analytical instruments was developed using modern and accurate optimization theory, improving results compared to a trial-and-error optimization technique. Improvement in objective values may be up to 2 orders of magnitude in the example of optimizing the peak height in GC-MS.
- The inclusion of experimental designs in this optimization technique saves researchers up to 2^(N-3) experiments to conduct, where N is the number of parameters. This would be approximately 30 minutes – 1 hour per experiment, saving researchers hours and providing further improvement over trial-and-error with no definite conclusion.
- The new technique improves accuracy of optimal values compared to using trial-and-error or unbounded optimization where the parameters are later restricted individually rather than incorporating physical constraints during the optimization.
- The expansion to new objective quantities allows for improved results based on the needs of individual projects this technique will be applied to.
- A journal article is being prepared for submission to *Science* (back up journal is *Analytical Chemistry*) which describes the full optimization technique and provides an example application.

Peer-reviewed Publications

- S. Gamble, C. Granger, & J. Mannion. Advanced Optimization for Sampling and Analysis Instrumentation. In preparation for submission to *Science*. 2023.

Team Members

Stephanie Gamble, Caroline Granger[*], Joseph Mannion Tatiyanna Singleton[+]

[*]*Postdoctoral Researcher*
[+]*Post-Bachelor's Intern*

References

1. K. Miettinen. Nonlinear Multiobjective Optimization. *Springer Science & Business Media*. 1998.
2. M. Abouhawwash & K. Deb. Karush-Kuhn-Tucker Proximity Measure for Multi-Objective Optimization Based on Numerical Gradients. Technical Report COIN Report No. 2016005. Department of Electrical and

Computer Engineering, Michigan State University, East Lansing, USA. 2016.
3. G. Giorgi, B. Jiménez, & V. Novo. Approximate Karush-Kuhn-Tucker Condition in Multiobjective Optimization. *J Optim Theory Appl*. **2016**. 171:70-89.
4. R. T. Marler, & J. S. Arora. Survey of multi-objective optimization methods for engineering. *Structural and Multidisciplinary Optimization*. **2004**. 26:6, 369–395.
5. D. C. Montgomery. Design and Analysis of Experiments (9th ed.) *John Wiley & Sons, Inc.* 2017.
6. R. A. Fisher. Statistical Methods for Research Workers (14th ed.) *Oliver & Boyd*. 1970.
7. G. Box & D. Behnken. Some new three level designs for the study of quantitative variables. *Technometrics*. **1960**. 2:455-475.

photo by Kelsie Taylor

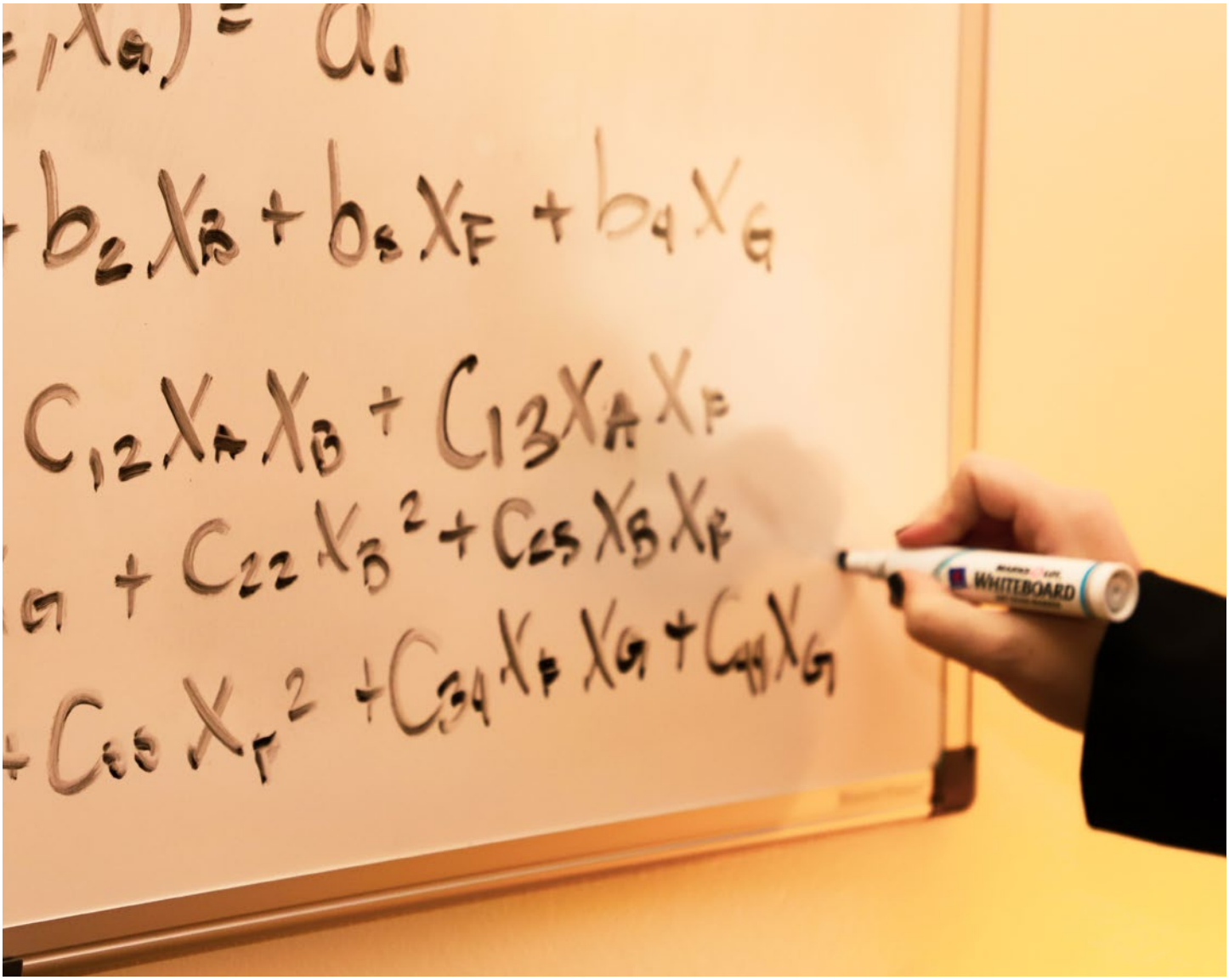

Development of Transuranic Stimuli-Responsive Metal-Organic Frameworks

Corey Martin, Dwight D. Eisenhower Postdoctoral Research Fellow

Photochromic metal-organic extended structures have the potential to shape the existing materials landscape of "smart" semiconducting materials. The inclusion of actinides within photochromic metal-organic frameworks will shed light on the unique photophysical and electronic properties of actinides in tandem with photochromic moieties.

Introduction

Understanding the electronic and photophysical properties of actinide-containing metal-organic frameworks (MOFs) is essential to determining their unrevealed potential, especially considering that there are very few literature reports on this subject to date.[1] This project merges the area of transuranic MOFs with the on-demand modularity of embedded photochromic units and includes the first studies delving into the area of photoresponsive MOFs where transuranic cations and stimuli-responsive building blocks are incorporated in the same structure.[2] An established correlation between the dynamic electronic and photophysical response under light exposure will be applied in advanced "smart" electronics such as MOF-based field effect transistors to highlight their functionality.

The first year of the project encompassed 1) the synthesis and structural characterization of five novel azobenzene-containing lanthanide-MOFs, 2) an investigation on the photochromic nature of 4,4'-azopyridine (4,4'-AzP) in the solid state, in solution, and loaded within a MOF's pores, and 3) procurement and method development of various spectroscopic instruments and components for time-resolved diffuse reflectance measurements under direct UV excitation. The second year of this project is focused on translating the studies of non-radioactive surrogates with their actinide counterparts (e.g., americium, curium, neptunium, and plutonium cations).

Approach

Photochromic molecules respond to light exposure, resulting in a reversible interconversion between photoisomers possessing distinct properties (e.g., dielectric constants, redox potentials, or absorption profiles). This research merges two research areas by combining the unique advantages of MOFs (e.g., porosity, modularity, and crystallinity) with the capability to tune the electronic and optical properties through integration of photoswitchable molecules. The ability to change the electronic energy levels of the valence and conduction bands in semiconductors is one of the foundational principles of modern electronics and their fine tuning (e.g., absolute conductivity, activation energy for charge transport, and intrinsic band gap) is crucial for performance optimization as active layer materials. As a choice of semiconductor material, MOFs are renowned for their modularity, owed to a nearly limitless combination of organic linkers and inorganic secondary-building units.

The project will be execute via the development of non-radiological MOF surrogates with embedded photochromic molecules (**Figure 1a**), monitoring electronic and photophysical properties using single-crystal and pressed-pellet conductivity (**Figure 1b**), and then by translating those initial findings into radiological systems and integrating them into a proof-of-concept device (**Figure 1c**). Five novel azobenzene-containing MOFs have been synthesized at SRNL and structurally characterized using single-crystal X-ray diffraction (**Figure 2**), Fourier-transform infrared spectroscopy, energy-dispersive X-ray (EDX) spectroscopy, and ^{1}H nuclear magnetic resonance spectroscopy on the digested species. The photophysical properties were investigated using time-resolved diffuse reflectance spectroscopy and show a change in optical response under UV excitation. Time-resolved conductivity measurements under UV-excitation are currently being developed.

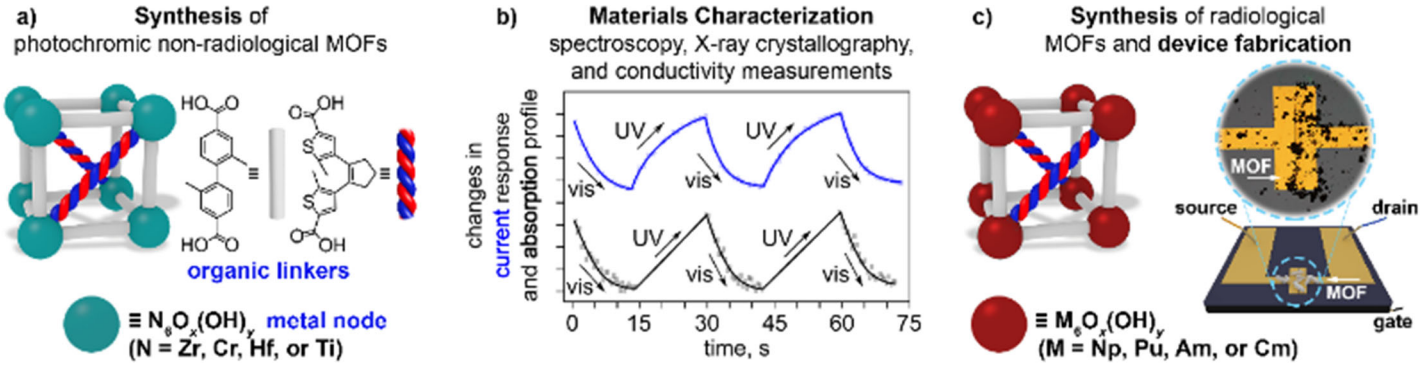

Figure 1. a) Examples of nonradiological photochromic MOFs (N = Zr, Ce, Hf, or Ti). b) MOF photophysical and electronic properties measured to establish a structure-property correlation. c) Radiological photochromic M-MOFs (M = Np, Pu, Am, or Cm), followed by investigating optoelectronic properties. Device fabrication is shown on the example of a field-effect transistor.

Accomplishments

- Synthesized five novel metal-organic frameworks ((Nd(4,4'-AzP), Pr(4,4'-AzP), Ce(4,4'-AzP), Eu(4,4'-AzP), and Dy(4,4'-AzP); 4,4'-Azp = 4,4'-azopyridine) including crystallographic structure solutions using single-crystal X-ray diffraction.
- Confirmed photochromic retention of azobenzene in photoswitch-embedded lanthanide frameworks. Measured in the solid-state, solution, and embedded in a MOF for photoisomerization rate comparison.
- Developed novel methods for time-resolved photophysics and electronics measurements using new diffuse reflectance spectrometer and electronic sourcemeter for high spatially and temporally controlled measurements on non-radioactive and radioactive materials.

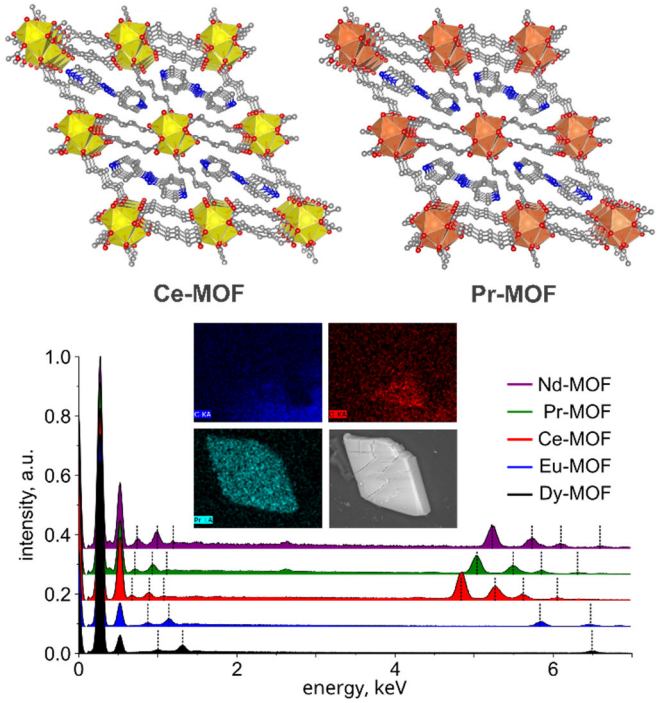

Figure 2. (*top*) Single-crystal X-ray diffraction structures of novel Ce(4,4'-AzP) and Pr(4,4'-AzP). The gray, red, blue, yellow, and peach colors represent carbon, oxygen, nitrogen, cerium, and praseodymium, respectively. (*bottom*) EDX spectra of Nd(4,4'-AzP) (purple), Pr(4,4'-AzP) (green), Ce(4,4'-AzP) (red), Eu(4,4'-AzP) (blue), and Dy(4,4'-AzP) (black). The inset shows EDX mapping for a single crystal of Pr(4,4'-AzP). The features corresponding to the presence of lanthanides are marked with dashed lines.

References

1. Martin, C. R.; Leith, G. A.; Shustova, N. B. Beyond Structural Motifs: The Frontier of Actinide-Containing Metal-Organic Frameworks *Chem. Sci.* **2021**, *12*, 7214–7230.

2. Martin, C. R.; Leith, G. A.; Kittikhunnatham, P.; Park, K. C.; Ejegbavwo, O. A.; Mathur, A.; Callahan, C. R.; Desmond, S. L.; Keener, M. R.; Ahmed, F.; Pandey, S.; Smith, M. D.; Phillpot, S. R.; Greytak, A. B.; Shustova, N. B. Heterometallic Actinide-Containing Photoresponsive Metal-Organic Frameworks: Dynamic and Static Tuning of Electronic Properties *Angew. Chem. Int. Ed.* **2021**, *60*, 8072–8080.

Understanding the Chemistry and Physics of the Pu Metal-Oxide Interface with Vibrational and LIBS Spectroscopy

Eliel Villa-Aleman

This project developed spectroscopic tools for the characterization of Ce, U, Pu, and the oxide surfaces. For the first-time, laser ablation breakdown spectroscopy was developed to conduct miniaturized sample analysis in a double-walled cell and scanning electron microscopy was used to identify molten particulates from the laser ablation process.

Introduction

Oxidation of metals such as Ce, U, and Pu leads to the formation of CeO_2, UO_2, and PuO_2, respectively. The interface between the metal and the oxide is characterized by a sub-oxide layer such as Ce_2O_3 and Pu_2O_3. The sub-oxide layer controls the hydriding process and affects the stability of the metal. A set of new tools are required to produce and characterize the suboxide layer in different environments. Laser ablation can be used to clean the surface to enable oxide growth. Laser-induced breakdown spectroscopy (LIBS) can be used to characterize the surface of the material and induce oxidation chemistry.

This project developed new DWCs and spectroscopic tools for the characterization of Ce, U, and Pu metal and oxide surfaces. A highly sensitive LIBS setup was developed for the characterization of small samples. The new LIBS tools enabled the study of spots with 80 mm diameter and with low laser energies (< 500 mJ). For the first time, LIBS of PuO_2 was conducted in a DWC and the temporal evolution of the plasma investigated. The oxide surface and particulates were studied with Raman, infrared, and diffuse reflectance spectroscopy. PuO_2 particulates generated during the laser ablation step were further analyzed for the first time with scanning electron microscopy (SEM). Three different types of particulates were observed in the ablation process: 1) particles from mechanical breakup of the pellet, and 2) molten particulates (10 -30 mm) and spheroids with dimensions less than 500 nm. **Figure 1** shows a PuO_2 pellet and the LIBS spectrum.

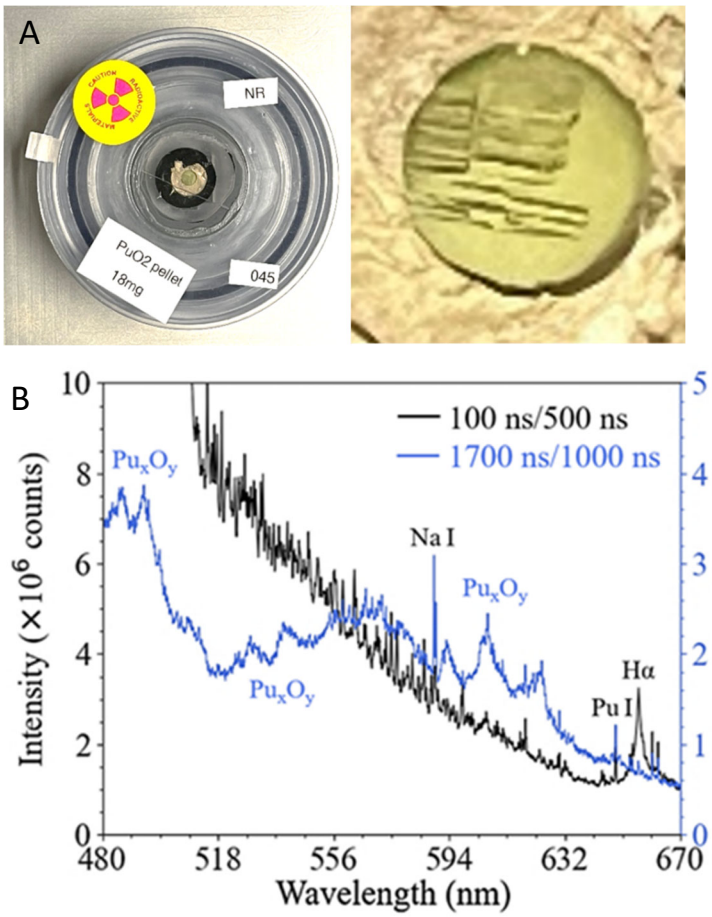

Figure 1. (A) DWC with a PuO_2 pellet and (B) LIBS spectra acquired within 100 and 1700 ns showing the evolution of ionic and atomic spectral lines to molecular emission.

Approach

Handling and characterizing actinide metals is a challenge due to rapid surface oxidation and radioactivity. Ce metal is a surrogate for U and Pu used to test experimental concepts. CeO_2 provided a path for the fabrication of PuO_2 pellets without binders. Ce metal was used to test multiple concepts, including handling in a cell containing

a nitrogen atmosphere to avoid aggressive oxidation. The approach developed with Ce and U enabled us to study PuO_2 pellets. Handling Pu in our radiologically clean lab is limited to quantities less than 50 mg, in contrast to Ce or U. New concepts were required to produce metal oxide pellets, new cells for LIBS, and a highly efficient LIBS system to characterize the materials of interest.

Current LIBS setups used by world-wide researchers employ laser energies ranging from 20 to 200 mJ and laser interrogation spots may be greater than 1 mm. Those experimental conditions are not compatible with the limited amount of Pu material in our lab and the respective smaller pellets with a diameter dimension of ~3 mm. A LIBS setup was assembled to achieve ablation with less than 500 mJ per pulse and 80 mm spots. Ce metal and oxides were used initially and, thereafter, U metal and PuO_2 pellets were used to study particulates generated from the LIBS process and imaged with SEM. **Figure 2** shows SEM images of PuO_2 particulates generated from the laser ablation of the pellet.

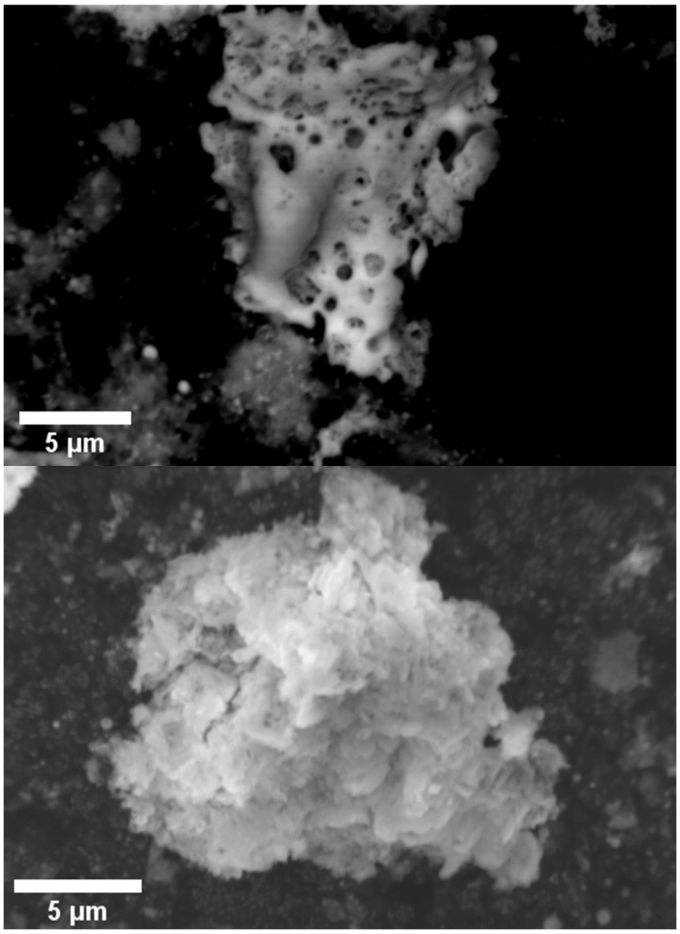

Figure 2. Particulates generated from the laser ablation of a PuO_2 pellet. Irregular and molten particulates are observed in the images indicating temperatures exceeding 2740°C (melting point of PuO_2).

Accomplishments

- Developed CeO_2 and PuO_2 pellets.
- Designed new DWC for conducting LIBS experiments of PuO_2.
- Designed and developed a new LIBS setup for characterization of small samples with minimum energies.
- Characterized LIBS spectrum of Pu_xO_y molecular structures with high spectral resolution.
- Observed, for the first time, the shape and melting process of PuO_2 particulates with SEM.
- Characterized, for the first time, the annealing temperatures of the ablated surface and particulates using Raman spectroscopy.

Peer-reviewed Publication

- "Laser-Induced Plasma in a Double-Walled Cell", Eliel Villa-Aleman, Emily H. Kwapis, Bryan J. Foley, Thomas C. Shehee, Don D. Dick, Jason R. Darvin, Henry M. Ajo, and Kyle C. Hartig under preparation for Applied Spectroscopy.

Team Members

Eliel Villa-Aleman, Jason Darvin, Don Dick, Bryan Foley, Thomas Shehee, Rebecca Carter, Henry Ajo, Tatiana Ayers, Dale Sivils, Emily Kwapis[a+], Kyle Hartig[a]

[a]*University of Florida*
[+]*Graduate Student*

Urban Heat Island Effects on Air and Water Quality in the Augusta Metropolitan Area

Joe Wermter

Urban heat island effects describe warmer temperatures in urban regions. While they are often felt at the surface, they can impact upper-air and water temperatures. The goal of this project is to investigate how the urban heat island of Augusta, Georgia impacts the surrounding weather and hydrology. We will define the UHI effects on this moderately-sized city and develop ways to forecast their impacts.

Introduction

The Urban Heat Island (UHI) is the longest-known anthropogenic impact on weather and climate, but in some cases is one of the least understood[1]. UHI effects encompass increased heat over urban surfaces due to the prevalence of built structures instead of natural soil climatology. Urbanization in the 21st century has led to an amplification in UHI effects, which poses environmental impacts as well as public health risks.

The heat anomalies over urban surfaces lead to increased convection and can lead to increased dispersion of pollution to areas outside of the urban centers[2], as well as influence rainfall[3]. Urban heat can also affect the hydrology of streams that run through the area. We intend to use observation and dispersion modeling to quantify the intensity of Augusta's UHI and its impact on surrounding regions. We will also observe the effects it has on the Savannah River, which runs between Augusta, GA and North Augusta, SC, and is the southern boundary of the Savannah River Site downstream.

The population of the Augusta Metropolitan Area has increased more than 10% in the last decade. Because of increasing urban sprawl in conjunction with overall increased anthropogenic warming, it is critical to define Augusta's UHI impact and model how it could change in the future.

Approach

We investigate the different aspects of Augusta's UHI using a combination of in situ observations, remotely-sensed observations, and numerical modeling depending on the availability of the data. There are three different facets of the atmospheric UHI[4] as well as the hydrologic UHI[5].

The surface UHI describes how urban temperature surfaces are warmer than rural temperature surfaces. These are estimated using satellite-derived surface "skin temperatures," and are simulated using a land-surface model coupled with an atmospheric model.

The "canopy layer" UHI describes urban enhancement of the near-surface air, and is the most familiar form of the UHI observationally. This is analyzed through weather station data at both urban and rural locations around Augusta and is also simulated through weather models.

The "boundary layer" UHI is the enhancement of temperatures within the first ~500-1000m of the atmosphere. Our investigation of this aspect is mostly

[1] Barlow, J. F., Progress in observing and modelling the urban boundary layer. Urban Climate **2014**, 10, 216-240.
[2] Cosgrove, A.; Berkelhammer, M., Downwind footprint of an urban heat island on air and lake temperatures (vol 1, 46, 2018). Npj Clim Atmos Sci **2019**, 2.
[3] McLeod, J.; Shepherd, M.; Konrad, C. E., Spatio-temporal rainfall patterns around Atlanta, Georgia and possible relationships to urban land cover. Urban Climate 2017, 21, 27-42.
[4] Johnson, B.; Shepherd, J. M., An urban-based climatology of winter precipitation in the northeast United States. Urban Climate **2018**, 24, 205-220.
[5] Zahn, E.; Welty, C.; Smith, J. A.; Kemp, S. J.; Baeck, M. L.; Bou-Zeid, E., The Hydrological Urban Heat Island: Determinants of Acute and Chronic Heat Stress in Urban Streams. Journal of the American Water Resources Association **2021**, 57 (6), 941-955.

limited to numerical modeling since observations of the boundary layer are very temporally sparse and not within the Augusta area of focus. These effects can impact rainfall, which is explored through a combination of convection modeling and radar-derived rainfall estimates.

The "hydrologic" UHI is a newly-explored facet that describes how adjacent stream temperatures are affected by rainfall runoff from hot urban surfaces. This is measured in the Savannah River using an array of measurements provided by the Phinizy Center for Water Sciences and the City of Augusta and is also simulated using both SRNL and publicly-available hydraulic models.

Accomplishments

- Co-I.s Appelbaum and Shepherd of UGA have found a strong surface UHI using satellite analyses (**Figure 1**), with surface temperature deviations of ~15°C in the urban and suburban regions of Augusta.
- P.I. Wermter and Co-I. Thomas have conducted simulations of a warm-season rain event northwest of Augusta and found that while all models under-predicted rainfall in the region, the total downwind rainfall production varied depending on the urban parameterization used in the simulation (**Figure 2**).
- Co-I. McLeod found an increase in radar-derived daily rainfall over and around the Augusta Metropolitan Area (**Figure 3**) as well as a diurnal urban-forced pattern of cloud cover in the region.
- P.I. Wermter conducted several simulations of Augusta's urban boundary layer and found a curious connection between the nocturnal boundary layer impacts of Augusta and Columbia, South Carolina (**Figure 4**).
- Co-I. Turner implemented bathymetry for the Savannah River near Augusta and input the data into SRNL's ALGE3D model (**Figure 5**).

Peer-reviewed Publications

- Wermter, J.; Thomas, A.; Impacts of Urban Parameterizations on Simulated Rainfall Downwind of Augusta, Georgia. **2023.** *Manuscript Complete; Submitting to Atmosphere pending General Counsel review.*

- McLeod, J.; Shepherd, J.M.; Appelbaum, M.; Evidence of cloud and rainfall modification in a mid-sized urban area – a climatological analysis of Augusta, Georgia. **2023.** *Submitted to City and Environment Interactions*

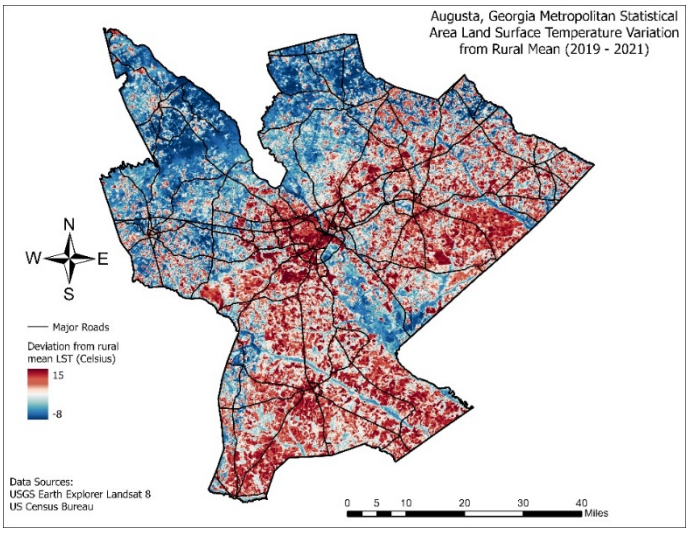

Figure 1. Landsat-derived midday skin temperature deviations from the rural mean of the Augusta Metropolitan Area.

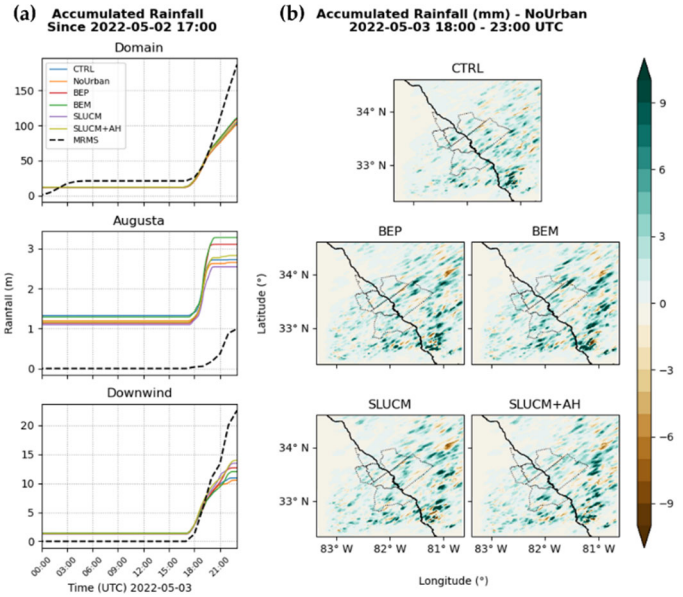

Figure 2. Accumulated rainfall from the Weather Research and Forecasting (WRF) model simulations utilizing several different urban parameterizations compared to (a) Multi-Radar Multi-Sensor (MRMS) rainfall estimates and (b) the simulation in which the urban surface was replaced with natural land-cover.

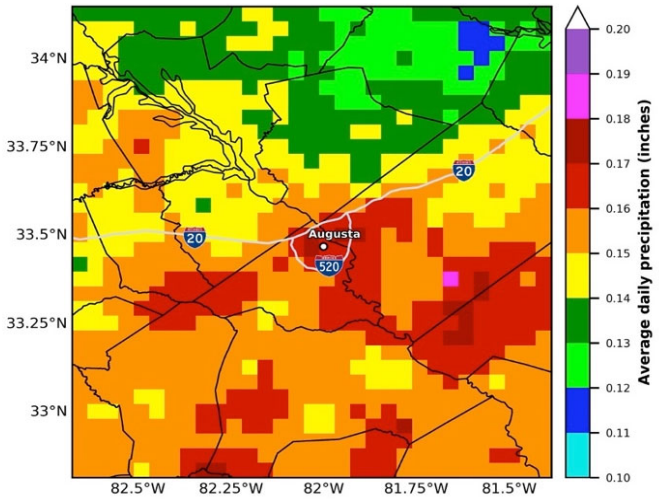

Figure 3. Average daily precipitation during June-July-August (JJA) from 2002–2019.

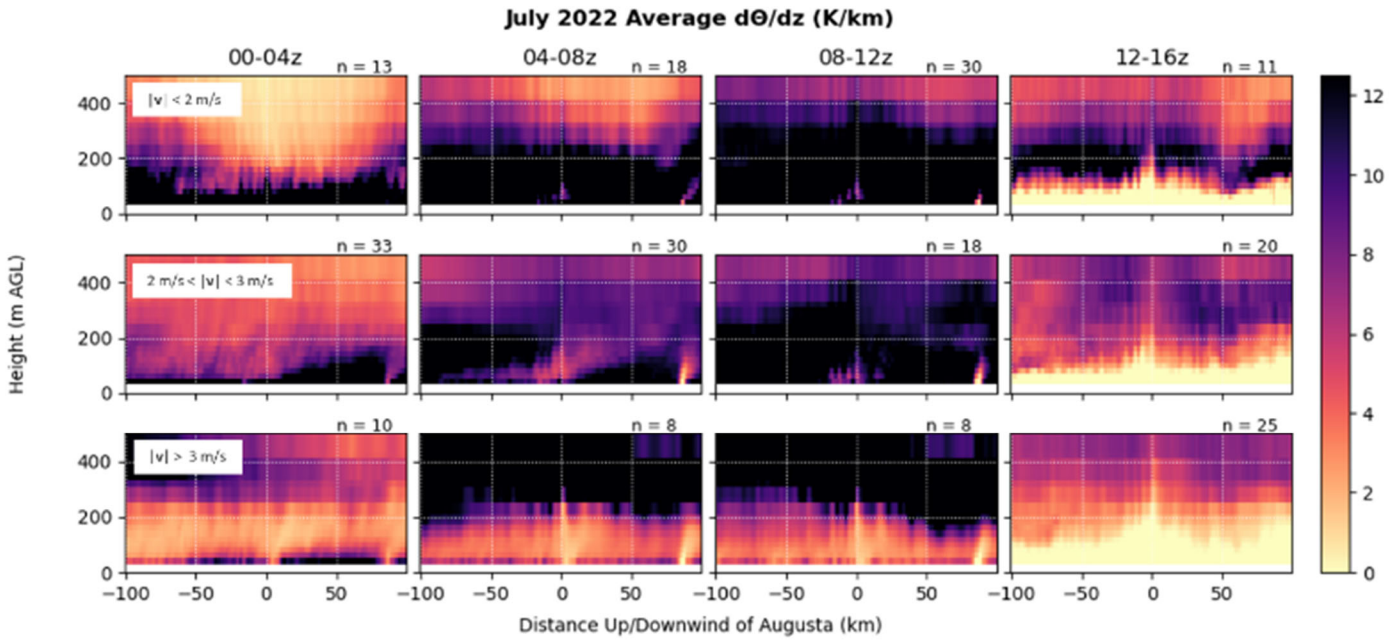

Figure 4. Wind direction-following cross-sections of vertical potential temperatures gradients within the nocturnal boundary layer, centered at the Augusta urban center averaged for July 18-25, 2022.

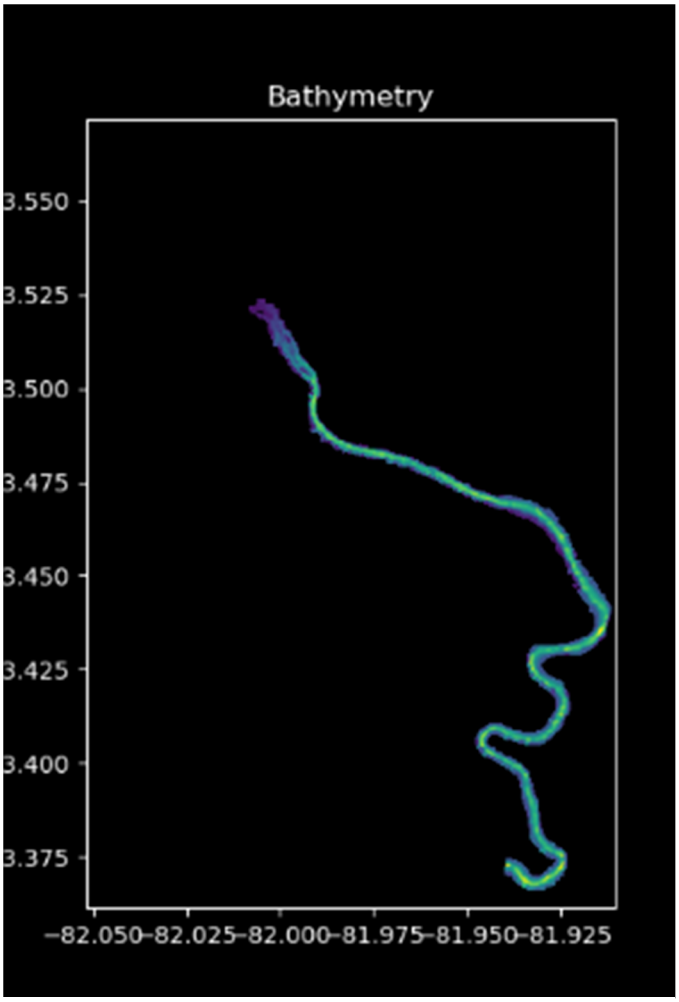

Figure 5. Bathymetry from the Savannah River used in SRNL's ALGE3D model.

Team Members

Vivian Turner, Andrew Thomas[*], Marshall Shepherd[a], Max Appelbaum[a**], Jordan McLeod[b]

[a]*University of Georgia*
[b]*University of South Alabama*
[*]*Postdoctoral Researcher*
[**]*Graduate Student*

FY23 PROJECTS

CORE COMPETENCY:

Creating Manufacturing and energy solutions for EM, NNSA, and other sponsors

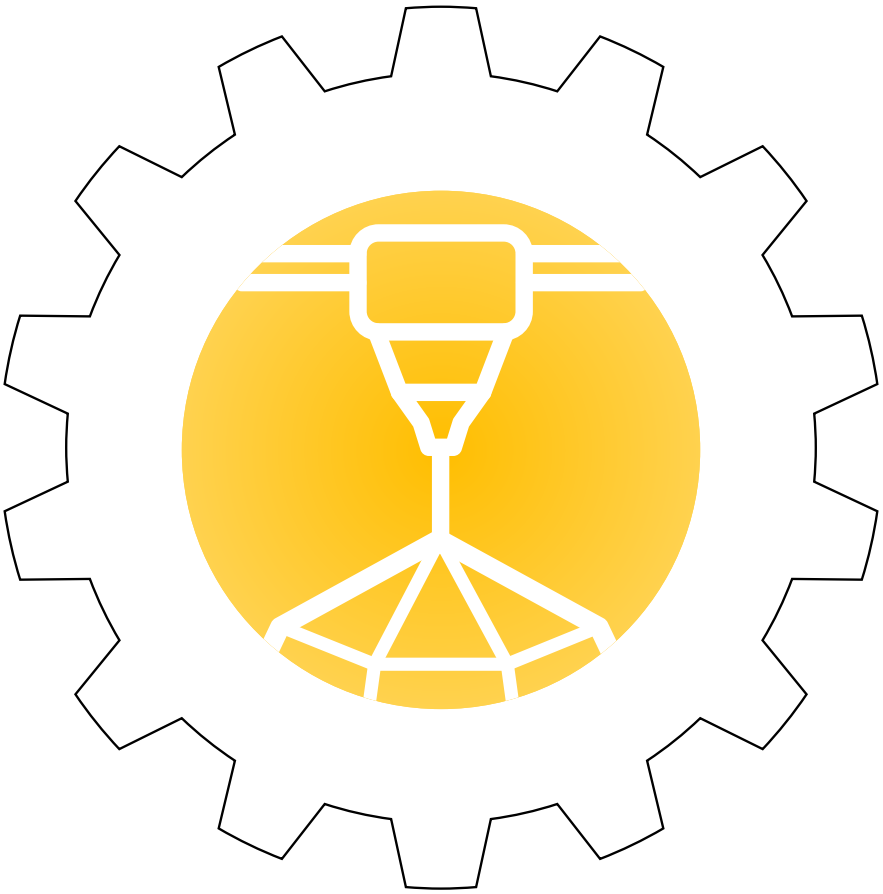

Re-Imagining Additive Manufacturing

Donald Benza, Camden Chatham

The use of polymer blends has traditionally afforded tunable mechanical, chemical and thermal properties of objects manufactured from them, but requires multiple steps to achieve the desired performance. Methods for creating polymer blends through layer-wise chemical modification and material layering were explored to reduce the total steps needed for compatibilized blend part production.

Introduction

Blending dissimilar polymers is a cost-effective method to tune mechanical, chemical, and thermal properties of polymers parts into ranges not easily achievable with homopolymer feedstock alone. Most polymer blends are inherently incompatible as binary mixtures due to chemical dissimilarities between each constituent or phase of the blend. This also manifests as high interfacial tension at natural domain boundaries after melt processing, leading to reduced mechanical strength. Often, compatibilizers or other chemical modifiers are added to incompatible blends during melt processing to decrease the interfacial tension and increase polymer dispersion as part of a multi-step preparation process before part manufacturing [1]. Methods for polymer blend compatibilization during manufacturing as a one step process were explored during FY23 to include both *in situ* chemical modification and controlled, repeated layering of dissimilar polymers. Specifically, the science explored pertaining to each of these methods respectively are (i) the effects of melt state chemical reactions by a reactive gas on an uncompatibilized polymer blend's thermomechanical behavior and (ii) the effect of layer height and the number of interfaces on repeated alternating polymer layering behavior. Further development and understanding of each of these methods could allow for the creation of new polymer blends in a one step process that exhibit improved mechanical, thermal and chemical properties while minimizing carbon footprints. The techniques explored during this project may have significant applicability to mixed municipal polymer waste handling *without* the need for deconstruction into low-molecular weight species, which is a significant challenge outlined by DOE steering documents [2-4].

Approach

During FY23, incompatible polymer blends of 50/50 w/w% Bisphenol(A)polycarbonate (BPA-PC) and polystyrene (PS) were additively manufactured (AM) in an atmosphere containing ozone and UV light to take advantage of the intimate access to each voxel that AM affords [5]. The chemical modification of the BPA-PC/PS blend in the melt state by ozone and UV light populates each respective phase of the blend with oxygen functional groups, increasing the phase-to-phase chemical similarity [6-9]. Conceivably, a second chemical modifier may then be deposited after the ozone pretreatment to enable crosslinking across phase boundaries, increasing the compatibility of the blend [10]. Both computational thermodynamic modeling of the reaction pathways between the blend and UV/O_3 and a plethora of polymeric characterization techniques typical for evaluating AM polymers were employed to understand the effect that the ozone pretreatment has on the thermomechanical properties and behavior of the BPA-PC/PS blend.

Additionally, a dual extrusion Fused Filament Fabrication (FFF) AM machine (Ultimaker S3) was used to create test coupons with alternating layers of BPA-PC and PS. The thickness of each layer and the number of layers were modulated to observe changes in the thermomechanical behavior of the blend as well as the blend's tensile properties. These samples were compared to test coupons comprised of a traditionally melt processed blend of BPA-PC and PS at a 50% w/w ratio.

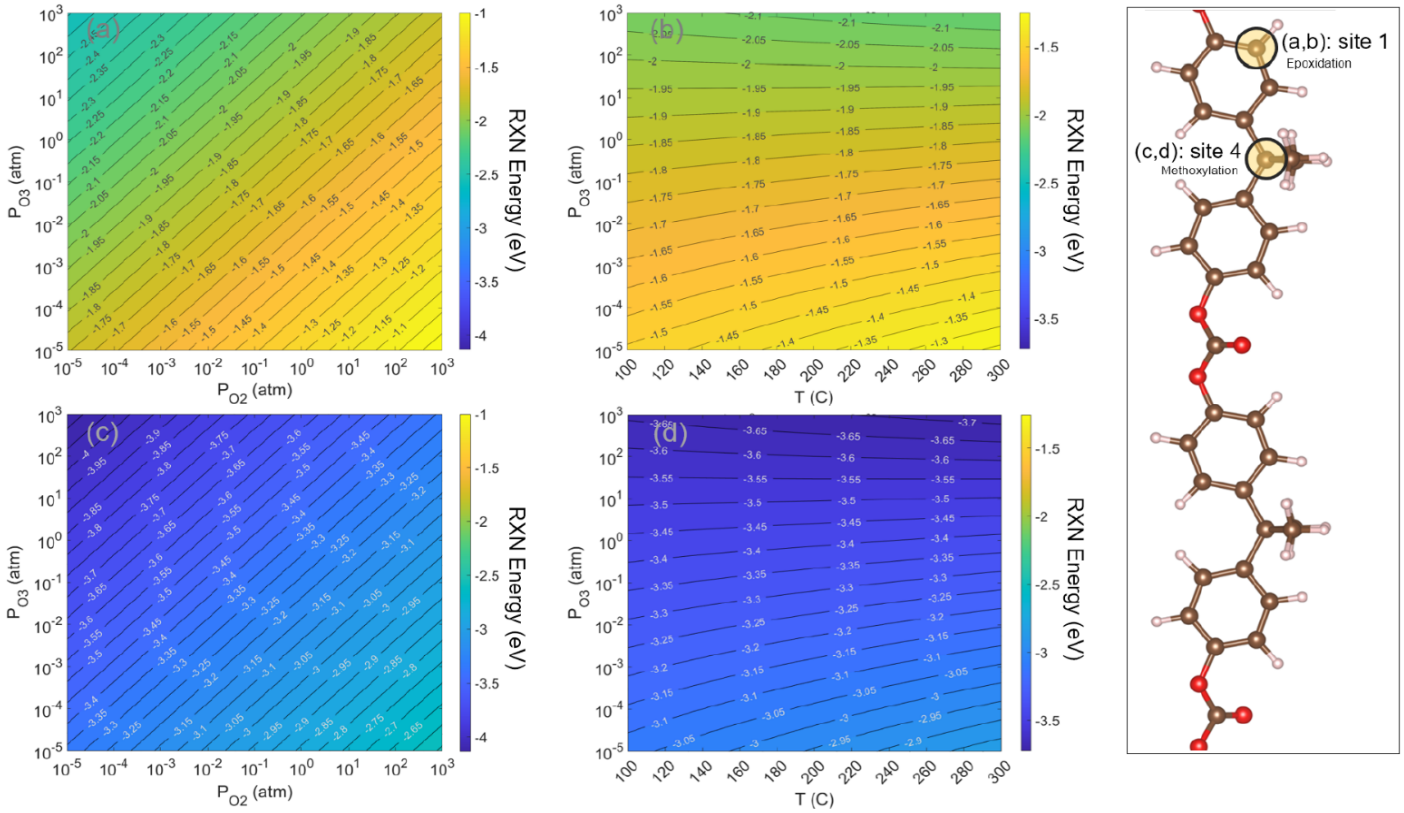

Figure 1. Reaction energies of O3 with site 1 and site 4 versus temperature, ozone pressure, and oxygen pressure. The leftmost column (a,c) shows the reaction energies as a function of PO2 and PO3 with a fixed temperature of 230◦C. The middle column (b,d) shows

Accomplishments

In situ Chemical Modification of BPA-PC by UV/O_3 During Additive Manufacturing

- Completed computational modeling of the reaction pathways between melt state BPA-PC and UV/O_3, **Figure 1**. This modeling indicates that aromatic epoxide and methoxyl formation are the dominant reaction pathways, with some chain cleavage also expected to occur at C-O bonds along the BPA-PC chain under UV excitation.
- The simulated reaction products should increase polymer free volume leading to a decrease in the glass transition temperature as well as interferences with BPA-PC's normal crystallization mechanisms.
- UV/vis measurements of BPA-PC modified by UV/O_3 during printing confirm computational model expectations of 300nm and 360nm features associated with aromatic epoxide formation, **Figure 2**. Direct UV/vis evidence of methoxylation is, however, obscured by the epoxide signature.
- Pressure printing of BPA-PC cubes at Virginia Tech (VT) demonstrates the necessity of performing chemical modifications *in situ* instead of *post hoc,* as is traditionally done: Cubes printed in UV/O_3 mixture at 0, 5, 10, and 15 PSIG exhibit SRNL-observed characteristic color change throughout bulk of part, whereas those initially printed in air and only later exposed to a pressurized UV/O_3 environment exhibit color change only on the outermost "skin".

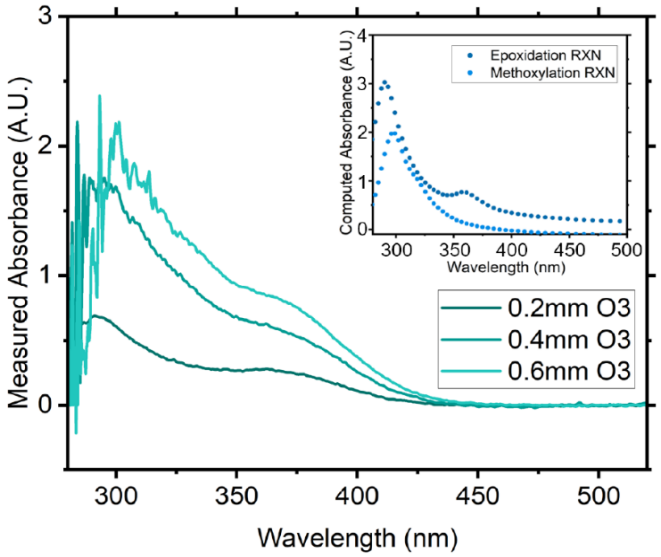

Figure 2. Experimental UV/vis spectra of UV/ozone modified AM BPA-PC disks. (Inset) simulated UV/vis

- FTIR characterization of UV/O_3 modified PS surfaces indicate an increase in oxygen species in the carbonyl (C=O) region (1735 cm^{-1}) which completes after 80 seconds at processing conditions (90 °C, 0.9 wt% O_3 at a flow rate of 3.2 SLPM), **Figure 3**.

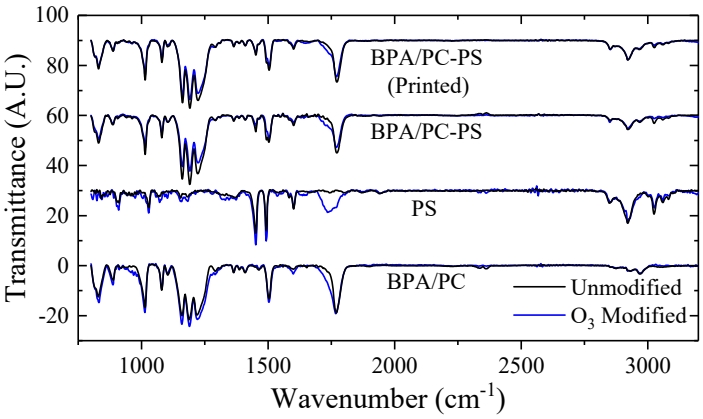

Figure 3. ATR-IR spectra of unmodified and ozone modified BPA-PC, PS, and BPA-PC/PS filaments and unmodified and ozone modified printed BPA-PC/PS dogbone specimens.

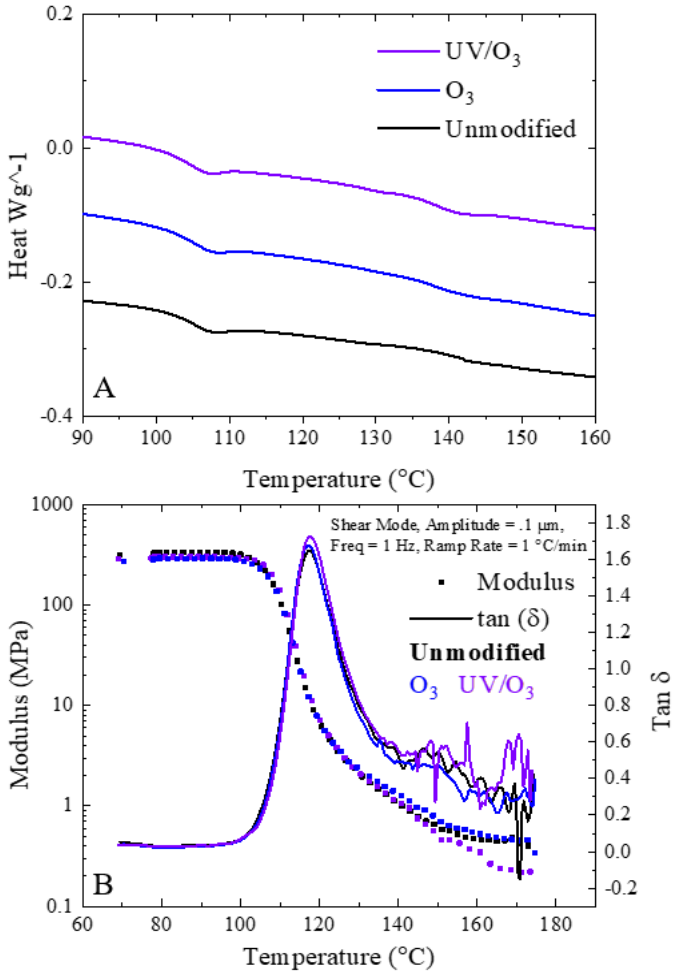

Figure 4. A) Calorimetric (10 °C min-1, exo up) and B) Thermomechanical analysis of unmodified, O3 modified, and UV/O3 modified printed samples.

- The addition of carbonyls to PS, which is inherently devoid of oxygen, represents an increase in chemical similarity to BPA-PC.
- Additionally, with both blend components now having common reaction sites, further modifications to crosslink across phase boundaries may be possible.
- Simple chemical modification of BPA-PC/PS blends by UV/O_3 during manufacturing does not significantly increase blend compatibilization, **Figure 4**.
- Dynamic Mechanical Analysis (DMA) and Differential Scanning Calorimetry (DSC) spectra showed no change for the PS phase, but a decrease of 6 °C for the BPA-PC phase. The expected behavior, were the compatibilization increased, is for the glass transition temperatures of both phases to shift towards one another.
- Tensile properties of the BPA-PC/PS blend are statistically unaffected in uniaxial tension to failure, **Figure 5,** indicating that despite the chemical modifications to both polymers, the natural domain boundary interfacial properties still dominate the performance of the blend.

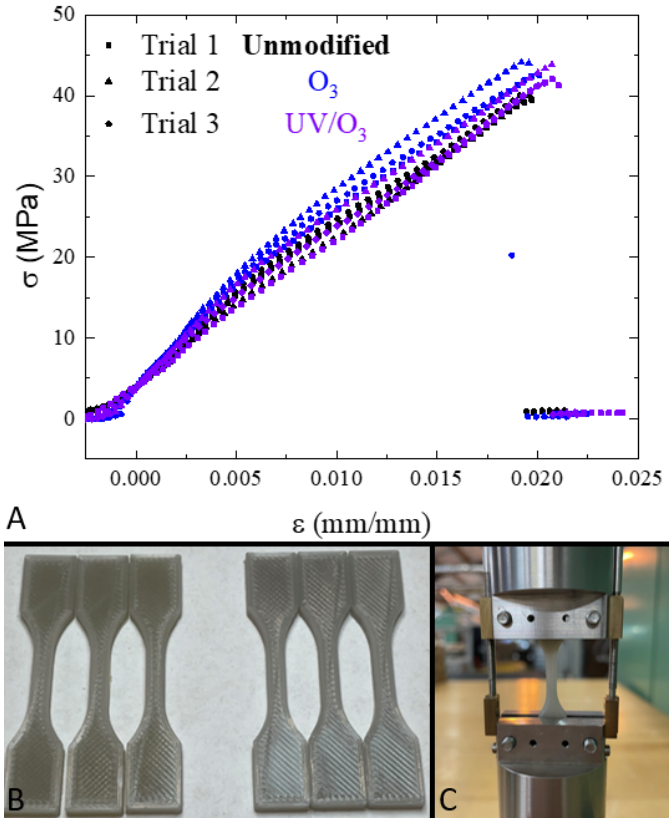

Figure 5. Tensile testing of unmodified, ozone modified, and UV/ozone modified BPA-PC/PS printed dogbone blends. Photographs of B) ozone modified (left) and unmodified (right) tensile bars and C) tensile bars loaded into the MTS Deben Microtest.

Hybrid FFF/Inkjet Printing (VT)

- A FFF AM machine was outfitted with an additional inkjet head to deposit magnetic iron oxide nanoparticles (IONPs) (30 nm, 5 mg/ml) or carbon nanotubes (CNTs) suspended in distilled water between each deposited layer. These remain dormant until activated during post-manufacturing, then cause selective internal heating, **Figure 6**, reflowing interfaces, closing gaps, and reducing porosity. This improves z-direction tensile properties.
- IONPs were successfully deposited at the layer interface, but digital radiography showed significant aggregation, and simulations showed that this IONP size would struggle with heating – this was born out by experiment.
- Carbon nanotubes were successfully deposited at the layer interface and showed temperature increases up to 219 °C under microwave heating at high concentrations.

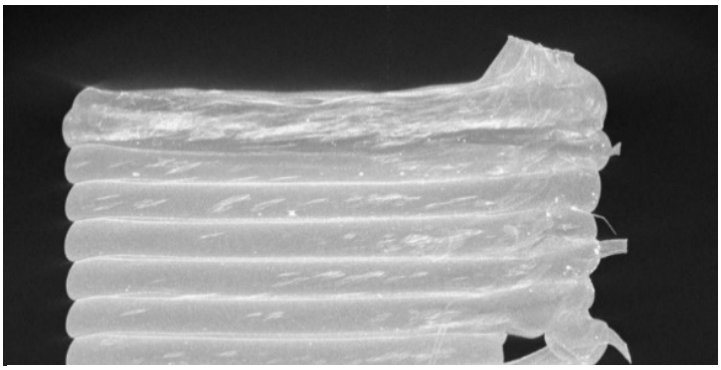

Figure 6. Radiograph of IONPs deposited at the layer interface of BPAPC printed parts.

- Particles may also be suspended in a liquid reagent to enable crosslinking during reflow and other novel polymer chemistry modifications. *Alternating Material Layer Dual Extrusion Printing*
- Leveraged the dual-extrusion capability of the procured Ultimaker S3+ FFF printers to explore the influence of macro-scale spatial arrangement of dissimilar polymer domains on (i) oscillatory shear modulus, (ii) shear creep recovery, and (iii) ultimate tensile strength. Specimens with alternating layers of PS and BPA-PC were fabricated, and results were compared against a traditionally prepared blend (i.e., twin screw extruder at 50 % w/w).
- Temperature-dependent shear modulus from alternating layer specimens was found to closely track the modulus of the twin-screw blended specimens, demonstrating similar shear performance while eliminating the extra processing step of pre-print twin-screw blending.
- Creep recovery was observed to vary with layer height for all tested specimens. The effect of layer height appears reduced for the alternating layer specimens compared to those prepared by twin-screw blending, **Figure 7**.
- Ultimate tensile performance was evaluated for two homopolymer samples (PS and BPA-PC), the twin screw blended filament, and a sample containing a single interface between PS and BPA-PC domains. As expected for 3D printed and un-compatibilized samples, the homopolymers exhibited the highest strength. The twin screw blended filament tested at roughly half the homopolymer strength, and the single interface tested at roughly half the strength of

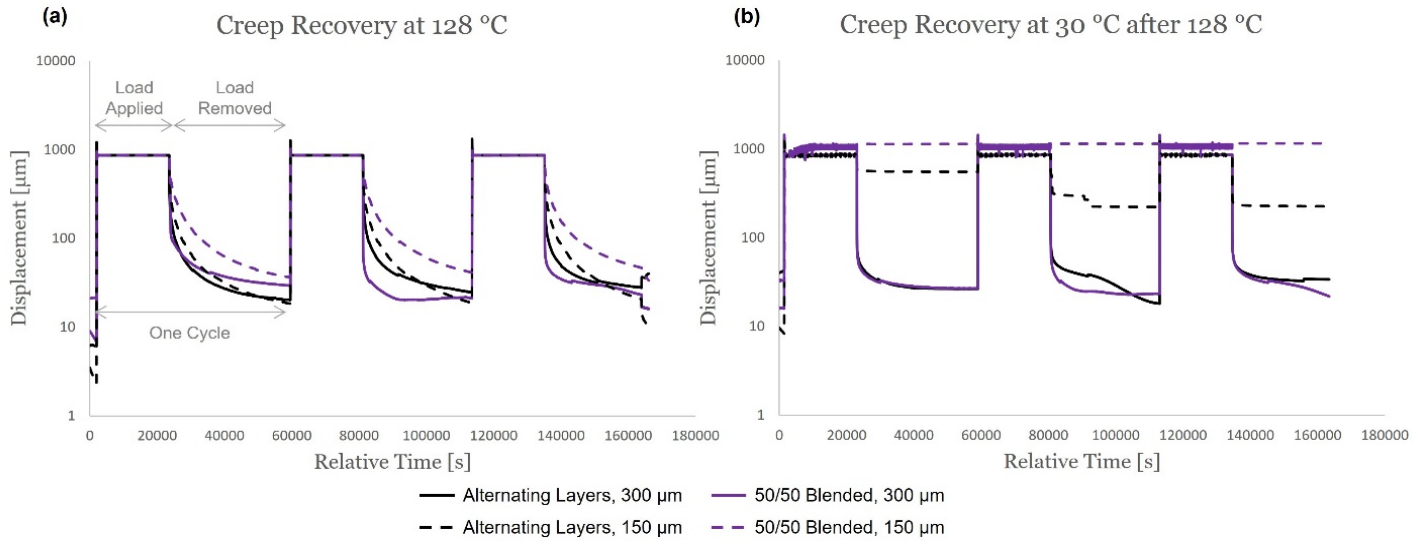

Figure 7. Shear creep recovery for homopolymers, twin-screw blended filament, and samples fabricated from alternating homopolymer layers of PS and BPA-PC. (a) Depicts creep recovery at 128 °C, which is above polystyrene's glass transition temperature but below that of polycarbonate. (b) Depicts creep recovery at room temperature following high temperature exposure. Creep recovery assessed after 30 N applied force for 6 h followed by 8 h recovery time.

the blended filament. Tensile modulus shows a similar trend, though not to the same degree.
- The differences between shear, creep, and tension loading behavior emphasize the importance of considering multiple properties before drawing final conclusions regarding layerwise manufacturing of materials.

Peer-reviewed Publications

- "Fused filament fabrication of polymer blends with in situ layerwise chemical modifications" *Proceedings of the Solid Freeform Fabrication Symposium* Accepted September 2023.
- "A comparison of mechanical properties from natural and process-induced interfaces in filament extrusion AM of polymer blends" *Proceedings of the Solid Freeform Fabrication Symposium* Accepted September 2023.

Oral Presentations

- Benza, D; Chatham,C.A; Baker, J. "Fused filament fabrication of polymer blends with in situ layerwise chemical modifications" The Solid Freeform Fabrication Symposium, Austin, TX, August 14-16, 2023.
- Chatham,C.A; Benza, D; "A comparison of mechanical properties from natural and process-induced interfaces in filament extrusion AM of polymer blends" " The Solid Freeform Fabrication Symposium, Austin, TX, August 14-16, 2023.

Poster Presentations

- Benza, D; Chatham,C.A; Baker, J. "Re-Imagining Additive Manufacturing (AM)" 2023 BSRA University Collaboration, Augusta, GA, June, 21.

Intellectual Property

Patent Applications

- Method for Controlling Local Environment Exposure During Additive Manufacturing- 063546/0454
- Method for in situ Chemical Modification During Additive Manufacturing- PCT/US23/27958

Team Members

Donald Benza, Camden A. Chatham, E. Cade Willis, Andrew Rhodes, Jonathon Baker, Louis McNamara, Robert Lascola, Christopher Williams[a], Michael Bortner[a], Devin Johnson[+], Malik Blackman[b**], Ian Ho[a**]

[a]*Virginia Polytechnic Institute & State University*
[b]*Georgia Institute of Technology*
[**]*Graduate Student*
[+]*Undergraduate Student*

References

1. Utracki, L.A., Compatibilization of polymer blends. the Canadian journal of chemical Engineering, 2002. 80(6): p. 1008-1016.
2. Fitzgerald, N., et al., Plastics for a Circular Economy Workshop: Summary Report. 2020, US Department of Energy (USDOE), Washington DC (United States). Office of ….
3. Britt, P.F., et al., Report of the Basic Energy Sciences Roundtable on Chemical Upcycling of Polymers. 2019, USDOE Office of Science (SC)(United States).
4. Jenks, C., et al., Basic Research Needs for Transformative Manufacturing. 2020, USDOE Office of Science (SC).
5. Chevallier, C., F. Becquart, and M. Taha, Polystyrene/polycarbonate blends compatibilization: Morphology, rheological and mechanical properties. Materials Chemistry and Physics, 2013. 139(2-3): p. 616-622.
6. Fang, J., Y. Xuan, and Q. Li, Preparation of polystyrene spheres in different particle sizes and assembly of the PS colloidal crystals. Science China Technological Sciences, 2010. 53: p. 3088-3093.
7. R.O.F. Verkuijlen , M.H.A.v.D., A.A.E. Stevens , J. van Geldrop , J.P.C. Bernards, Surface modification of polycarbonate and polyethylene naphtalate foils by UV-ozone treatment and µPlasma printing. Applied surface science, 2014. 290: p. 381-387.
8. Davidson, M.R., S.A. Mitchell, and R.H. Bradley, Surface studies of low molecular weight photolysis products from UV-ozone oxidised polystyrene. Surface science, 2005. 581(2-3): p. 169-177.
9. Callen, B.W., et al., Remote plasma and ultraviolet–ozone modification of polystyrene. Journal of Vacuum Science & Technology A: Vacuum, Surfaces, and Films, 1995. 13(4): p. 2023-2029.
10. Perryman, S.C. and M.D. Dadmun, Incorporating crosslinks in fused filament fabrication: Molecular insight into post deposition reactions. Additive Manufacturing, 2021. 38: p. 101746.

Bipolar Plates Design and Testing for Alkaline Electrochemical Systems

H. Colón-Mercado

The objective of this project is to develop next generation alkaline electrochemical systems by designing low cost, high efficiency bipolar plates (BPs) that meet current DOE technical targets. These bipolar plates will result in lower commercialization barriers of cost and ease of manufacturing associated with electrochemical systems.

Introduction

Performance, cost, and durability of alkaline electrochemical systems are the key factors that govern the commercialization of H_2-based energy devices such as unitized regenerative fuel cells (URFCs), fuel cells (FCs), and electrolysis cells (ECs). While alkaline systems offer advantages of high energy density vs. existing energy conversion systems, their cost prevents commercialization. Bipolar plates influence many of the system barriers such as cost, lifetime, and performance. While the development of BP is recognized by funding agencies, the research is in its early stage of development and is not a saturated field. This project seeks to address the major obstacles in BP design to develop commercially friendly BP for alkaline electrochemical systems. In this project, SRNL, in collaboration with the University of South Carolina (UofSC), is working on the development of next generation BPs that address most of the metrics outlined by funding agencies such as the Department of Energy-Energy Efficiency and Renewable Energy (DOE-EERE). Our research focused on the development of low-cost thin BPs that perform equal to or better than research grade BPs. We (1) developed surface finishes and high-performance thin films for corrosion protection applications, (2) designed new flow fields with improved mass transport and heat rejection, and (3) enhanced component test capability for the evaluation of new experimental components being developed at SRNL.

Approach

SRNL utilized its expertise in electropolishing and electroplating to coat different substrates considered as alternate alloy materials, such as aluminum and stainless steel, for preparing BPs. Figure 1 shows the comparison of bare aluminum alloy strip and ~10 µm thick electroless Ni plated on aluminum alloy bipolar plate before and after immersion in 0.1M KOH, for 24h and 100h, respectively. The solution concentration was selected since it is currently used in the alkaline water electrolyzer. Bare aluminum alloy showed dissolution of Al in the electrolyte (**Figure 1A**) while electroless Ni plated bipolar plate did not show any underlying metal dissolution (**Figure 1B**).
Figure 2 shows the scanning electron microscopy (SEM) images of Ni porous transport layer (PTL) impregnated with varying amounts of polytetrafluoroethylene (PTFE). The PTFE is needed in the alkaline electrolyte membrane (AEM) water electrolyzer oxygen evolution reaction (OER) electrode to tailor the hydrophilic/hydrophobic properties for the easy transport of reactant (water) and product (oxygen).

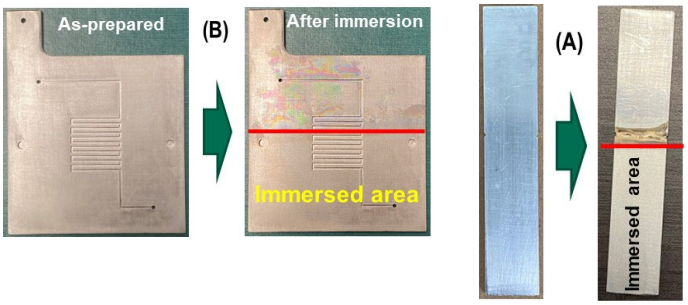

Figure 1. Photographs of (A) bare aluminum alloy and (B) electroless Ni plated on aluminum alloy plates before and after immersion in 0.1M KOH.

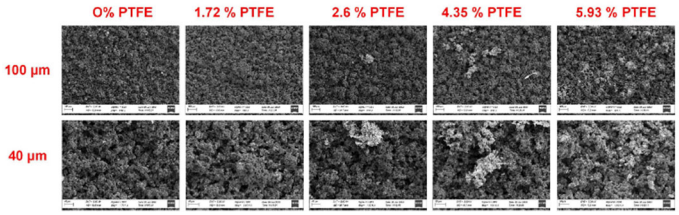

Figure 2. SEM images of bare and PTFE impregnated Ni PTLs.

Based on the SEM images and visual observations, 1.72 wt% PTFE impregnated PTL was selected for the preparation and testing of OER electrode in alkaline electrolyzer. The electrolyzer performances of bare and 1.72 wt% PTFE impregnated Ni PTL based OER electrodes (5-cm^2) are compared in **Figure 3**. The figure shows that at an applied total current of 1A, the bare Ni PTL based electrode showed 1.55V up to 40h of operation. However, the 1.72 wt% PTFE based Ni PTL showed initial cell voltage of ~1.55V up to 20h of operation, started to stabilize after ~40h and exhibited a cell voltage of ~1.42V, a 130mV difference in performance.

Figure 4 compares the effect of Nafion® addition in the OER and hydrogen evolution reaction (HER) electrodes on the electrolyzer performance. **Figure 4 (a)** shows that the addition of Nafion® (brown trace) in the OER electrode has significantly improved the electrolyzer performance by 100mV at an operating current density of 2A/cm^2 when compared to the OER electrode with no Nafion® addition (red trace). Furthermore, the Nafion® addition not only enhanced the electrolyzer performance, but it also improved the electrolyzer life as indicated by the short-term test results shown in **Figure 4(b). Figure 5** compares the effect of Nafion® addition on the alkaline water electrolyzer performance and shows the optimum conditions to operate the alkaline water electrolyzer. As shown in the figure, the operating temperature has a significant influence on the electrolyzer performance. That is, the initial performance (black solid line trace in **Figure 5**) slowly degraded (blue solid line trace) when operating the cell at 60°C; however, the cell performance reverted to the initial performance after 19h when the operating temperature is increased to 80 °C (red dotted line trace). Moreover, high operating temperature (80 °C) and high KOH concentration (1.0M) resulted in significantly higher electrolyzer performance. Unfortunately, these operating conditions are harsh for the alkaline exchange membranes.

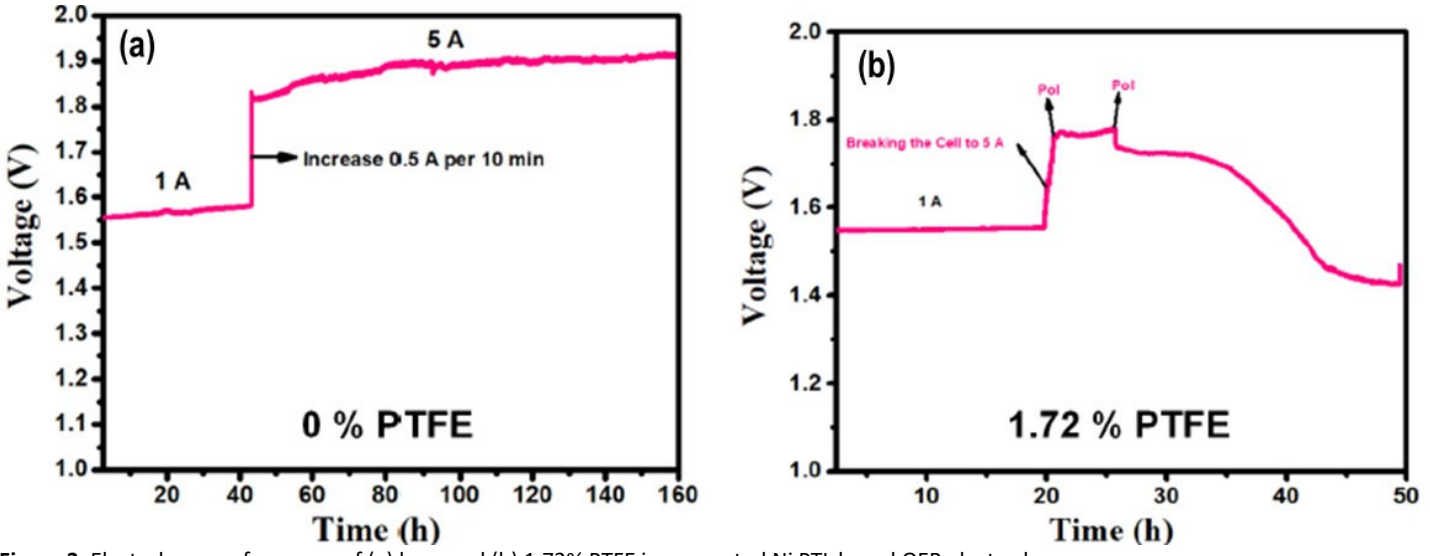

Figure 3. Electrolyzer performance of (a) bare and (b) 1.72% PTFE impregnated Ni PTL based OER electrode.

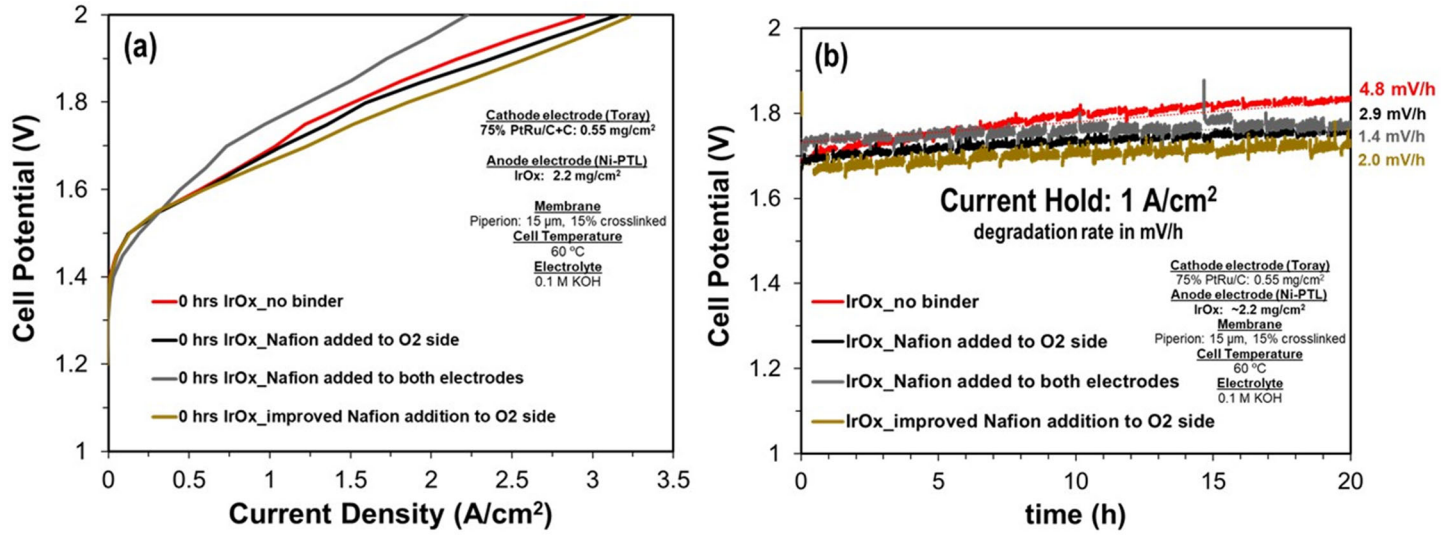

Figure 4. Comparison of the effect of Nafion® addition on the (a) initial and (b) short-term stability of alkaline water electrolyzer performance.

The results of this effort set the stage to apply for future funding in the alkaline electrolysis area of research. New electrode composition shows not only improved performance, but also improved durability. Additionally, thin film deposition is a viable approach to low-cost bipolar plate fabrication.

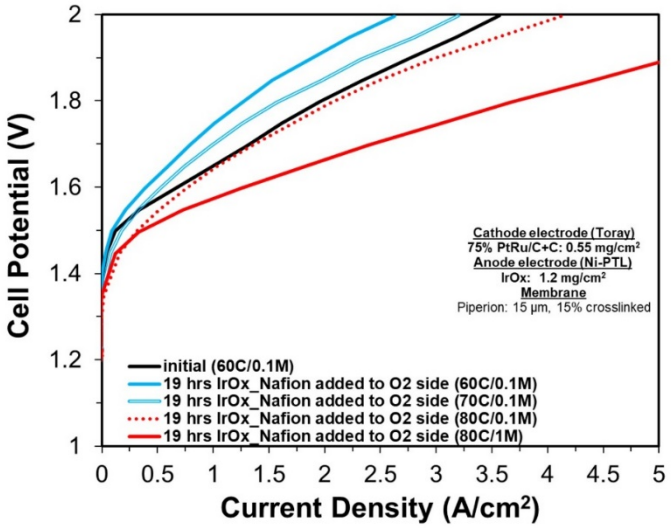

Figure 5. Comparison of the effect of operating temperature and KOH concentration on the Nafion® added OER electrode performance.

Accomplishments

- Successfully coated defect-free ~10 µm thick coating of electroless Ni on to aluminum alloy bipolar plates and demonstrated its corrosion protection properties
- Optimized the oxygen evolution reaction electrode in the membrane electrode assembly (MEA) and tested its performance in 5 cm^2 nickel bipolar plates.
- Achieved high water electrolysis performance by optimizing the electrode composition and porous transport media properties as compared to traditional electrodes

Peer-reviewed Publications

- Noor Ul Hassan, Elaine Motyka, Jonathan Kweder, Prabhu Ganesan, Bryce Brechin, Barr Zulevi, Héctor R. Colón-Mercado, Paul A. Kohl, and William E. Mustain. "Effect of porous transport layer properties on the anode electrode in anion exchange membrane electrolyzers." Journal of Power Sources 555 (2023): 232371.

Team Members

Prabhu Ganesan, Bryce Brechin, Mohammed Al Murisi[a], William Mustain[a], Noor Ul Hassan[a*], Mohammed Al Murisi[a*]

[a]*University of South Carolina*
[*]*Graduate Student*

Accelerated Discovery of W-Re-Ta-Mo Refractory Medium Entropy Alloy for Extreme Conditions

Guru Dinda

This report summarizes the methodology under development for the accelerated discovery of W–Re–Ta–Mo refractory ductile medium entropy alloys for harsh service conditions, specifically for hydrogen and low-carbon fuel turbines, rocket nozzles, space nuclear propulsion systems, and advanced next generation nuclear reactors.

Introduction

Extreme environment applications require components that must have elevated temperature corrosion and oxidation resistance, strength, toughness, and wear resistance that are rarely found in a single material. Refractory alloys such as W and Mo based alloys can withstand high operating temperatures. However, refractory alloys exhibit intrinsic brittleness and oxidation-susceptibility, which remains a significant challenge for their processing and application in harsh service conditions. There has been increased demand for structural materials that can withstand extreme environments. However, traditional alloy design and alloy selection are practically restricted by one alloy at a time concept. Given the vast universe of potential alloys that can be created, the conventional method of synthesizing and testing samples one at a time is too slow for exploring the broad range of novel materials. To overcome the limitations of the current refractory materials, the SRNL team is developing a high-throughput alloy development technique based on the laser-based directed energy deposition principle coupled with integrated computational modeling and high-throughput materials synthesis and screening. This dramatically reduces the time to discover new W-Re-Ta-Mo refractory medium entropy alloys for extreme environment applications. To demonstrate the proposed high-throughput alloy development concept, the team has developed a laser-based directed energy deposition system based on a 3-kW diode laser, six-axis robotic arm, coaxial nozzle, and four powder feeders. It is expected that the proposed high-throughput alloy development technique will be used extensively to explore various alloy libraries to discover many new high-performance materials.

Approach

In pursuit of the proposed goal, the research plan is divided into two interconnected research aims: (1) Design W–Re–Ta–Mo refractory medium entropy alloy composition space via CALPHAD-based solidification modeling, and (2) Establish a high-throughput alloy synthesis and screening procedure via laser-based directed energy deposition process.

Alloy design: The SRNL team employed an equilibrium solidification model to simulate the composition and mole fraction of equilibrium phases in the W-Re-Ta-Mo quaternary system. The primary objective of this task is to determine the solid solution phase boundary in the W-Re-Ta-Mo composition space. The second objective of the CALPHAD simulation is to establish the composition window of the W-Re-Ta-Mo alloys with solidus temperature > 3000 ^{o}C. The results, as shown in **Figure 1**, revealed that the only solid solution phases exist in the lower Re side (<15%) with any combination of W, Mo, and Ta.

High-throughput alloy synthesis: Laser-based directed energy deposition is an additive manufacturing technique where the powder is fed into the melt pool created by a high-power laser beam to form an overlay layer of material, as shown in **figure 2**. Usually, the powder consists of a single material, but multi-component materials can be synthesized by fusion of the incoming powders followed by in-situ mixing of different powders. By varying the feed rate of various incoming powders, clad tracks with compositions following any pre-set variation can be rapidly produced. This offers a unique possibility for rapid preparation of a complete spectrum of materials with varying compositions.

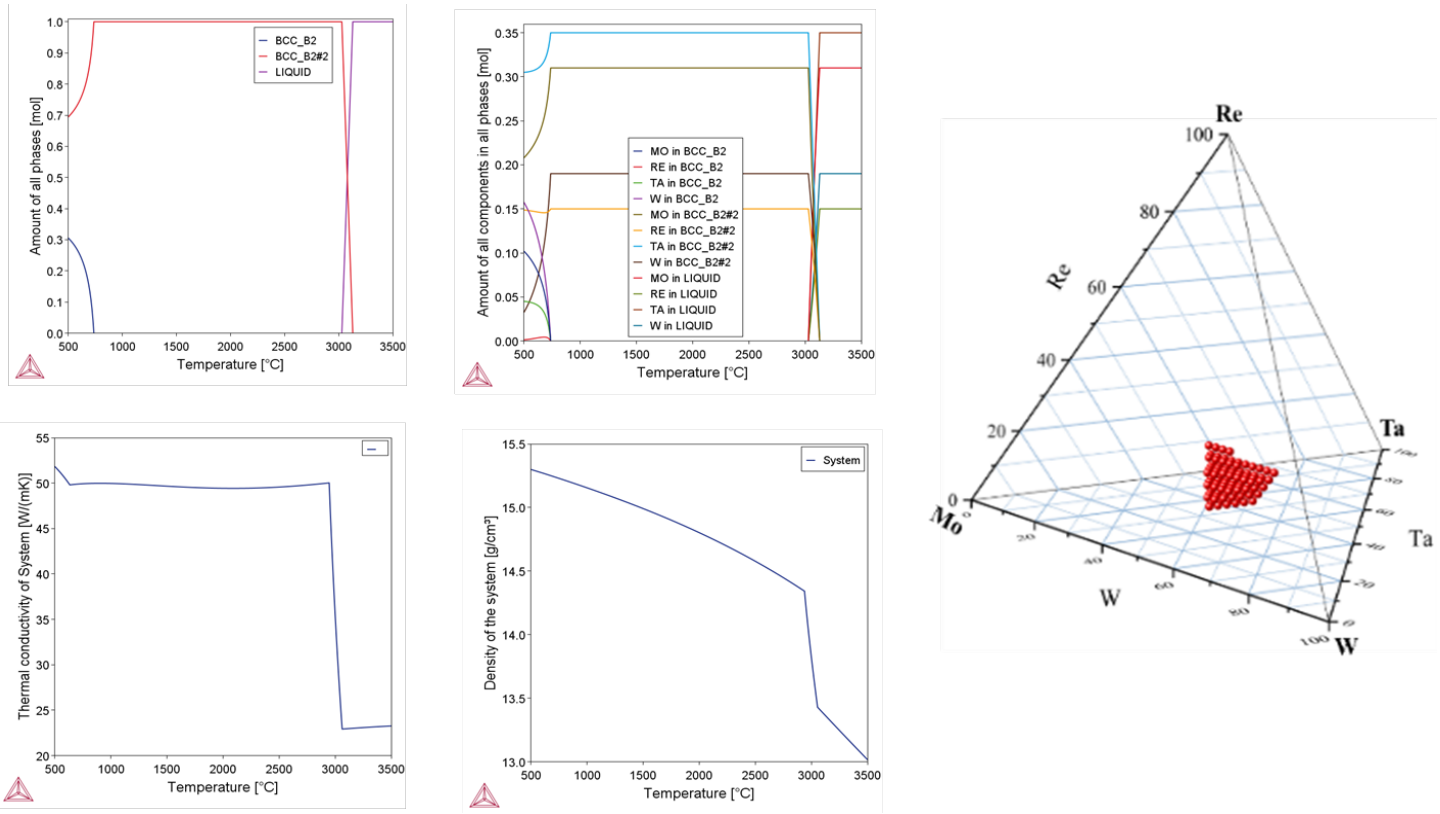

Figure 1. Equilibrium solidification simulation of 19W-15Re-31Mo-35Ta alloy: (a) Amount of equilibrium phases, (b) Elemental distribution in BCC_B2#2 and BCC_B2 phases, (c) Thermal conductivity, (d) Density, and (e) Predicted composition space of W-Re-Ta

Accomplishments

- Thermodynamic simulations of 350 W-Re-Ta-Mo alloys have been completed. Mole fraction of all phases, phase composition, entropy, density, thermal conductivity, and electrical conductivity have been calculated for 350 RMEAs from 500 °C to 3500 °C.
- W-Re-Ta-Mo refractory medium entropy alloy composition space was constructed based on the CALPHAD simulations.
- Developed a high-throughput alloy development process via laser based multi-feeder directed energy deposition process for accelerated alloy discovery.

Team Members

Rajiv Mishra, Nathan Wyeth

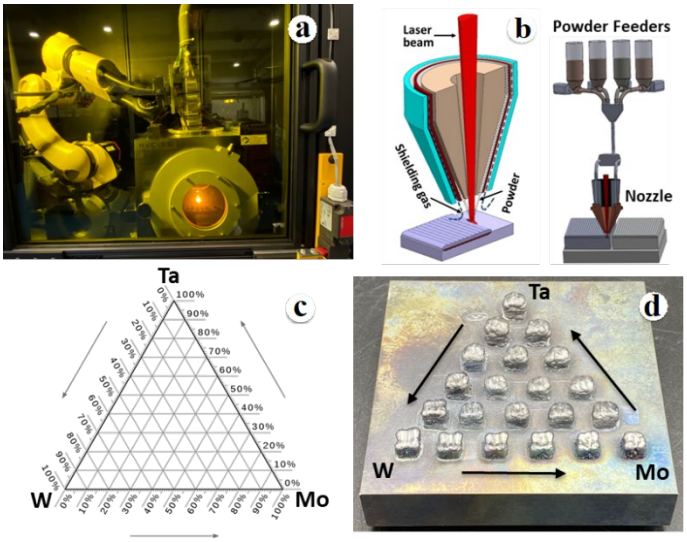

Figure 2. (a) Directed energy deposition (DED) system developed at SRNL, printing W-Mo-Ta alloys, (b) Schematics of the DED process, (c) Schematics of W-Mo-Ta ternary composition space, and (d) As-deposited W-Mo-Ta ternary alloy coupons.

Controlled Equilibrium Catalytic Isotope Exchange (CECIE) - Unlocking new Avenues of Materials Science and Performance

George Larsen

Deuterated materials are desirable, but extremely expensive or non-existent. By harnessing our competency in hydrogen processing, SRNL can disrupt the traditional process and create new avenues of research and applications. The primary goal is to develop a unique national resource for the deuteration of materials and apply it toward research in strategic areas.

Introduction

Deuterated materials, such as polymers, have unique properties compared to normal protiated materials. This is because protium (H) and deuterium (D) have the largest relative mass ratios of any isotopes, which significantly affects kinetics (kinetic isotope effect), and the C-D bond has improved stability compared to the C-H bond. However, deuterated organics are extremely expensive and only available in small quantities, if available at all. This is because traditional methods for deuterated organic syntheses rely on D_2O chemistry to build up larger molecules from precursors and monomers – an expensive and laborious process that is constrained by known chemical pathways.

Catalytic hydrogen isotope exchange is a promising approach to shortcut this traditional process to synthesize new and existing deuterated materials. However, catalytic exchange is a slow, equilibrium-driven process. Thus, most deuterium that enters the reactor passes through unreacted. To make the catalytic process cost-efficient and scalable, the unreacted deuterium needs to be separated from protium and other impurities in the effluent stream and recycled – this is the basis of the controlled equilibrium catalytic isotope exchange (CECIE) process. It is worth noting that these requirements are analogous to those of a deuterium-tritium fusion fuel cycle, and SRNL is recognized as the world leader in developing and deploying hydrogen processing technologies. The goal of this project is to develop unique a national resource at SRNL for the deuteration of materials and apply it toward research in strategic areas: batteries, novel optical materials, fusion energy, polymer recycling, and basic materials science.

Approach

The crux of making CECIE relevant to science and industry is the combination of hydrogen isotope exchange reactions with subsequent hydrogen processing, including impurity removal and isotope separation. The most efficient way to couple these two processes is to create a recirculation loop through the catalytic reactor. This recirculating loop is connected to an impurity trap and an isotope separation system through valves and control volumes. The loop is initially charged with deuterium, which is circulated through the heated catalytic reactor. As hydrogen isotope exchange in the target molecule progresses, the protium level in the loop increases, and the deuterium level correspondingly decreases. The isotope separation system needs to be connected to the recirculation loop in such a manner as to enable dynamic control of the loop protium concentration. With an in-loop binary gas analyzer for monitoring, the valves can be controlled and operated to bleed out protium/deuterium and feed pure deuterium back in from the external and recycled supplies. The isotope separation system is the heart of the hydrogen processing system, and the project will employ SRNL's world-leading Thermal Cycling Absorption Process (TCAP) for this task. Specifically, a micro-TCAP system is being refurbished for the project. To maximize the impact of SRNL's CECIE process, the project will produce several classes of deuterated materials that are currently cost-prohibitive for intensive research. These materials will be investigated internally and through external collaborations for applications in batteries, fusion energy, polymer recycling, and neutron detection.

Accomplishments

- Designed and assembled first of its kind catalytic reactor recirculation loop - integration with the refurbished TCAP will be completed in FY24, according to the project plan (**Figure 1**).
- Produced a multigram batch of deuterated amorphous polypropylene (**Figure 2).**
- Developed a surfactant-based approach to catalytically deuterate new materials, including polyethylene oxide (PEO), which is a material used in many applications, such as Li ion batteries (**Figure 3**).
- Demonstrated a catalytic deuteration approach to a novel silicone-based neutron detection material (**Figure 4**).
- Presented results at TechConnect World conference.

Intellectual Property

- Invention Disclosure – Deuterated Polymers for Battery Separators

Team Members

Tyler Guin, Kori McDonald[*], Collin Malone[*], James Folkert, Chelsea Goetzman[*], Cooper Tillman[a+]

[a]*Clemson University*
[*]*Postdoctoral Researcher*
[+]*Undergraduate Intern*

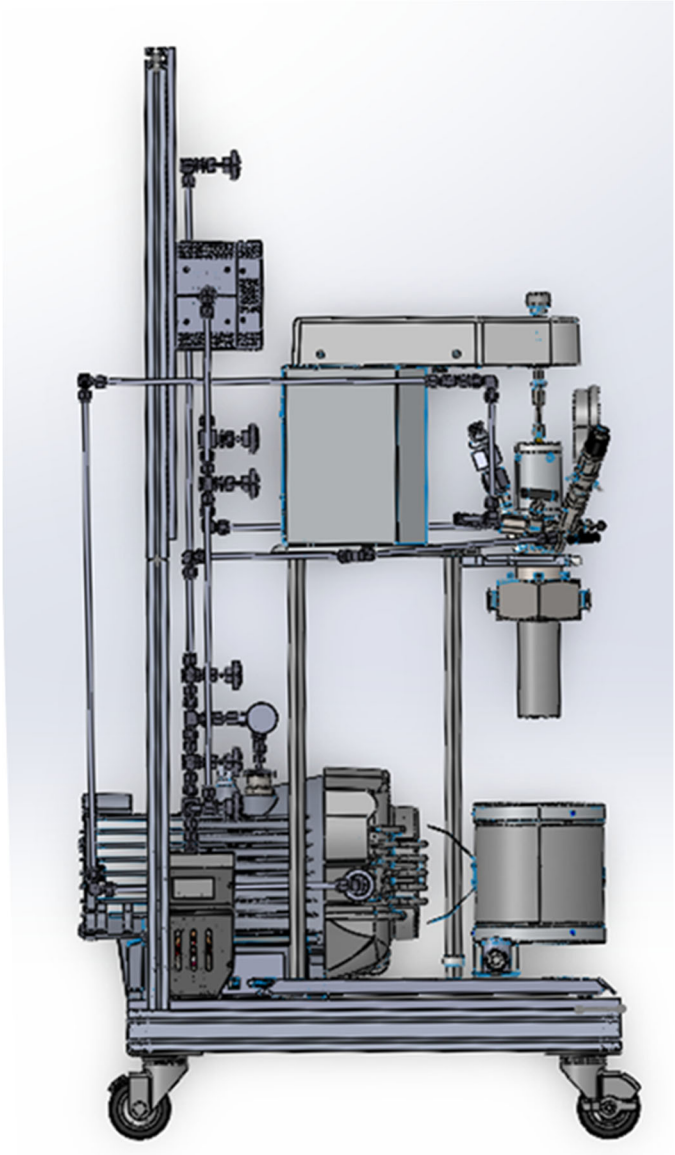

Figure 1. Computer Aided Design (CAD) rendering of the completed catalytic reactor recirculation loop
.

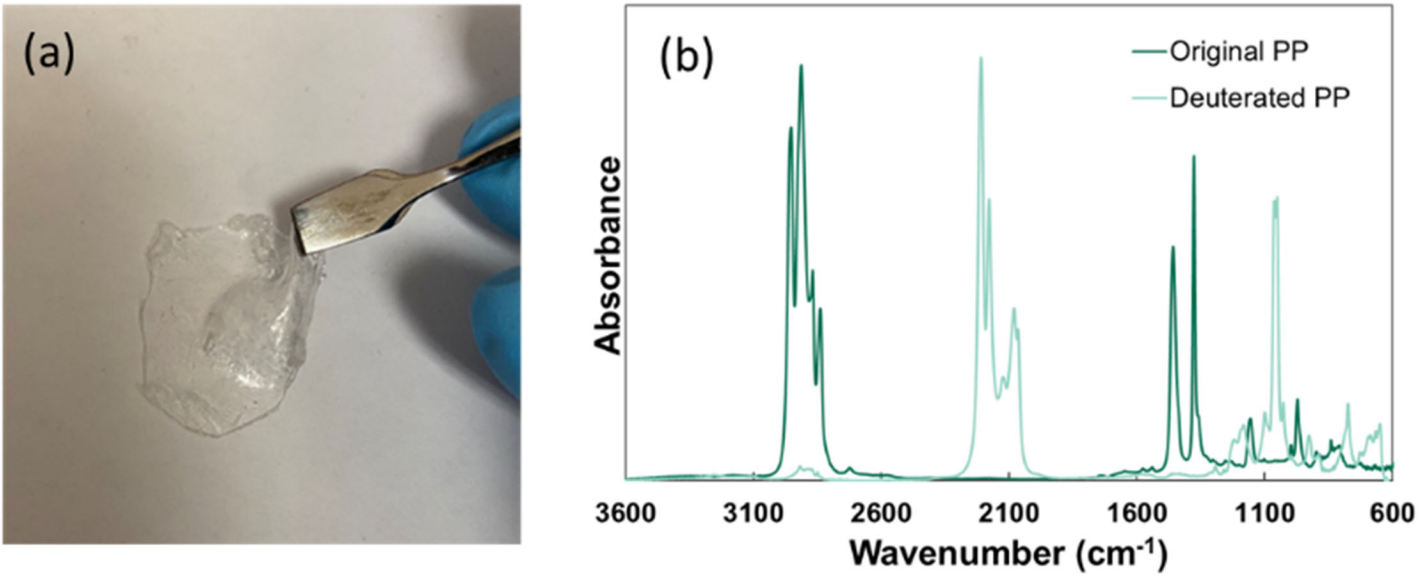

Figure 2. (a) Photograph of deuterated amorphous polypropylene sample, and (b) Fourier transform infrared (FTIR) spectroscopy data showing the shifts in the C-H peaks to the C-D peaks.

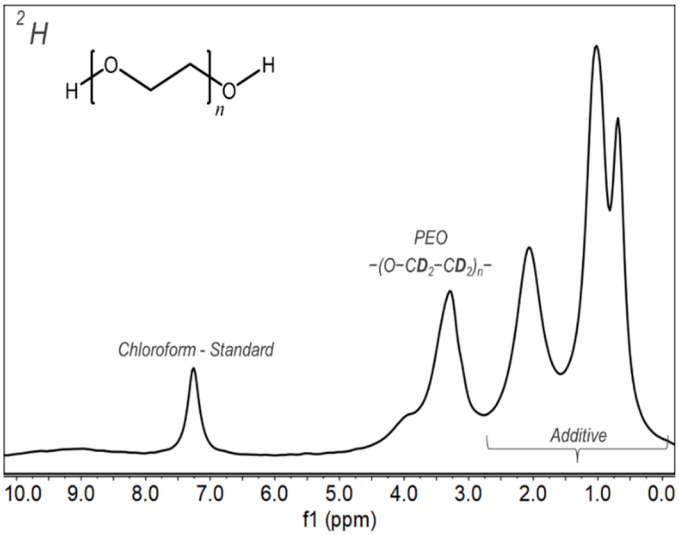

Figure 3: Nuclear magnetic resonance (NMR) data showing the exchange of hydrogen with deuterium in polyethylene oxide (PEO) via surfactant-enhanced catalysis.

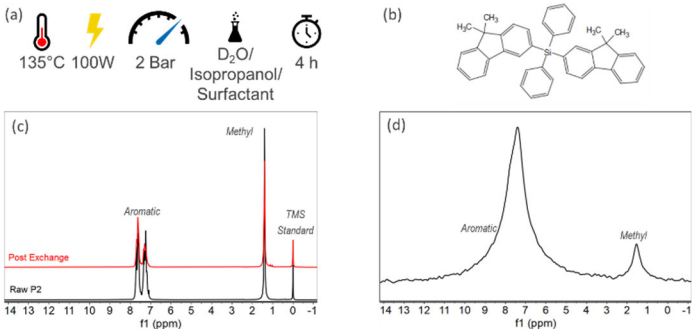

Figure 4. (a) Reaction conditions for deuteration of neutron detection material. (b) Molecular structure of the material. (NMR) data showing the exchange of hydrogen with deuterium for (c) 1H and (d) 2H scans.

Synthesis and Characterization of Critical Material Free Permanent Magnets

Binod Kumar Rai

The objective of this proposal is to investigate and explore the discovery of new Critical Material Free Permanent Magnets (CM-FPM) with high coercivity, remanence, and (BH)max by synthesizing and characterizing candidate materials to mitigate the current critical materials challenges.

Introduction

Permanent magnets are materials that create their own magnetic fields. The strongest known permanent magnets today are referred to as "Rare Earth" magnets. These magnets contain rare earth elements or lanthanides, such as "Neodymium magnets," which contain some neodymium but are are mostly iron. These Neodymium magnets have exceptional field strength and have seen widespread adoption in the automotive, biomedical, weapon, jet, and consumer electronics industries. The dominance of neodymium magnets has created global neodymium shortages and drastic price increases. It is such a threat to our future economy and technology that the United States Government has labeled neodymium as a critical material. Critical materials are any materials used in technology that are subject to supply risks, and for which there are no easy substitutes. Neodymium falls into this class as China dominates the mining industry for these types of heavy and rare earth elements, controlling 61% of global mine production (**Figure 1**). Our work will eliminate the United States high demand for neodymium and, therefore, reduce our dependence on foreign countries by synthesizing and characterizing new Critical Material Free Permanent Magnets.

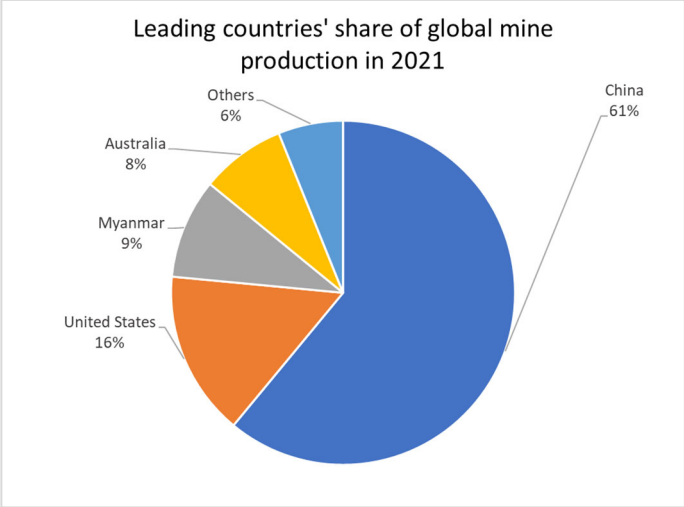

Figure 1. China dominates the rare earth mining industry, controlling nearly 61% of global mine production.

Approach

Identifying and synthesizing materials with high magnetocrystalline anisotropy and remanence is important for achieving improved $(BH)_{max}$ of CM-FPM. High anisotropy and remanence will be achieved by synthesizing materials that incorporate high total-spin transition metal and high spin-orbit coupled elements. High coercivity of materials will be optimized by tuning magnetocrystalline anisotropy, as well as fine particle and grain size, while high remanence will be achieved by aligning the grains along the magnetic easy axis. The second approach of this proposed work is to discover ternary CM-FPM with high coercivity, remanence, and $(BH)_{max}$.

The design and development of new CM-FPM for this project requires magnetic characterization of newly synthesized candidate materials, which is not a current capability of SRNL. To conduct the magnetic characterization, a subcontract with collaborators at the University of South Carolina was successfully executed in June 2023.

Accomplishments

We have one manuscript draft in preparation, four presentations completed in FY23, a summer intern mentored, and Alex Bretaña was awarded the People's Choice at the 2023 SRNL Research Slam. The details are provided below:

- Attended the 2023 Rigaku XRD Workshop at Georgia Tech January 5 and 6.
- Attended the 2023 BSRA University Collaboration Exchange.
- Contributed to writing an invited review article in Report on Progress in Physics (Impact factor: ~18), the manuscript is currently under review.
  - Binod K. Rai, Alex Bretaña, Gregory Morrison, Ryan Greer, Krzysztof Gofryk, Hanno zur Loye, "Magnetism of Binary Actinide Oxides: A Review", Report on Progress on Physics.
- 5%, 10%, and 15% lutetium doped Ce2Fe14B and 10%, 20%, 30%, 40%, and 50% Yttrium doped Ce2Fe14B, as well as Fe-Ni-B candidate materials synthesized and crystal structure characterized.
- Transition temperature of lutetium and yttrium doped samples measured by Differential Scanning Calorimetry (DSC) and Thermogravimetric analysis (TGA) (**Figure 2**).
- Approved subcontract with the University of South Carolina for magnetic characterization.
  - 5%, 10%, and 15% lutetium doped Ce2Fe14B and 10%, 20%, 30%, 40%, and 50% yttrium doped Ce2Fe14B sent and characterized using the University's MPMS (results shown in **Figures 3 and 4**)
- Hosted potential postdoctoral candidate Matt Gordon – spoke about Alex's postdoctoral experience and his recommendation for the Laboratory Director's Postdoctoral Fellowship
  - Since joined the lab as a Laboratory Director's Postdoctoral Fellow.
- Presented at the 2023 SRNL Postdoctoral Poster Session.
- Presented at the 2023 SRNL Intern Poster Session.
- Presented at the L3000 Leadership Program Discussion.
- Presented at the 2023 SRNL Research Slam.
  - Awarded People's Choice Award – selected by the audience.
- Presenting at the 69th Annual American Vacuum Society (AVS) Meeting.
- Presenting at the Up and Atom Event on October 3 presented by the CNTA.

Peer-reviewed Publication

- Alex Bretaña**,** Catherine Housley, Henry Ajo, Benjamin Conner, Patrick Ward, Wenxia Li, Gregory Morrison, Hano zur Loye, Binod K Rai, "Magnetic properties of Lutetium and Yttrium doped $Ce_2Fe_{14}B$ permanent magnets", *(In Drafting 2023)*.

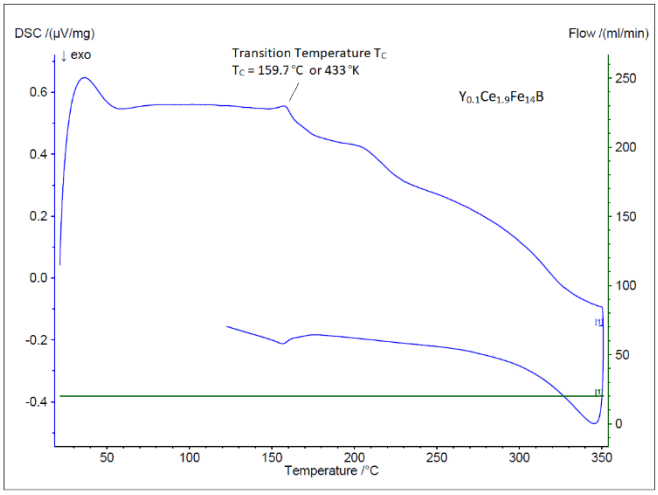

Figure 1. China dominates the rare earth mining industry, controlling nearly 61% of global mine production.

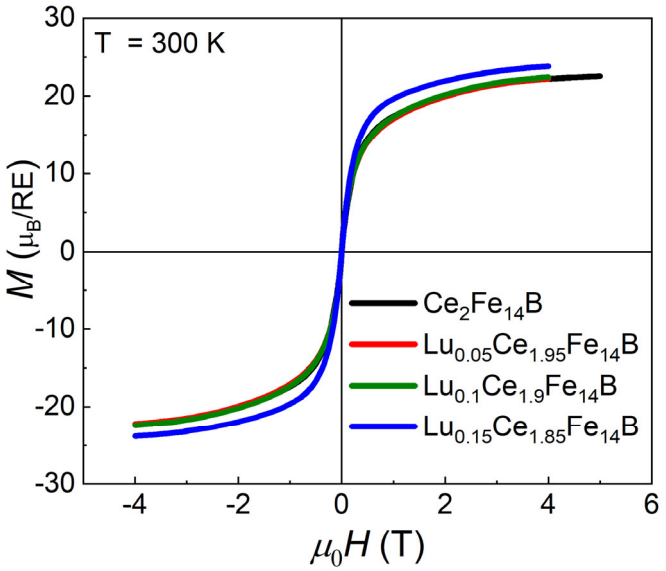

Figure 2. DSC results on $Y_{0.1}Ce_{1.9}Fe_{14}B$ depicting a peak at the transition temperature of $Y_{0.1}Ce_{1.9}Fe_{14}B$.

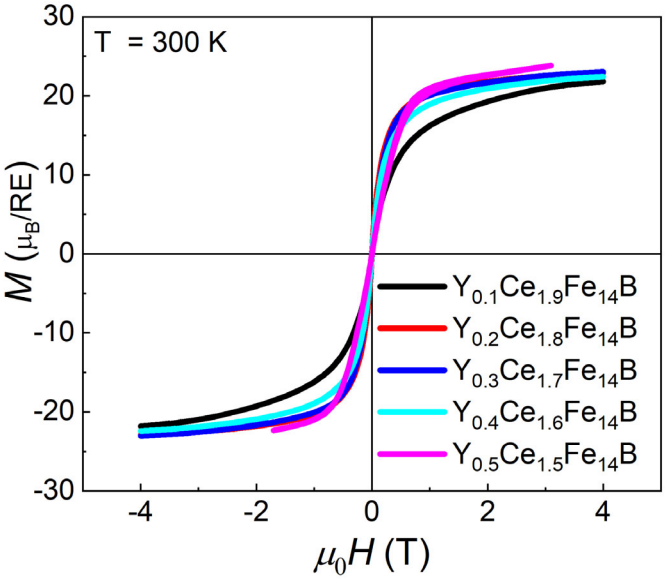

Figure 3. Isothermal magnetization measurements on Lutetium doped $Ce_2Fe_{14}B$ permanent magnet samples completed by our collaborators at the University of South Carolina.

Team Members

Alex Bretana[*], Catherine Housley, Henry Ajo, Chandra Lamberth, Bejamin Conner, Wenxia Li, Patrick Ward, Tucker Koenig[+]

[*]*Laboratory Director's Postdoctoral Research Fellow*
[+]*Undergraduate Intern*

Waste Heat Recovery by 3-D Printed Metal Hydride Thermochemical Energy Storage

Patrick A. Ward

Utilization of waste heat from industrial processes provides a lucrative opportunity for reducing energy consumption and reduction of greenhouse gases. This project aims to develop a novel metal hydride heat pump for the recovery and upgrading of industrial waste heat in a highly efficient manner.

Introduction

Most of the world's energy consumption is ultimately rejected as waste heat due to various inefficiencies across energy conversion and utilization technologies. Therefore, an economically viable solution to recover and utilize waste heat could have an enormous economic and environmental impact. Many industrial processes produce rejected heat from thermal processes, which if captured and utilized, could provide tremendous cost and energy savings. Metal hydride heat pumps provide a promising solution to capture and upgrade thermal energy. In a metal hydride heat pump, thermal energy is used to release hydrogen from one metal hydride bed to a lower enthalpy hydride bed. Heat is added to the second hydride bed to drive hydrogen back into the first hydride bed and the resulting exothermic reaction generates heat. If this reaction can be accelerated by introducing hydrogen at a higher pressure, a temperature upgrading effect can be achieved. This is typically accomplished using a compressor, which is one of the primary inefficiencies in this technology. Our research aim is to develop a methodology to provide a compressor-free heat upgrading effect from a metal hydride heat pump.

Approach

Our team strives to develop an innovative advancement on metal hydride heat pump technology that eliminates the need for a compressor. This, in turn, provides an efficient solution for the recovery and upgrading of industrial waste heat. **Figure 1** illustrates the basic concept utilized in the compressor-free heat pump design.

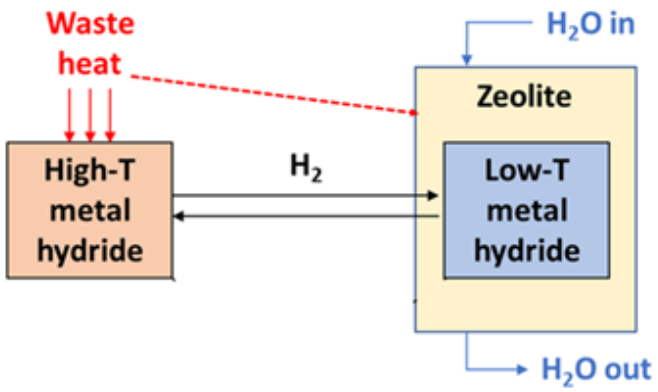

Figure 1. Illustration of novel metal hydride heat pump concept

Since temperature can drive compression in a metal hydride bed, an external bed around the low temperature metal hydride bed is filled with a material that reacts exothermically with water. This allows for the addition of water to drive a temperature spike and resulting compression effect from the low temperature metal hydride bed. Additionally, by increasing the kinetics of the reaction in the high temperature hydride bed, the heat upgrading effect can be enhanced. Therefore, we have systematically evaluated 3D printed lattice structures of various lattice widths, as shown in **Figure 2**, to gain a deeper understanding of hydrogen diffusion's role in the kinetics of hydrogen uptake. To quantitatively access this newly-developed metal hydride heat pump design, our team leverages a computational and experimental approach to develop an optimal material pairing and heat transfer geometries for the overall system. To provide experimental fidelity in the overall technology, a bench-scale test system is being constructed, as illustrated in **Figure 3**, which will provide performance metrics of the newly-developed system design and material pairing choices. Additionally, the influence of 3D printing the high temperature hydrides materials is methodically studied

to determine the influence on hydrogen uptake and thermal transport properties.

Accomplishments

- Designed waste heat upgrading testing rig and began construction.
- Submitted invention disclosure related to novel metal hydride heat pump design.
- Submitted one manuscript for publication.
- Developed Pd doping methodology for increased hydrogen uptake kinetics.
- Prepared and evaluated 3D printed metal hydride samples for diffusion and kinetics studies.
- Produced new alloy formulations for fine-tuning thermodynamic properties of the metal hydride materials.

Peer-reviewed Publication

- Duca, Z.; Ward, P. A.; Sessions, H.; Murph, S. Evaluation of Hydrogen uptake in Powdered and 3D-Printed Ti-6Al-4V. *Journal of Alloys and Compounds*, **2023**, *submitted* (SRNL authors only)

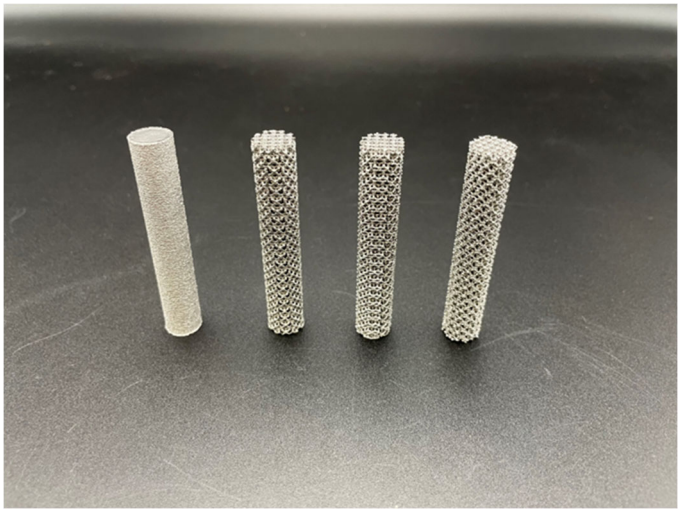

Figure 2. 3D printed samples for diffusion studies

Intellectual Property

- Invention disclosure "Metal Hydrides for Waste Heat Recovery and Upgrading" **SRS-23-028 (BSRA-328-S)** ***submitted***

Team Members

Simona Murph, Bruce Hardy, John Bobbitt

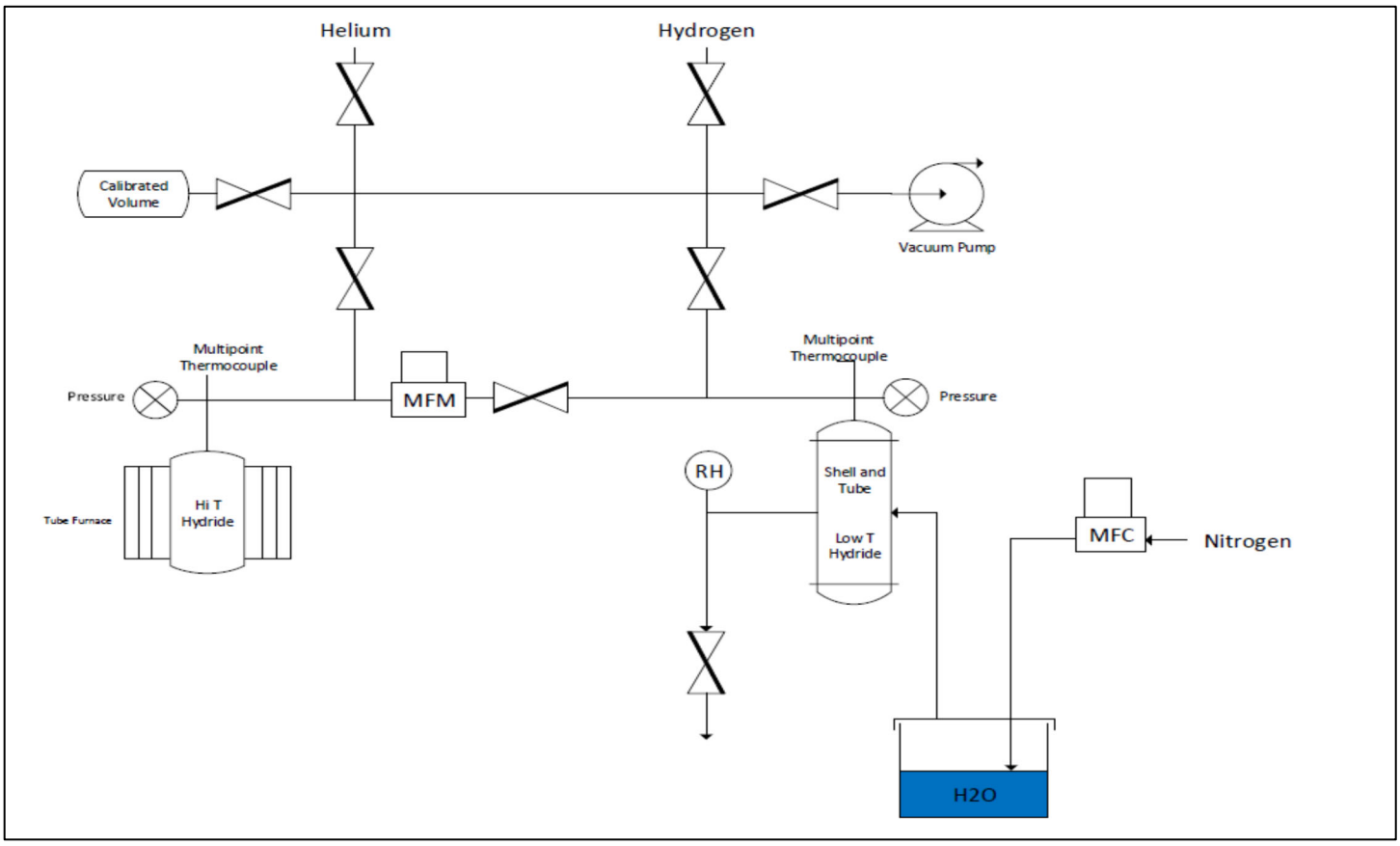

Figure 3. Schematic of waste heat upgrading test rig

Leveraging Magnetic Field Coupling for Extended Charge Separation Lifetimes

Patrick Ward

Photovoltaics operate by light induced generation of negative electrons and positive electron holes, which are separated to generate electricity. These charges can recombine before an electric current can be generated resulting in lower solar power conversion efficiencies. Herein, we study the impact of magnetic fields on mitigating charge recombination to increase photovoltaic efficiencies.

Introduction

Perovskites are well established as one of the most promising candidates for next generation photovoltaics due to their reasonably high solar conversion efficiencies and low-cost production potential. One of the factors that limits photovoltaic efficiencies is the recombination of positive electron holes and negative electrons before they reach their respective electrodes. Our intention is to demonstrate enhancement in the performance of these materials through the application of a magnetic field to induce Lorentz forces on these charged particles. When a moving charged particle is subjected to a magnetic field, that charged particle experiences a force called the Lorentz force according to the following equation:

$$\vec{F} = q(\vec{V} \times \vec{B})$$

The Lorentz force ($\vec{F}$) depends on the strength of the magnetic field ($\vec{B}$), the velocity of the charged particle ($\vec{V}$), and the charge of the particle (q). Since the direction of the applied Lorentz force is the result of the cross product of the velocity, magnetic field strength, and the sign of the charge, positive and negative particles will have an induced Lorentz force in opposite directions. **Figure 1** provides a simplified illustration of the concept. Thus, we developed methodologies to carry out fundamental studies and a deeper understanding of the potential that applied magnetic fields can have on the overall enhancement of photovoltaic efficiencies. Novel variable magnetic field sample cells were constructed to pair with transient absorption spectroscopy measurements to systematically evaluate the influence of magnetic field strength and direction on the lifetimes and degree of charge separated states.

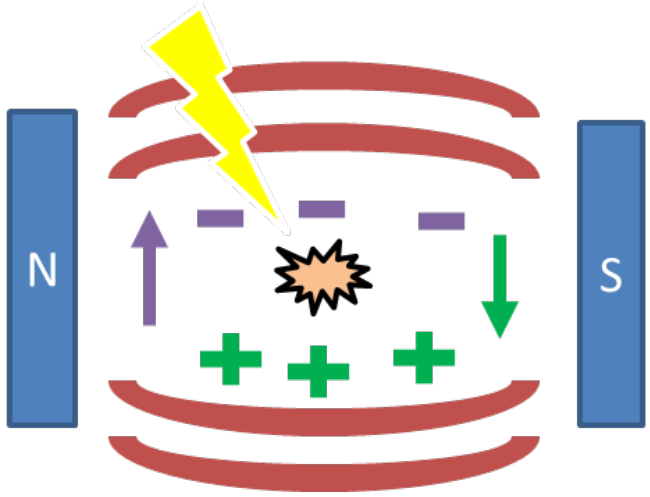

Figure 1. Simplified illustration of Lorentz force on photoinduced charge carriers.

Approach

We aimed to highlight the influence of the magnetic field strength and direction on charge recombination mitigation to increase the solar conversion efficiency of perovskite solar cells. By evaluating various perovskite thin films under fixed illumination and under various external magnetic field strengths and directions, the influential factors and magnitude of performance enhancement can be ascertained. Additionally, slight differences in enhancement between different perovskite solar cells provide insight into the influence of electron transfer pathways and interfaces on the recombination of electrons and electron holes within an applied magnetic field. Furthermore, the alteration of the charge transfer pathway by the influence of an externally applied magnetic field can be evaluated to provide more fundamental insight into these systems. We leveraged a custom built variable magnetic field sample cell in conjunction with UV/visible transient absorption

spectroscopy (UV/Vis TAS) to monitor electronic state absorption differences on the femtosecond time scale. This information provides an understanding of the electron transfer pathways and lifetimes of charge separated states. Methodologies to produce homogenous thickness perovskite thin films on semiconductor thin films were developed and employed to carry out spectroscopic measurements. Full cell $CsPbBr_3$ perovskite photovoltaics were produced and evaluated under magnetic field to demonstrate the enhancement capability of magnetic fields in a practical application. J-V curves of $CsPbBr_3$ solar cells held under an externally applied 5500 gauss magnetic field demonstrated a 7.5% enhancement of the short circuit current, as shown in **Figure 2**.

This observation was further corroborated by current vs. time measurements, shown in **Figure 3**, which demonstrates an increased photocurrent for a $CsPbBr_3$ solar cell under an externally applied 5500 gauss magnetic field.

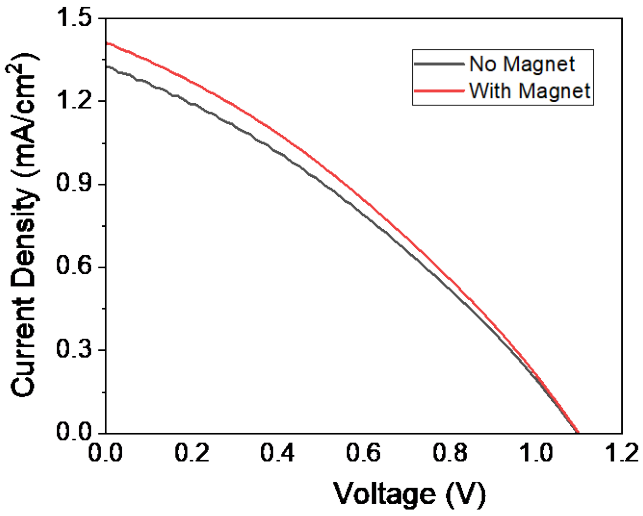

Figure 2. J-V curve of CsPbBr3 perovskite solar cell with magnetic field (5500 gauss) and without magnetic field

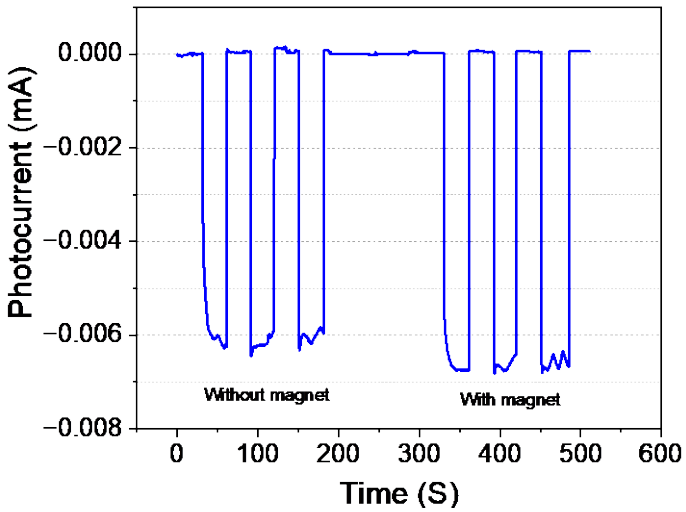

Figure 3. Current vs. time plot of $CsPbBr_3$ perovskite solar cell with magnetic field (5500 gauss) and without magnetic field

Accomplishments

- Demonstrated a 7.5% enhancement of the short circuit current in $CsPbBr_3$ solar cells under a 5500 Gauss magnetic field.
- Submitted 2 manuscripts for publication.
- Filed a patent on a novel photovoltaic device.
- Characterized photovoltaic cell performance in applied variable magnetic fields.

Peer-reviewed Publications

- Hernandez, J.; Robb, A.; Servera,S.; Bedrosian, N.; Gomez, O.; Duca, Z.; Thomas, M. B.; Tamae, D.; Fischhaber, P.; Ward, P. A.; Teprovich, J. A. Synthesis and Characterization of Highly Fluorescent Lawsone Carbon Dots. *ACS Applied Nanomaterials*, **2023**, accepted.
- Robb, A. J.; Duca, Z. A.; White, N.; Woodell, P.; Ward, P. A. Influence of Oxygen on the Optical and Electrical Properties of Magnetron-Sputtered Indium Tin Oxide Thin Films at Ambient Temperature. *Thin Solid Films*, **2023**, accepted.

Intellectual Property

- **Ward, P**. "Systems and Related Methods for Collecting Light Transmitted Through an Architectural Opening" Application No: **18/475,428** Filed: September 27, 2023

Team Members

Zachary Duca[*], Alex Robb[*], Savannah Servera[a+], Nanor Bedrosia[a+], Osma Gomez[a**], Jesus Hernandez[a**]

[a]*California State University Northridge*
[*]*Postdoctoral Researcher*
[**]*Graduate Student*
[+]*Undergraduate Student*

Machine Learning for Weather Forecasting

David Werth

Given its location relative to the coast, sea breezes pass over Savannah River Site (SRS) fairly often, usually overnight, with consequent effects on site meteorology. Similar to our previous work with fog, we have applied machine learning (ML) to the problem of forecasting sea breeze passage on site, using as input 1) meteorological observations, and 2) weather model forecasts. The two ML techniques we applied demonstrated skill, especially when compared to a simple forecast that uses the land-sea temperature gradient as a predictor.

Introduction

During the day, the land surface near the coast will warm faster than the adjacent ocean. In response, a circulation will develop by which the warmer air rises and is replaced by cooler maritime air brought inland. The SRS experiences this phenomenon quite often, though usually at night after the circulation is nearing the end of its diurnal cycle. The sea breeze can affect site operations by lifting air and inducing thunderstorms or causing a sudden wind shift, affecting controlled burns. As with fog, the weather models run at SRS can miss the sea breeze occurrence in their forecasts, either by underestimating daytime surface heating or predicting a too-strong easterly flow.

Increasingly, meteorological forecasting is accomplished with machine learning (ML) - a process by which a computer algorithm analyzes meteorological data and identifies conditions that favor the subsequent occurrence of the targeted event. Given that a large dataset comprising site meteorology, forecasts from computer weather models and a record of sea breeze occurrence at SRS exists, we can apply ML techniques to determine what precursors to the sea breeze at SRS exist.

Two ML techniques – the random forest (RF) and logistic regression – have been trained on meteorological datasets collected from weather towers at the SRS and forecasts from site weather models. The benefit of these two algorithms will be judged based on their performance relative to a 'default' forecast – calling for a nocturnal sea breeze if the forecasted daytime land-sea temperature gradient exceeds a threshold.

Approach

As with fog, we are looking at a daily timescale, with a single prediction each day. The latter is defined with a sea breeze dataset that indicates whether a sea breeze passed over SRS each night. This is based on a combination of satellite images and the detection of a sea breeze signature in site meteorological data.

The predictors comprise both observed meteorological data and model weather forecasts for the period in question. The forecast is assumed to be issued at 1200 UTC (7am EST, 8am EDT) on the previous day (i.e., the forecast is issued on January 1st at 1200 UTC for the occurrence of a sea breeze during the overnight period between January 1 and January 2). For this forecasting application, we elect to maintain the hourly timescale of the input data, allowing for the algorithm to use the change in values with time as a possible indicator of a sea breeze. The input data comprises 3 types: 1) weather forecast model data for 3 models (RAMS, MOS, WRF) at 1-3 hour intervals (depending on the model) for the 0000UTC-1200UTC period concurrent with the forecast period, 2) hourly observations from site towers, both at the surface and at 61 m above ground level for the 0000-1200UTC period prior to the forecast period, and 3) daytime-averaged data from 2 buoys, one in Charleston harbor and the other farther off the coast for the previous day (1200UTC-0000UTC) (**Figure 1**). See **Figure 2** for the time periods used.

The hourly data were prepared one of three ways before serving as input to the ML training, 1) maintenance of the separate hourly values as input, 2) a simple averaging of the data over the time period, and 3) calculating the gradient of the data with time as a model input. As with fog, the data are divided into training and testing subsets.

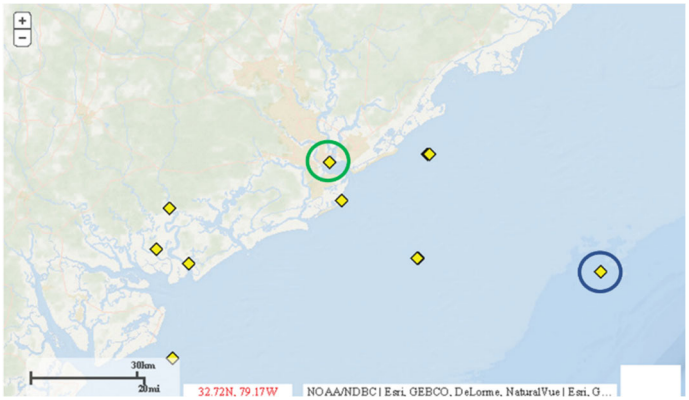

Figure 1. Location of National Data Buoy Center buoys, with the land (green) and sea (blue) buoys used to collect data for input to the ML algorithms.

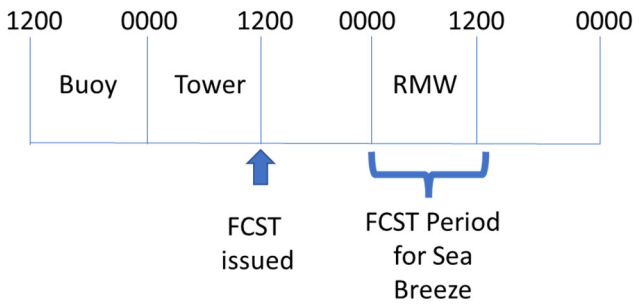

Figure 2. Timeline of the forecast, indicating the time the forecast is assumed to be issued, and the time period during which we hope to predict the sea breeze. Also included are the inputs - the time periods when buoy data (BUOY), meteorological data from site towers (Tower) and the RAMS, MOS, and WRF weather forecast models (RMW) were used as input to the ML algorithms.

The two ML algorithms were then trained and subsequently used to produce testing forecasts. These were scored and compared to a default forecast. For scoring, we apply the equitable threat score (ETS), a metric that rewards true positives (TP) (i.e., a predicted sea breeze occurred), while penalizing false positives (FP) and false negatives (FN) and eliminating the 'hits' expected by guessing randomly (TP_{random}):

$$ETS = \frac{TP - TP_{random}}{TP + FN + FP - TP_{random}}$$

$$TP_{random} = \frac{(TP+FN)(TP+FP)}{TP+TN+FP+FN}$$

The random forest was applied to several versions of the input dataset, and the best results were when the input data were allowed to remain as a sequence of separate values, with no averaging or use of a gradient calculation. The ETS value was approximately 0.35, and the best predictors included the MOS temperature at 0000UTC, the RAMS wind direction at 0300UTC, the observed 61m dewpoint temperature in N-Area at 0000UTC, the RAMS dewpoint temperature at 0000UTC, and the MOS wind direction at 0100UTC.

For the logistic regression, the best results were obtained when, 1) the gradient of the data served as input, and 2) no data from the buoys was used. The ETS was 0.420. The best predictors all came from models – the 0000-1200UTC gradients of the RAMS dewpoint temperature, RAMS wind speed, WRF wind direction, MOS wind direction, and the RAMS PBL. Including the buoy data as input to the ML, either as-is or using it to calculate a land-sea temperature difference to create a new input, tended to reduce the ETS.

The default forecast represents a prediction of the sea breeze if the difference between the RAMS-forecasted temperature at SRS and the off-shore buoy temperature exceeds 5.0°C. For both algorithms, the ETS values are much higher than those obtained using a temperature gradient alone to predict a sea breeze (~0.14).

Accomplishment

- Established that the sea breeze at SRS does have precursors in meteorological observations and forecast models for a 12-hour lead time, and that using hourly observed data and model predictions as input has a benefit.

Team Members

David Werth, Tom Danielson, Elizabeth LaBone, Stephen Noble

Advanced Plasticity Theory and Machine Learning Technology for Determining Burst Strength of High-Pressure Vessels

Xian-Kui Zhu

This project proposed an advanced strength theory, developed exact solutions (or burst models) for defect-free (or corroded) pipes, performed numerous finite element calculations, and created machine learning models from the burst database. The new models predict more accurate burst strength, improve design and operation and, thus, help improve safety and reliability of pressure vessels.

Introduction

Pressure vessels and pipelines, fabricated from various grades of steel and subject to high internal pressure, are the nation's important infrastructure for storage and transportation of hazardous liquids, natural gas, or other fluids for energy systems. Their maximum pressure bearing capability, characterized by burst strength, is critical to structural design, safe operation, and integrity management. Current industry codes or standards were empirically developed from limited experiments on particular steels or a simple strength theory and did not accurately determine the burst strength. This includes ASME Boiler and Pressure Vessel Codes, ASME B31.G, Modified B31.G and RSTRENG® models. However, those codes use either the classical Tresca or von Mises strength theory without considering the plastic flow effect of metals. Thus, significant errors may result utilizing estimation schemes from these codes.

An advanced strength theory is needed for developing a more accurate burst pressure solution with consideration of the plastic flow or strain hardening effect. Alternatively, the plastic flow theory should be used to determine an exact burst pressure solution, but complicated mathematical calculations have to be overcome. In addition to theoretical solutions, elastic-plastic finite element analysis (FEA) may be carried out for a case-by-case investigation or for a parametric study on different pressure vessels or line pipes with and without corrosion defects. With the FEA results, supplemented by existing full-scale burst test data for line pipes, machine learning models can be explored for a wide range of pipe geometries and steel grades using the artificial neural network (ANN) technology.

Approach

This work adopted a technical approach that combined theoretical, numerical, and experimental methods to achieve the project objectives. Full-scale burst test data were collected from literature and archives. An advanced strength theory was developed in terms of the Zhu-Leis yield criterion, and the associated burst solution was obtained for thin and thick-walled pressure vessels. A power series solution (exact solution) of burst pressure was also obtained using the flow theory of plasticity for pressure vessels in power-law hardening steels. On this basis, two corrosion assessment models were developed for thick-wall corroded pipelines. The proposed models were evaluated using full-scale burst test data for thin and thick-walled pipes. To supplement the test database, numerical burst data were calculated using the commercial software ABAQUS from 3D elastic-plastic finite element analyses (FEA, see **Figure 1**) for a well-designed matrix of 360 corroded pipe cases. A wide range of pipeline geometries and steel grades were analyzed with Python and MATLAB codes, which were written to generate the FEA input files and extract/analyze FEA burst pressures from these models (see flowchart in **Figure 2**). Based on a large database containing measured and numerical burst pressures, machine learning models were explored using ANN architectures (see **Figure 3**) for predicting burst strength. Microsoft Excel Solver was used to create ANN models with one or two hidden layers, while MATLAB was utilized to create and optimize ANN architectures with multiple hidden layers using better hyperparameters. Typically, an ANN may have multiple input variables, but only one output variable (e.g., burst pressure). **Figure 4** compares two machine learning predictions with the Zhu-Leis exact burst solution and measured burst data.

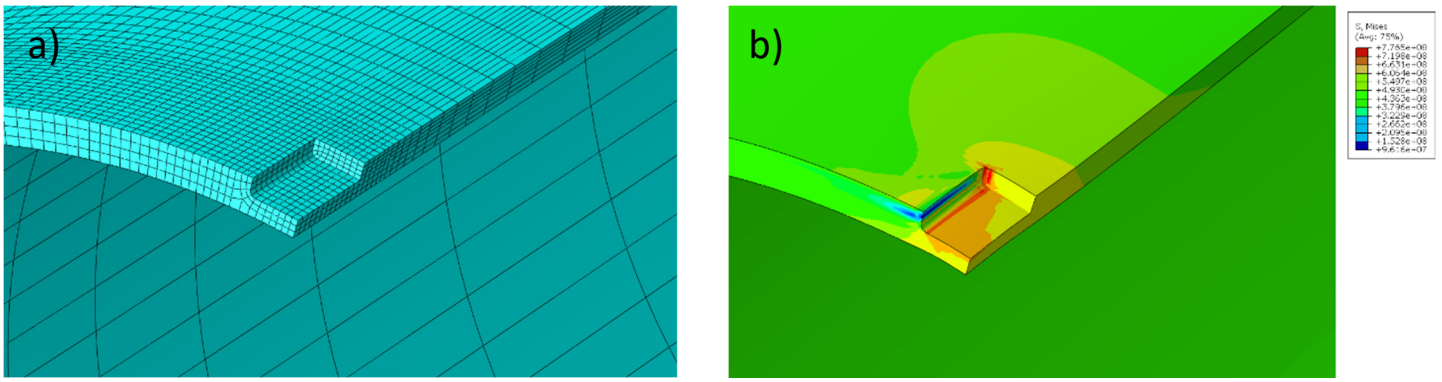

Figure 1. Finite element models of corroded pipes: (a) FEA meshes, and (b) von Mises stress contour.

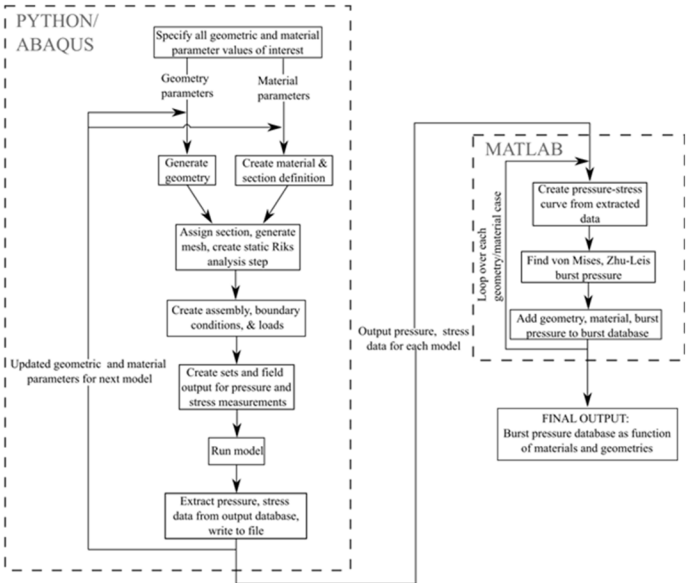

Figure 2. Flowchart of Python and MATLAB codes to generate ABAQUS input files and extract burst pressure data.

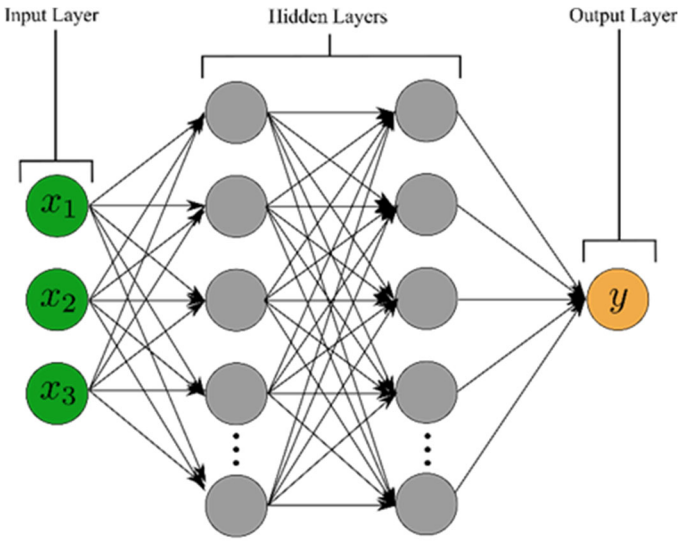

Figure 3. Illustration of a typical artificial neural network model with multiple hidden layers and hidden neurons.

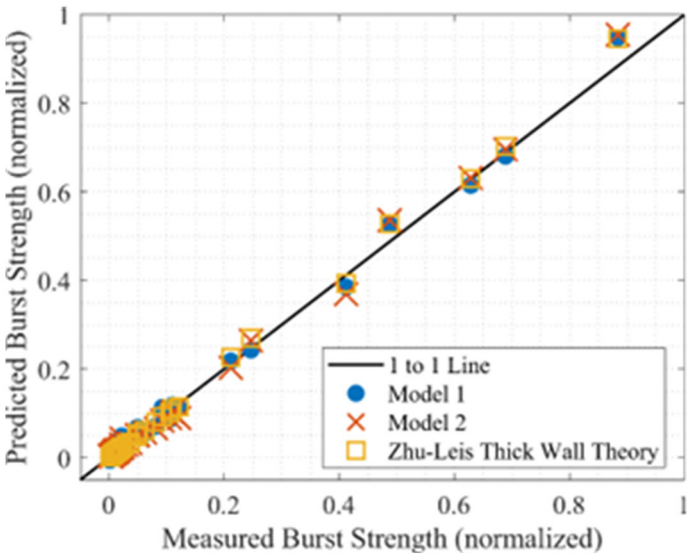

Figure 4. Comparison of machine learning predictions with Zhu-Leis burst solution and measured burst data (Model 1 has 3 input variables and 1 hidden layer with 8 hidden neurons; Model 2 has 3 input variables, two hidden layers with 10 hidden neurons).

Accomplishments

The major accomplishments achieved for this project are:

- Collected a large database of more than 400 burst pressure tests for a wide range of pressure vessels from small diameter tubes to large diameter carbon steel pipes.
- Developed an advanced strength theory and determined a more accurate burst strength solution for both thin and thick-walled pressure vessels. This new theory fills the technical gap in mechanics.
- Obtained a power series solution (exact solution) for burst strength of thick-walled pressure vessels in a power-law hardening steel using the flow theory of plasticity (see **Figure 5**). This exact burst solution fills the technical gap left by Svensson (1958) for predicting thick-wall burst pressure.
- Extended the exact solution to develop two corrosion models for predicting more accurate burst strength of

thin and thick-walled pipelines with corrosion defects for various steels (see **Figure 6**).

- Developed a Python script-based FEA code and performed the FEA calculations for a matrix of 360 corrosion defect cases in thin and thick-walled pipes for various pipeline steels. The FEA results will be compared with those predicted by the thin-wall models and the proposed thick-wall models.
- Developed machine learning models for burst strength of large-diameter pipelines using the Microsoft Excel Solver. The machine learning models improve the existing analytical models.

The machine learning models of burst strength were optimized using MATLAB with combined test and FEA database for a variety of pipelines. Compared to a regression tool, MATLAB facilitates the development of an ANN prediction model for a large database with multiple variables.

- Published seven journal papers and eight conference papers in FY23.

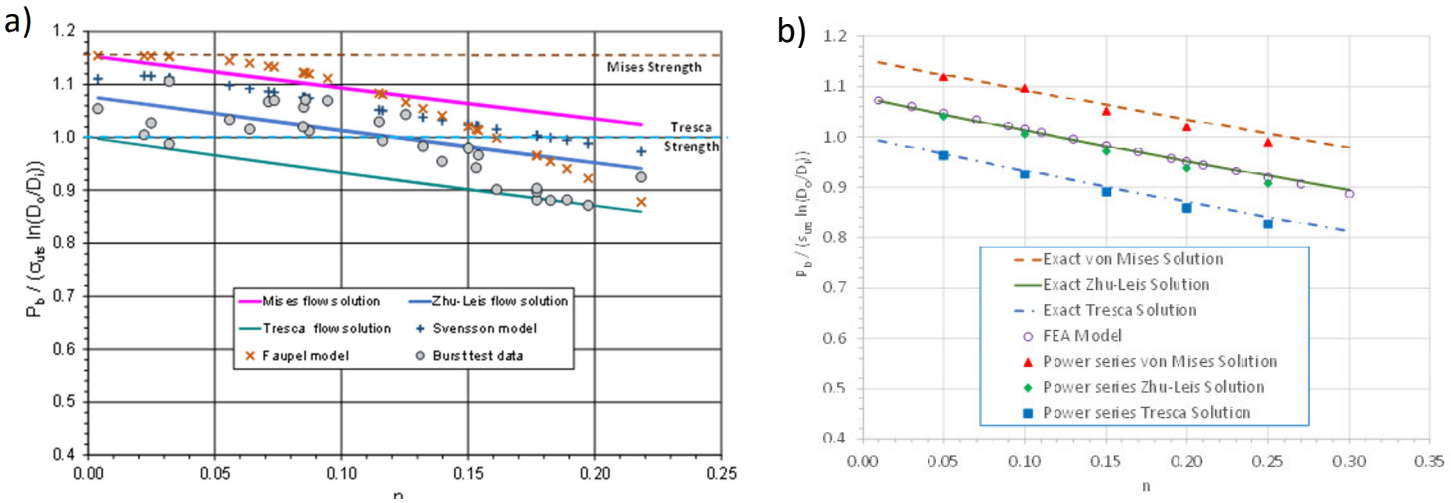

Figure 5. Variations of power series solutions (exact solutions) for burst pressure and comparisons with (a) FEA model, and (b) full-scale burst data for very thick-walled tubes.

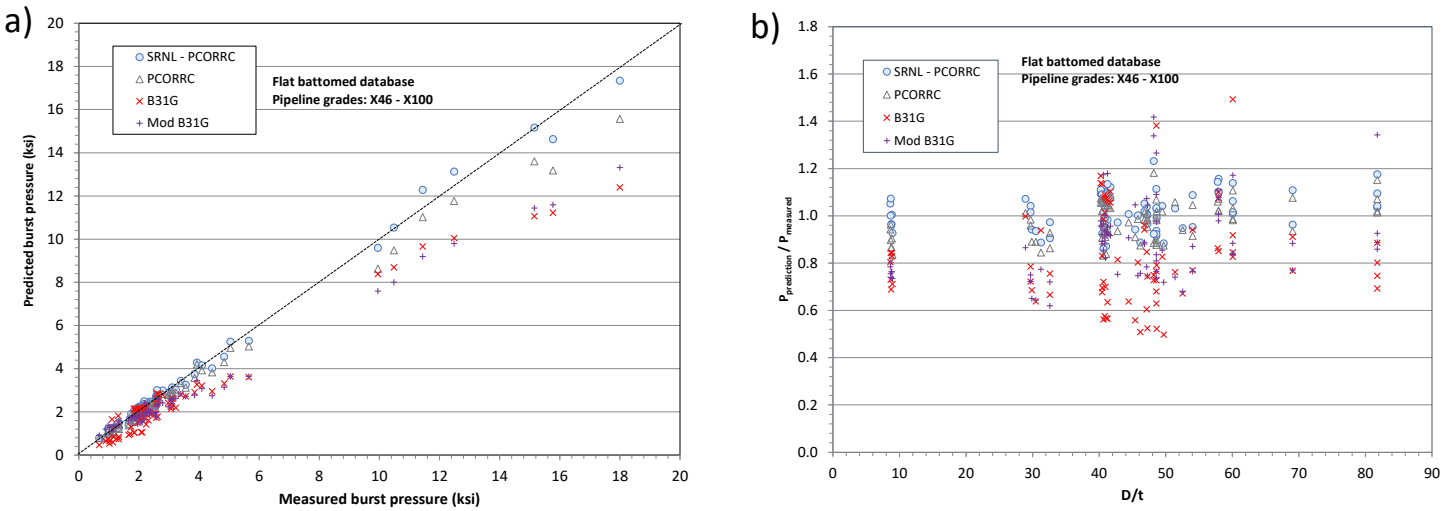

Figure 6. Comparison of the proposed model predictions with burst test data for corroded line pipes in various grades from X46 to X100.

Peer-reviewed Publications

The peer-reviewed publications for this work include journal papers and conference papers. For all these published papers, SRNL is the primary organization.

- Zhu X.-K., Wiersma B., Sindelar R., Johnson W.R. Exact solutions of burst pressure for thick-walled cylinders in power-law strain hardening steels, *International Journal of Pressure Vessels and Piping* **2023**, *206*: 105053.
- Zhu X.-K. Exact solution of burst pressure for thick-walled pipes using the flow theory of plasticity, *International Journal of Mechanical Science* **2023**, *259*, 108582.
- Zhu X.-K. A verification study of fatigue-based methods in API RP 1183 for estimating fatigue life of pipeline dents, *International Journal of Pressure Vessels and Piping* **2023**, *205*, 104969.
- Johnson W.R., Zhu X.-K., Sindelar R., Wiersma B. A parametric finite element study for determining burst strength of thin and thick-walled pressure vessels, *International Journal of Pressure Vessels and Piping* **2023**, *204*, 104968.
- Zhu X.-K., Johnson W.R., Sindelar R., Wiersma B. Burst Pressure Solutions of Thin and Thick-Walled Cylindrical Vessels, *Journal of Pressure Vessel Technology* **2023**, *145*(4), 044202.
- Zhu X.-K. Recent Advances in Corrosion Assessment Models for Buried Transmission Pipelines, MDPI *Journal CivilEng* **2023**, *4*(2), 391-415.
- Zhu X.-K., Johnson W.R., Sindelar R., Wiersma B. Artificial neural network models of burst strength for thin-wall pipelines, *Journal of Pipeline Science and Engineering* **2022**, *2*(4), 100090.
- Zhu X.-K., Wiersma B., Johnson W.R., Sindelar R. Corrosion assessment models for predicting remaining strength of corroded thick-walled pipelines, *Proceedings of the ASME 2023 Pressure Vessels and Piping Conference*, July 16-21, 2023, Atlanta, Georgia, USA. PVP2023-106911.
- Zhu X.-K., Zhu J.B., Duncan A.J., Data-driven stress intensity factor solutions for axial outside surface cracks in thin-walled cylinders, *Proceedings of the ASME 2023 Pressure Vessels and Piping Conference*, July 16-21, 2023, Atlanta, Georgia, USA. PVP2023-106471.
- Zhu X.-K. CMOD compliance solution determined by stress intensity factor for single edge notched tension specimens in end-clamped conditions, *Proceedings of the ASME 2023 Pressure Vessels and Piping Conference*, July 16-21, 2023, Atlanta, Georgia, USA. PVP2023-106906.
- Johnson W.R., Zhu X.-K., Sindelar R., Wiersma B. Artificial neural networks for predicting burst strength of thick and thin-walled pressure vessels, *Proceedings of the ASME 2023 Pressure Vessels and Piping Conference*, July 16-21, 2023, Atlanta, Georgia, USA. PVP2023-106471.
- Johnson W.R., Zhu X.-K., Sindelar R., Wiersma B. Determining burst strength of thin and thick-walled pressure vessels through parametric finite element analysis, *Proceedings of the ASME 2023 Pressure Vessels and Piping Conference*, July 16-21, 2023, Atlanta, Georgia, USA. PVP2023-106637.
- Zhu X.-K. Comparison of fatigue models in API 1183 for predicting fatigue life of pipeline dents, *Proceedings of the ASME 2023 Pressure Vessels and Piping Conference*, July 16-21, 2023, Atlanta, Georgia, USA. PVP2023-102043.
- Zhu X.-K. Constant CTOA determination for stable ductile crack growth and its application to running fracture control for gas transmission pipeline, *The 15th International Conference on Fracture (ICF15)*, June 11-16, 2023, Atlanta, GA, USA.
- Zhu X.-K. Analytical solution of CMOD compliance for single edge notched tension specimens in end-clamped conditions, *The 15th International Conference on Fracture (ICF15)*, June 11-16, 2023, Atlanta, GA, USA.

Team Members

William Johnson*, Bruce Wiersma, Robert Sindelar,

*Postdoctoral Researcher

FY23 PROJECTS

CORE COMPETENCY:

Securing connected control systems and associated data

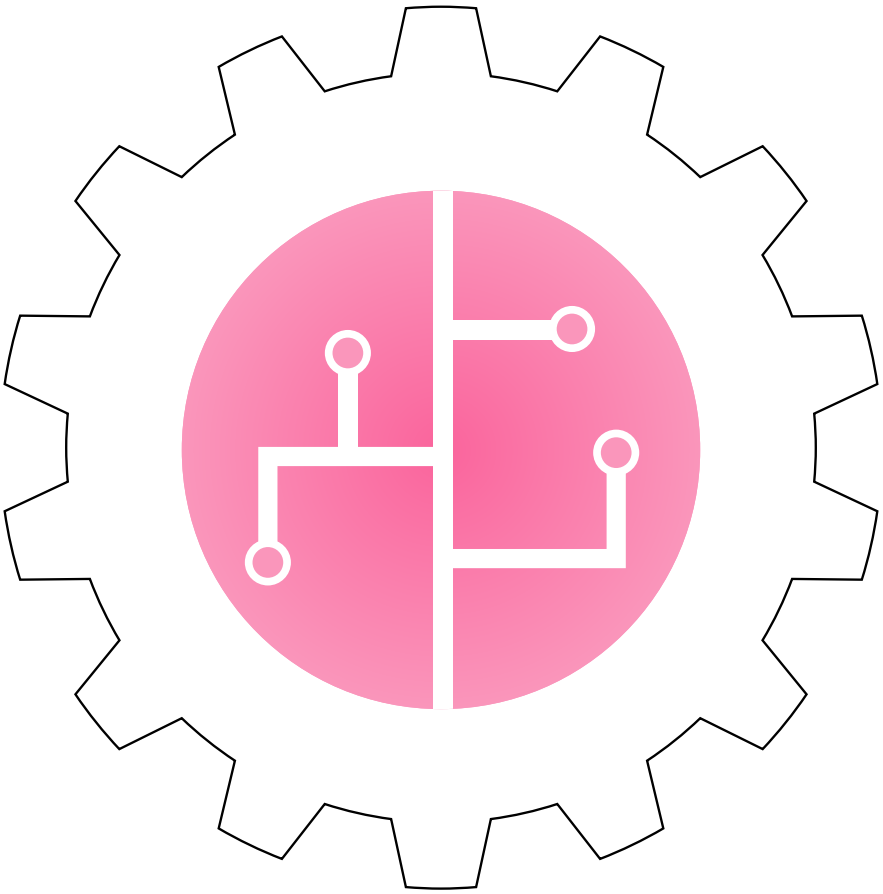

Theoretical Evaluation of Point Defect Induced Charge Trapping Mechanisms in CdZnTe and CdZnTeSe

Jonathon N. Baker

Cadmium zinc telluride selenide is a promising next-generation material for room temperature semiconductor radiation detectors. This research uses advanced computational materials science to deeply understand performance limiting factors of this system, and their relationship with processing. In turn, this will enable a deep level of materials engineering on this system.

Introduction

Techniques for accurately calculating the concentrations and ionization states of point defects in compound semiconductors have advanced rapidly in the past 10 years. However, these methods have yet to be applied in any kind of systematic way to materials of interest for radiation detection, due to difficulties in curating the large scale of hybrid exchange-correlation functional Density Functional Theory (DFT) data required to inform the necessary thermodynamics calculations. Additionally, the already extreme computational expense of performing these types of simulations for line compound materials is exponentially increased when considering alloys.

Simultaneously, substantial improvements have been made to the CdZnTe (CZT) material system by adding selenium, especially in terms of crystal quality. These improvements and work to overcome fundamental hurdles facing CZT (e.g., substantial reduction of large amounts of sub-grain boundary networks and tellurium inclusions, and issues controlling alloy composition) have culminated in the development of CdZnTeSe (CZTS). However, point defect derived trap states and their relation to processing remain, at best, poorly understood. This research seeks to systematically apply the advances in computational techniques for studying point defects to current state of the art methods for producing CZT and CZTS. This will fill the void of information on defect chemistry in CZTS while also allowing for very detailed analysis of particular defects of interest and is expected to advance both defect science in CZT and CZTS, and computational science for the study of point defects.

Approach

Hybrid exchange-correlation DFT calculations (an advanced, high-fidelity method of treating electron self-interaction in density functional theory) were performed for a large number of native and selenium-containing defects and defect complexes in ZnTe and CdTe, for use in projecting defect properties into lightly Se-doped CZT alloy. Alongside this effort, a thermodynamic model was derived for Traveling Heater Method growth of CZT and CZTS. The full set of point defect calculations and the thermodynamics model are taken together to calculate defect chemistry versus various processing and doping parameters via statistical mechanics methods. Vibrational properties of high population defects from these models were then calculated and fed back to refine the statistical mechanics calculations. Additionally, special quasi-random structure (SQS) simulations were performed on various CZTS compositions to study alloy disorder effects versus composition.

All DFT calculations were performed using VASP 6. The HSE06 exchange-correlation functional was used for defect calculations, bandstructure calculations, and thermodynamic ground state reference calculations, while the PBE exchange-correlation functional was used for defect vibrational property calculations and for SQS simulations. Vibrational calculations were post-processed using the Asphalt Minimal Phonon Library module, while data management and statistical mechanics analysis were enabled by the Asphalt Database and Point Defects Virtual Workbench modules. Initial preparation of SQS supercells was performed with the AT-AT Monte Carlo SQS module.

Together, these approaches are used to study the defect chemistry and property changes of CdTe, ZnTe, and CdZnTe with selenium concentrations varying between light doping and light alloying.

Accomplishments

- BLAST package was modified to add affine transformation mapping functionality, to enable exploration of nano-texturing.
- Vibrational properties of all high concentration native and selenium related point defects in CdTe and ZnTe were completed this FY (see **figure 1** below for formation energy diagrams and in-gap state movement).
- High priority impurity defect simulations and their associated vibrational simulations were completed this FY.
- Work is partially complete, and ready to continue when funding is available, on tuning the multi-polation scheme for projection of end-member datasets into alloy composition.
- Defect chemistry of THM-grown ZnTe and CdTe has been analyzed as a function of selenium content, using newly developed, much more sophisticated treatment of the THM melt charge environment (see **figure 2**, below for how different melt charge parameters affect the resulting defect and charge carrier concentrations).
- A manuscript documenting the defect chemistry of selenium doped ZnTe was published.
- A manuscript documenting the effects of selenium alloying on Cd0.9Zn0.1Te host matrix lattice parameter variations and associated HR-XRD data was published and chosen as a featured article.
- Manuscripts documenting the interaction of common donor dopants in CdTe with selenium doping/light selenium alloying, and defect chemistry of selenium doped $Cd_{0.9}Zn_{0.1}Te$ are in preparation.
- A manuscript discussing the effects of selenium alloying on $Cd_{0.9}Zn_{0.1}Te$ host matrix atomic spacing variation is currently being prepared.

Peer-reviewed Publications

- Roy, U.N.; Baker, J.N.; Camarda, G.S.; Cui, Y.; Yang, G.; James, R.B.; Evaluation of crystalline quality of traveling heater method (THM) grown $Cd_{0.9}Zn_{0.1}Te_{0.98}Se_{0.02}$ crystals. *Appl. Phys. Lett.* **2022**, *120*, 242103. https://doi.org/10.1063/5.0093255.
- Baker, J.N.; Roy, U.N.; Effects of Selenium Doping in Zinc Telluride from First Principles. *J. Phys. Chem. C* **2022**, *126(50), 21348.*

Intellectual Property

- Copyright paperwork approved by DOE to assert copyright for BLAST package (Bond Length Analysis and Statistics Tool)

Team Member

Utpal Roy

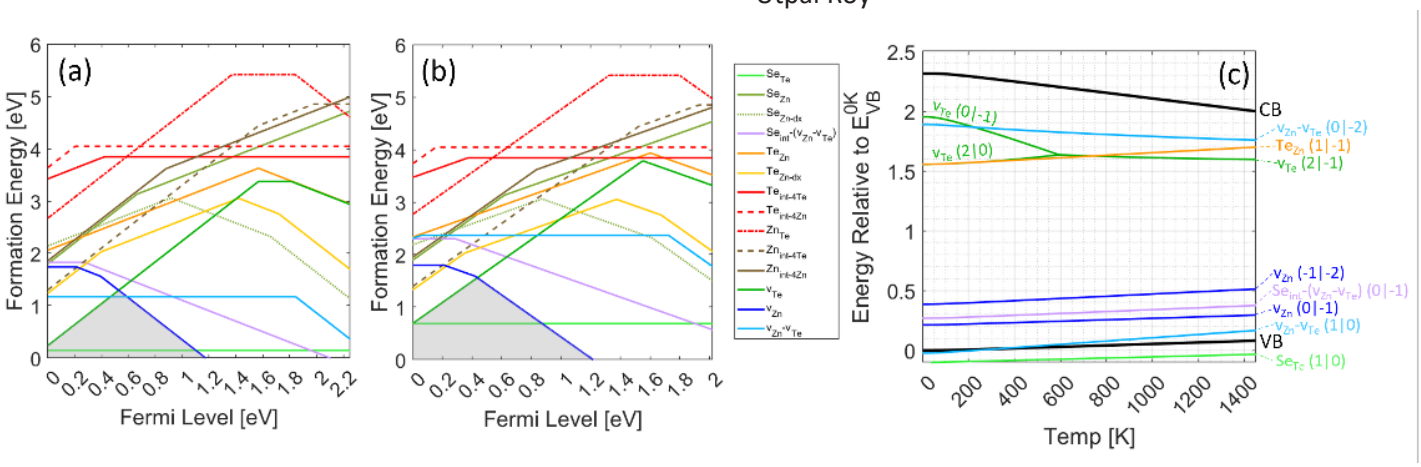

Figure 1: (Figure and caption are a pre-publication version of Fig 1. of *J. Phys. Chem. C* **2022**, *126(50)*, 242103, listed in Publications section above) (a,b) Formation Energies of simulated point defects at room temperature (a) and 800C (b), including band edge movement and vibrational energy contributions [for starred defects in table 1]; selenium defects are shown for a concentration of Se=10^{19} cm^{-3}. (c) In-gap state levels of simulated point defects, and their changes with temperature [for starred defects in table 1].

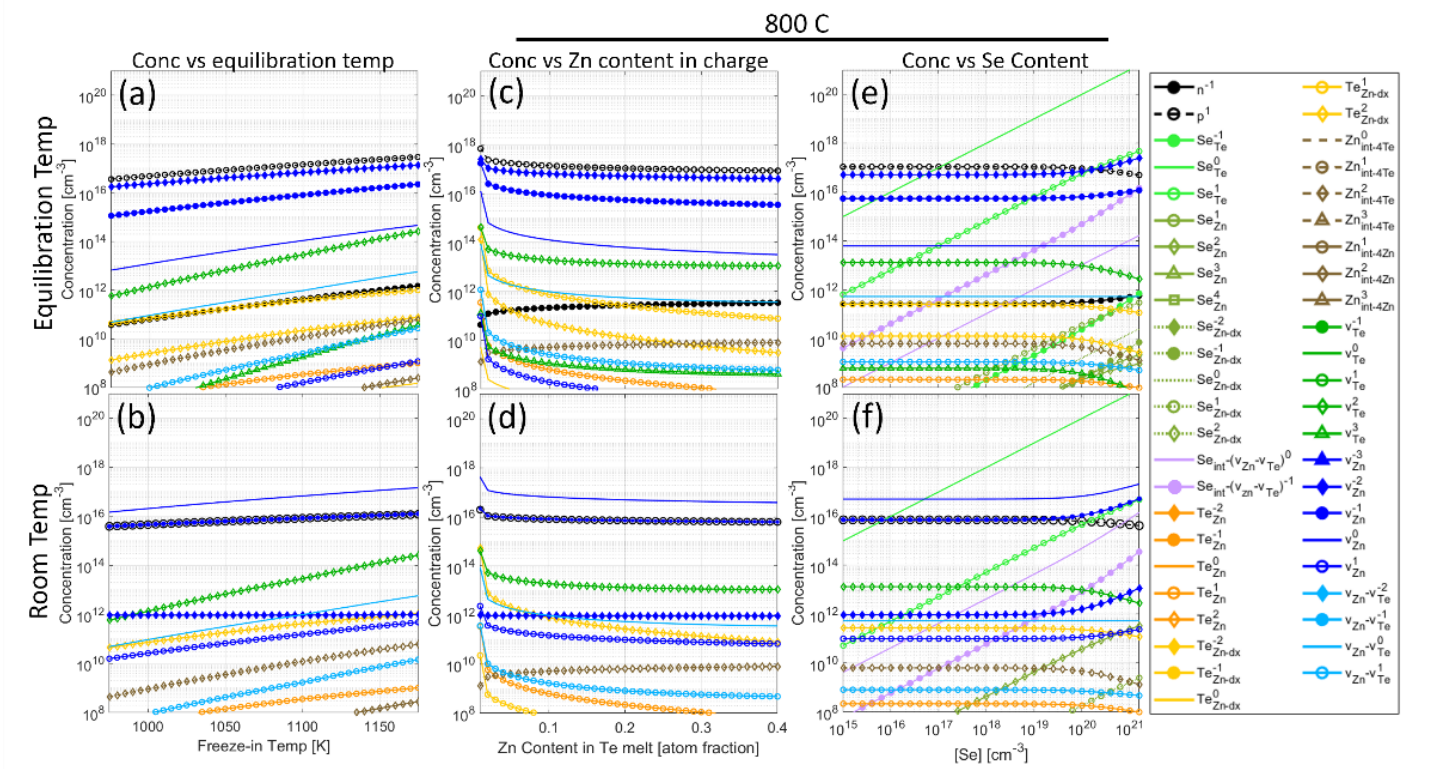

Figure 2: (Figure and caption are a pre-publication version of Fig 2. of *J. Phys. Chem. C* **2022**, *126(50)*, 242103, listed in Publications section above) : High (top: a, c, e) and low (bottom: b, d, f) temperature defect (colored lines) and charge carrier (black lines) concentrations predicted for ZnTe quenched from (a,b) a 20 at.% Zn tellurium melt at increasing freeze-in temperature, (c,d) a tellurium melt with increasing amounts of dissolved zinc content, (e,f) a 20 at.% Zn tellurium melt with increasing selenium content, up to about 3 at%. Defects are color coded by type, with the marker indicating the charge state (see legend to right).

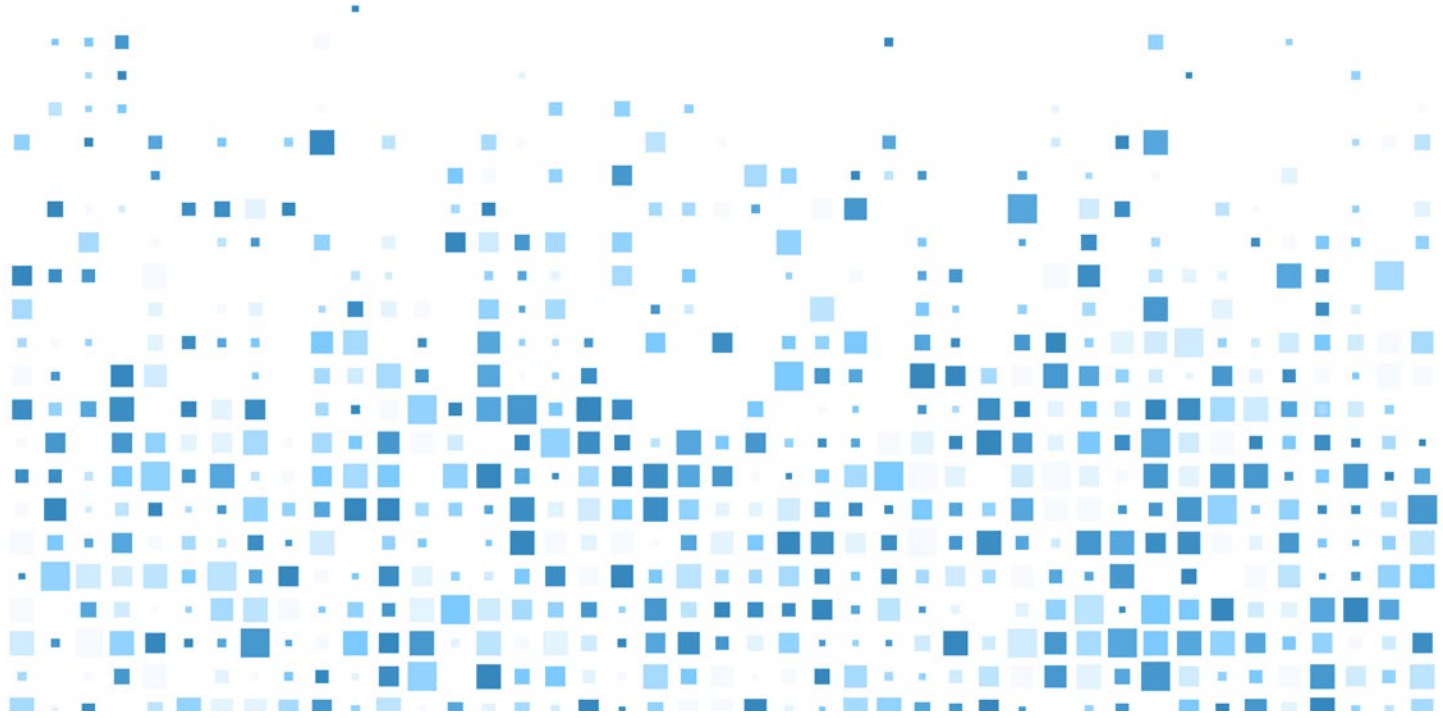

Grid-Forming Inverter Network Cyber Attack Intrusion Prevention and Localization System

Lindsay Roy and Klaehn Burkes

This project was focused on how to secure renewable energy resources for utility companies, through security information and event management platforms tuned specifically for the electric grid. The project developed a virtual electrical grid, utility cybersecurity monitoring system, and malicious activity to secure renewable energy resources.

Introduction

Over the last few years, there has been a large increase in renewable-energy-powered inverter-based resources (IBRs) such as solar plants, wind turbines and battery storage integrated into the bulk power system. This paradigm shift from a dispatchable power flow network (i.e., large power plants) to a variable, de-centralized system utilizing IBRs requires innovative cybersecurity solutions. This shift away from non-renewable-based power generation has resulted in the deployment of millions of power-electronic devices (inverters) onto the grid that are a mixed-control type between local inverter control and centralized Control Center over network-based connections. Distributed IBRs have been demonstrated to be exceptionally vulnerable to network-based attacks, requiring minimally sophisticated cyber-attack frameworks to inflict system shutdown, cause instability, and physically damage power system components. To address this issue, the proposed cyber defence solution would employ highly aggressive informational technology (IT) in an operational technology (OT) network, while also maintaining grid stability and compensating for any power system disturbances through control algorithm swapping. If proven, it will provide a cyber security solution that improves the robustness of a distributed electrical power generation system that is exceptionally vulnerable, while also maintaining grid stability. This research will be widely applicable to current and future implementations of IBRs and their associated control networks, which is quickly becoming the primary source of energy production on the grid.

Approach

SRNL has built a lab that emulates the OT network from Purdue level 4 to 0 of an electric utility company, which was designed for performing vulnerability assessments of power system devices and their communication networks. It is becoming crucial to be able to detect, identify, and halt attacks performed on remote distributed, controlled facilities such as solar facilities, but also maintaining grid stability while thwarting the cyber intrusion. Attacks on the communication networks of aggregated solar controllers would cause instability within the power grid, localized to that inverter mesh network. To this extent, a complete hardware-interfaced digital twin of a distributed grid-forming inverter command and control network will be formed. To do this, a pre-existing co-simulation network between SRNL and University of South Carolina (UofSC) will be upgraded and expanded using power system simulators between SRNL and BSRA partners. This co-simulation network will consist of real-time power system simulators connected via VPN IPsec tunnels, as shown in **Figure 1**. Further, the control system software acting as distributed control system (DCS) or Supervisory control and data acquisition systems (SCADA) will be connected via the VPN and communicate through traditional OT protocols.

This network will ensure accurate depictions of realistic network latency, congestion, and traffic of distributed grid-edge inverter-based devices, creating a critical infrastructure control network that has realistic network characteristics. This will emulate the investor owned and utility operated interconnection of IBRs to allow for independent cybersecurity controls for the utility that don't have to be maintained by the investor. Further, by connecting real-time power system simulators, the size and scale of the simulated grids is also effectively multiplied, combining controller and hardware-in-the-

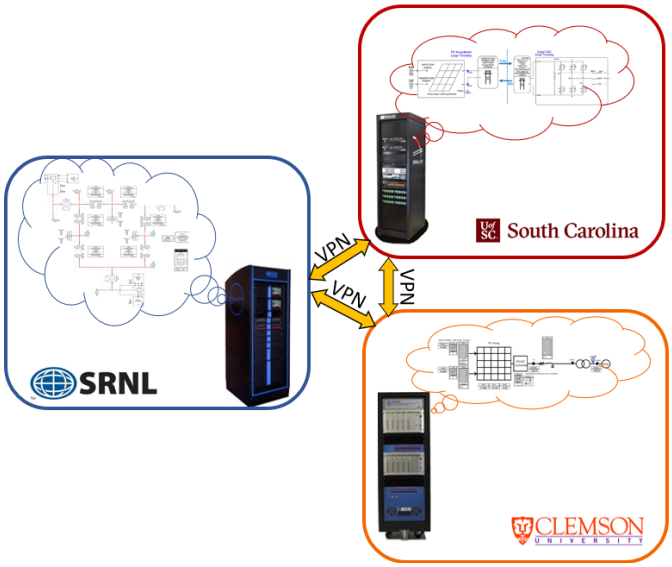

Figure 1. Co-Simulation Network of Power System Simulators

loop (HIL) capabilities into one cohesive network. The software to be used to interface each of the power system simulators is the VILLAS framework, which is an open-source toolset developed by personnel at the RWTH Aachen University. This open-source tool set effectively translates and prepares the data for network transport through VPN connections between power system simulators.

Each of the connected power system simulators has the capability of simulating transmission and distribution level power systems, while also being able to interface the simulations with hardware via analog I/O. The capability to interface the simulation with physical hardware will be utilized at each of the university partners by integrating physical inverters or controllers into the power system. This capability integrated into the co-simulation network ensures that any physical effects that come from an operation mode transition are closely monitored and captured, with the physical response reflected into the co-simulation. Once this controller HIL system is connected, experiments will be performed on the inverter mode swapping operation and the impact on dynamic system stability to measure the impact and ensure that the mode swap does not cause damage to the power system.

After the co-simulation network is established with physical HIL at the partnering universities, network monitoring will be deployed at each grouping of inverters with the central monitoring center being the S -CIIC. A passive, open-source network traffic analyzer, namely Zeek, will be deployed and will capture traffic within the inverter command and control network. This traffic data will then be sent to a software platform (Kibana) that condenses the traffic logs sent by Zeek into a readable form, creating a security information and event management center (SIEM). This will establish a security operations center (SOC) for the co-simulation network at the S-CIIC lab, emulating a true command and control center with networking monitoring capabilities. Once the SOC functionality is established, SRNL personnel will perform known vulnerabilities for industrial control systems such as Industroyer2, Eternal-Blue, Havex, or BlackEnergy3.

Using the network traffic that occurs from the attacks, indicators of compromise (IOCs) will be developed that will be fed into the intrusion prevention system (IPS) that will signify as the flag to set in motion the swapped mode of inverter operation. The IPS will operate in a mode such that when an IOC is detected, a signal is sent from the control center to the inverters at the affected location to swap mode of operation from the centralized control mode to a communication-less mode. The inverter will respond to this mode swap and the transient physical effects will be reflected in the power system simulation. The stability and transient fluctuations will be observed and recorded through the simulations within the co-simulation network. A full stability analysis will be performed on the resulting harmonic transients within the power system after the mode swap, with the data being recorded and analyzed to observe the effects that the mode transition imparted on the power system.

Accomplishments

- Connected Grid Simulators between UofSC and SRNL.
- Built Real Time Simulation of SRS transmission network.
- Developed SCADA in GE iFIX for SRS transmission network inside of S-CIIC through DNP3 communication.
- Developed Modbus exploit that can bypass authentication to the PLC.
- Developed Modbus and DNP3 Man in the Middle python code.
- Developed PTP master exploit to change relay time values without SIEM detection.
- Deployed Security Onion SIEM to detect OT attacks.

Demonstration of Data Integrity Compromises on a CubeSat

Rachel Jones

Satellites form a vital part of modern infrastructure. Small satellites, such as CubeSats, are relatively new and under-researched relative to their larger government counterparts. This project aims to demonstrate a data integrity compromise on a CubeSat by modeling vulnerabilities that could be found in space infrastructure.

Introduction

Satellites are an important but vulnerable component in connected control systems. For example, Viasat, a satellite communications provider, was targeted by a cyber-attack in February of 2022. Newspapers reported how the communication outage caused disruptions to thousands of wind turbines in central Europe[1]. The issue interrupted operations of approximately 5,800 wind turbines at a capacity of 11 gigawatts, which is enough power to have caused wide-scale blackouts. Ongoing research is needed to secure command and control of satellites.

This project aims to demonstrate a data integrity compromise on a small satellite by demonstrating vulnerabilities that could be found in space infrastructure. The demonstration will be performed on an SRNL designed terrestrial-based satellite test bed (STB). As denoted in **Figure 1**, the STB utilizes a radio frequency glove box and can involve one or more CubeSats. SRNL currently has three 1U CubeSat simulators (see **Figures 2, 3, and 4**), with a 6U CubeSat on-order.

Next year, the STB will be used to demonstrate an attack on a satellite where the information stored and/or provided by the satellite will be changed. Then a novel method of Radio Frequency Intrusion Detection System (RFIDS) to detect indications of known exploits to satellite systems will be explored.

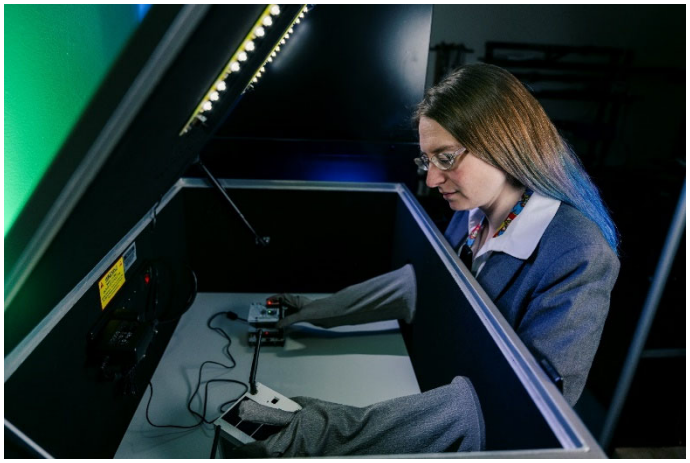

Figure 1. Picture of the inside of the Satellite Test Bed (STB). The radio frequency glove box is only able to block emissions when the lid is closed and sealed.

Approach

This project spans two years. The first year focused on building the hardware-in-the-loop STB with CubeSats. The LDRD collected information to analyze and define the problem by performing a literature review and conducting interviews with University CubeSat builders.

During the second year, the main goal will be to utilize the STB to demonstrate an integrity attack on a simulated satellite. Radio frequency signatures of known exploits will be used to create a database. Utilizing this database, information will be fed into a novel RFID device, which proposes a new way to protect radio frequency connected systems.

One of the defining features of satellite security is the necessity of radio communication to interface with high-altitude assets. This LDRD will investigate new

[1] Sheahan, M.; Steitz, C.; Rinke, A. Satellite Outage Knocks Out Thousands of Enercon's Wind Turbines. *Reuters* (online), February 28, 2022. https://www.reuters.com/business/energy/satellite-outage-knocks-out-control-enercon-wind-turbines-2022-02-28/

technologies to secure systems with radio interfaces. By attempting to examine waveforms at the physical level, next generation Intrusion Detection/Prevention Systems (IDS/IPS) may be able to flag or isolate malicious radio packets before they are transformed to the digital domain.

This research is significant because it will provide additional solutions to securing small satellites and other radio frequency-controlled devices, demonstrating the ability to conduct data integrity attacks on small satellites, and enhancing SRNL capabilities to respond to customer needs.

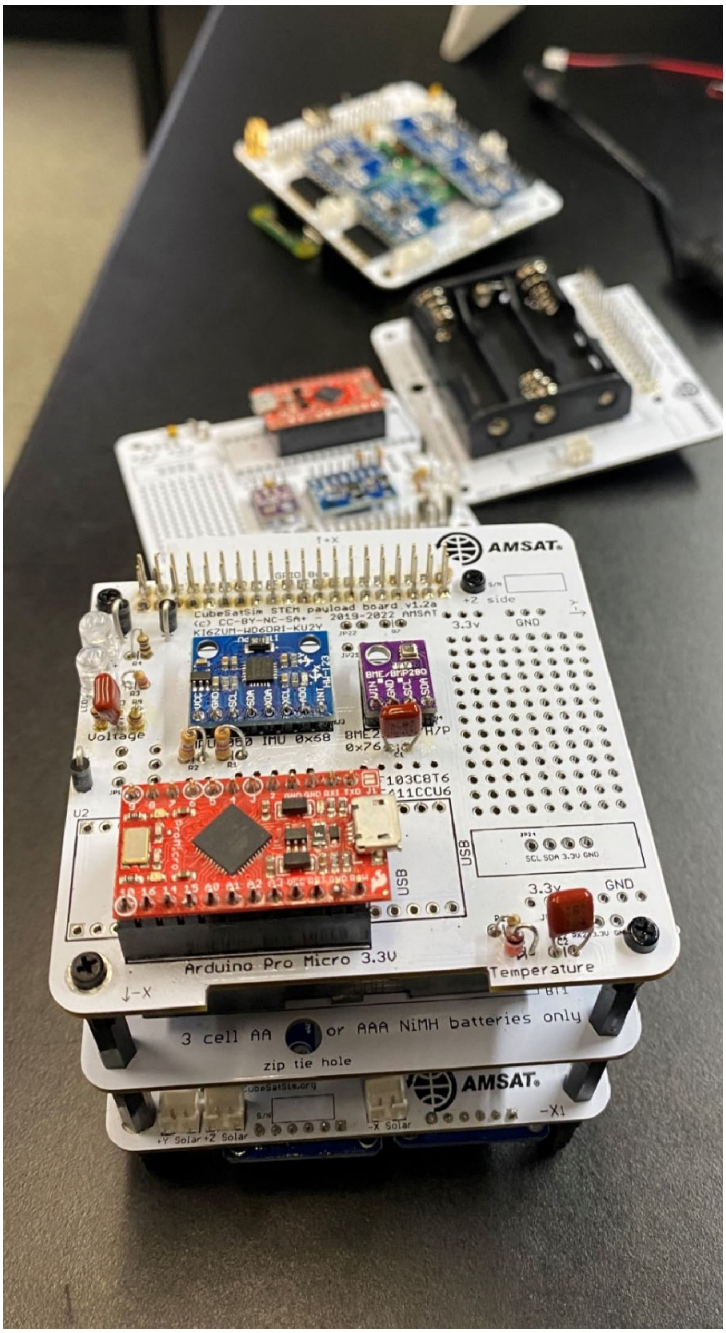

Figure 2. Up-close image of a 1U AMSAT CubeSat Simulator.

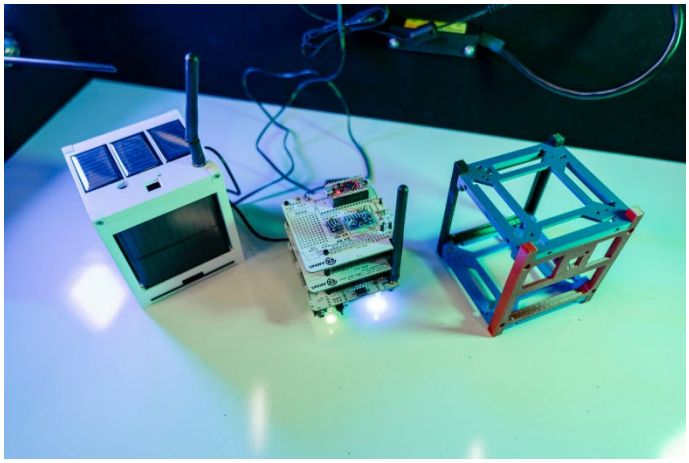

Figure 4. Left: Custom 3-D frame of 1U AMSAT CubeSat simulator showing antenna and various sized solar cells. Middle: The inside components of a1U AMSAT CubeSat simulator. Right: A traditional 1U AMSAT CubeSat simulator frame.

Accomplishments

- Designed and Constructed an SRNL Satellite Test Bed (STB) with permission to operate wirelessly in select radio frequency bands.
- Built three 1-U AMSAT CubeSat Simulators.
- Hosted a Graduate Student-in-Residence, Jackson Tilley, from a SRNL Partner the University of Georgia.
  - Jackson presented LDRD Research to the lab and university partners, in April of FY23
  - Helped gain DOE IRB approval for interviewing university small satellite build teams
  - In Progress, Peer-Review Qualitative Paper of those interviews (Target Publication Submission FY24)
- Rachel Jones, tied for Best Presenter at the 2022 Radio Club of America (RCA) Technical Symposium, November of FY-23.
- Rachel Jones and Scott Jordan were selected to present at the local cybersecurity conference, B-Sides Augusta, October of FY24.
- Continued development of a space science knowledge, expertise, and lab space at SRNL.

Intellectual Property

- Provisional Patent Acquired for a Radio Frequency Intrusion Detection System, July of FY23
- Invention Disclosure accepted, October of FY23

Team Members

Colton Bond, Ethan Farquhar, Scott Jordan, Sean Krautheim, Jackson Tilley**

***Graduate Student*

Savannah River National Laboratory®

U.S. DEPARTMENT OF ENERGY

LDRD LABORATORY DIRECTED RESEARCH & DEVELOPMENT

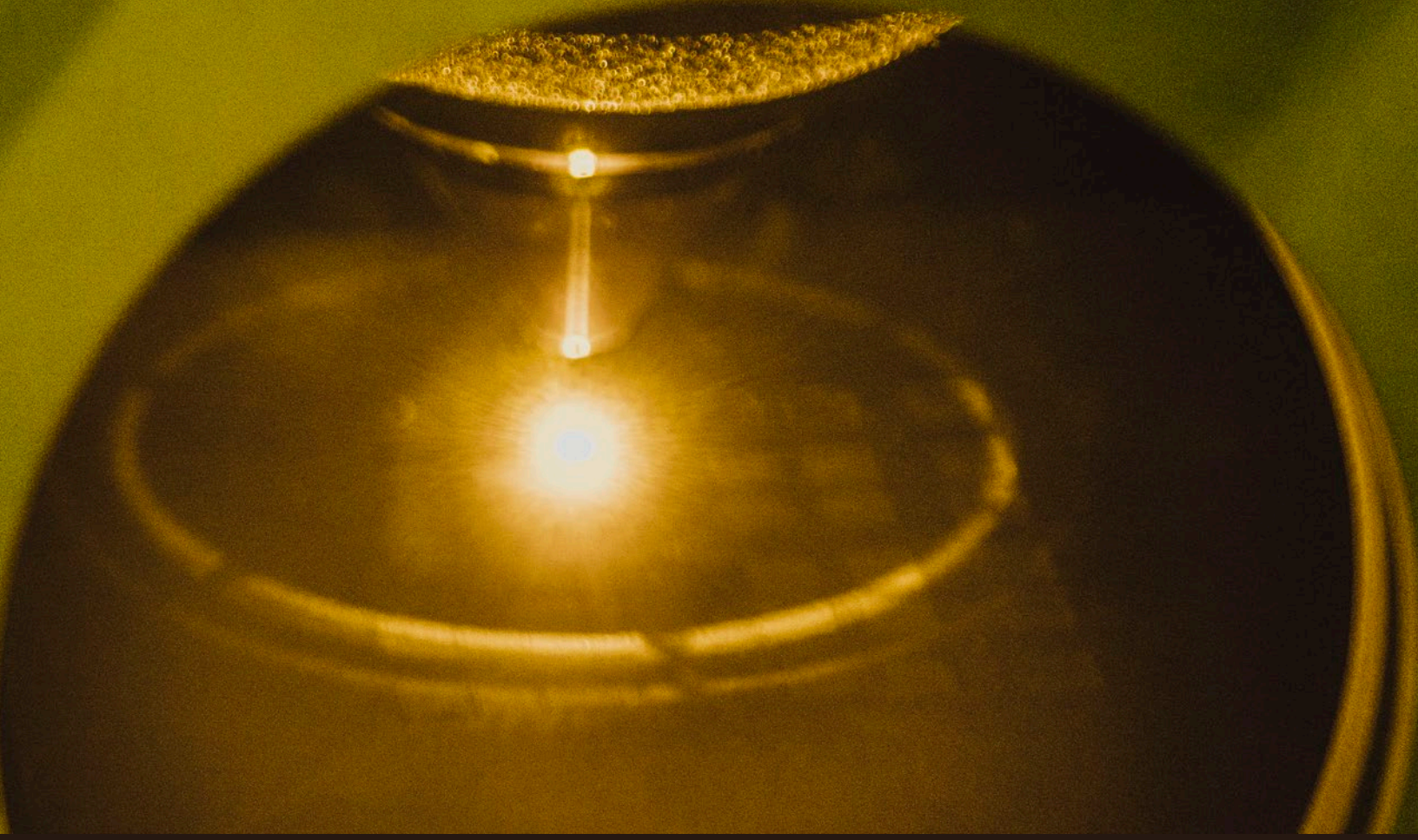

LDRD FY23 ANNUAL REPORT CONTRIBUTORS

Jonathon Baker

Kent Cubbage

Dale Hitchcock

Liz Hoffman

Tammy Newman

Jacqueline Ramos

LJ Gay, photography

Susanna King, design and layout

published January 2024

SRNL®

SAVANNAH RIVER NATIONAL LABORATORY